The REQUIEM Survey. I. A Search for Extended Lyα Nebular Emission Around 31 $z > 5.7$ Quasars

Emanuele Paolo Farina[1,2] , Fabrizio Arrigoni-Battaia[2] , Tiago Costa[2], Fabian Walter[1] , Joseph F. Hennawi[1,3] ,
Alyssa B. Drake[1] , Roberto Decarli[4] , Thales A. Gutcke[2] , Chiara Mazzucchelli[5] , Marcel Neeleman[1] , Iskren Georgiev[1] ,
Anna-Christina Eilers[1] , Frederick B. Davies[3] , Eduardo Bañados[1] , Xiaohui Fan[6] , Masafusa Onoue[1] ,
Jan-Torge Schindler[1] , Bram P. Venemans[1] , Feige Wang[3] , Jinyi Yang[6] , Sebastian Rabien[7], and Lorenzo Busoni[8]

[1] Max Planck Institut für Astronomie, Königstuhl 17, D-69117, Heidelberg, Germany; emanuele.paolo.farina@gmail.com
[2] Max Planck Institut für Astrophysik, Karl-Schwarzschild-Straße 1, D-85748, Garching bei München, Germany
[3] Department of Physics, University of California, Santa Barbara, CA 93106-9530, USA
[4] INAF—Osservatorio di Astrofisica e Scienza dello Spazio di Bologna, via Gobetti 93/3, I-40129, Bologna, Italy
[5] European Southern Observatory, Alonso de Córdova 3107, Vitacura, Región Metropolitana, Chile
[6] Steward Observatory, University of Arizona, 933 N Cherry Ave, Tucson, AZ 85719, USA
[7] Max Planck Institut für Extraterrestrische Physik Gießenbachstraße 1, D-85748, Garching bei München, Germany
[8] INAF—Osservatorio Astronomico di Arcetri, Largo Enrico Fermi 5, I-50125, Firenze, Italy

Abstract

The discovery of quasars a few hundred megayears after the Big Bang represents a major challenge to our understanding of black holes as well as galaxy formation and evolution. Quasars' luminosity is produced by extreme gas accretion onto black holes, which have already reached masses of $M_{BH} > 10^9 \, M_\odot$ by $z \sim 6$. Simultaneously, their host galaxies form hundreds of stars per year, using up gas in the process. To understand which environments are able to sustain the rapid formation of these extreme sources, we started a Very Large Telescope/Multi-Unit Spectroscopic Explorer (MUSE) effort aimed at characterizing the surroundings of a sample of $5.7 < z < 6.6$ quasars, which we have dubbed the Reionization Epoch QUasar InvEstigation with MUSE (REQUIEM) survey. We here present results of our searches for extended Lyα halos around the first 31 targets observed as part of this program. Reaching 5σ surface brightness limits of 0.1–1.1×10^{-17} erg s^{-1} cm^{-2} arcsec^{-2} over a 1 arcsec^2 aperture, we were able to unveil the presence of 12 Lyα nebulae, eight of which are newly discovered. The detected nebulae show a variety of emission properties and morphologies with luminosities ranging from 8×10^{42} to 2×10^{44} erg s^{-1}, FWHMs between 300 and 1700 km s^{-1}, sizes <30 pkpc, and redshifts consistent with those of the quasar host galaxies. As the first statistical and homogeneous investigation of the circumgalactic medium of massive galaxies at the end of the reionization epoch, the REQUIEM survey enables the study of the evolution of the cool gas surrounding quasars in the first 3 Gyr of the universe. A comparison with the extended Lyα emission observed around bright ($M_{1450} \lesssim -25$ mag) quasars at intermediate redshift indicates little variations on the properties of the cool gas from $z \sim 6$ to $z \sim 3$, followed by a decline in the average surface brightness down to $z \sim 2$.

Unified Astronomy Thesaurus concepts: Quasars (1319); Cosmology (343); Early universe (435); Circumgalactic medium (1879)

Supporting material: extended figures, machine-readable table

1. Introduction

Where do the first quasars form? Two decades after the discovery of the first quasar at $z > 6$ (i.e., J1030+0524 at $z = 6.3$; Fan et al. 2001), this question still puzzles astronomers. Assuming a simple model where a massive black hole grows at the Eddington limit starting at a certain time t_0 from a seed with mass $M_{BH}(t_0) = M_{seed}$, the evolution of the mass with time can be expressed as:

$$M_{BH}(t) = M_{seed} \times \exp\left[f_{Duty}(1 - \eta)\frac{t - t_0}{t_{Sal}} \right], \qquad (1)$$

where f_{Duty} is the duty cycle and η is the fraction of rest mass energy released during the accretion. The timescale of the mass growth is set by the Salpeter time (Salpeter 1964): $t_{Sal} = \epsilon\sigma_T \, c/(4\pi \, G \, m_p) = \epsilon \, 450$ Myr, where σ_T is the Thomson cross section, m_p is the proton mass, and ϵ is the radiation efficiency.[9]

---

[9] The presence of helium, with a mass of $\sim 4 \times m_p$ and two free electrons, allows a faster growth of the black holes. Considering a plasma with abundances $X = 0.75$ for hydrogen and $Y = 0.25$ for helium, the Salpeter time becomes $t_{Sal} = \epsilon \, 390$ Myr.

In standard radiatively efficient accretion disks, all the energy is radiated away, and it is typically assumed that $\epsilon = \eta = 0.1$ (Soltan 1982; Tanaka & Haiman 2009; Davis & Laor 2011; Davies et al. 2019a). Equation (1) implies that, for instance, a $10^2 \, M_\odot$ remnant of a Population III star at $z = 30$ needs to accrete at the Eddington limit for its entire life ($f_{Duty} = 1$) to reach a black hole mass $>10^9 \, M_\odot$ at $z \sim 6$, as observed in quasars (e.g., De Rosa et al. 2011, 2014; Mortlock et al. 2011; Wu et al. 2015; Mazzucchelli et al. 2017; Bañados et al. 2018; Pons et al. 2019; Reed et al. 2019; Shen et al. 2019). In addition, investigations at mm and submm wavelengths also revealed that the host galaxies of these first quasars are vigorously growing in mass, with star formation rates SFR $\gg 100 \, M_\odot$ yr^{-1} (e.g., Walter et al. 2009; Venemans et al. 2012, 2016, 2018; Wang et al. 2013, 2019a; Willott et al. 2015, 2017; Decarli et al. 2018; Kim & Im 2019; Shao et al. 2019; Yang et al. 2019a).

To comprehend how these first quasars form and grow, it is important to understand where they are hosted. Efstathiou & Rees (1988) first proposed that, in the current ΛCDM paradigm

of galaxy formation (e.g., White & Rees 1978), only rare high peaks in the density field contain enough gas to build up the black hole and star mass (taking into account mass losses due to supernova-driven winds) of high-redshift quasars. This scenario is supported by cosmological hydrodynamic simulations (e.g., Sijacki et al. 2009; Costa et al. 2014) and analytical arguments (e.g., Volonteri & Rees 2006) showing that only the small fraction of black holes that, by $z \sim 6$, are hosted by $\gtrsim 10^{12}\ M_{\odot}$ dark matter halos can grow efficiently into a population of quasars with masses and accretion rates matching current observational constraints (but see discussion in Fanidakis et al. 2013). To compensate for the rapid gas consumption, the host galaxies need a continuous replenishment of fresh fuel provided by filamentary streams of $T = 10^{4}$–10^{5} K pristine gas from the intergalactic medium (IGM) and/or by mergers with gas rich halos (e.g., Yoo & Miralda-Escudé 2004; Kereš et al. 2005, 2009; Volonteri & Rees 2005; Dekel & Birnboim 2006; Li et al. 2007; Dekel et al. 2009; Volonteri 2010, 2012; Fumagalli et al. 2011; Di Matteo et al. 2012; van de Voort et al. 2012; Habouzit et al. 2019; Mayer & Bonoli 2019). Observational validations of this framework can be set by the detection of gas reservoirs and satellites in the so-called circumgalactic medium (CGM; empirically defined as the regions within a few hundreds of kiloparsecs from a galaxy) of high-redshift quasars.

Historically, information on the CGM has been provided by absorption signatures imprinted on background sightlines. This revealed the presence of halos of cool and enriched gas extending to ~ 200 pkpc from high-redshift galaxies (e.g., Bahcall & Spitzer 1969; Steidel et al. 1994; Chen & Tinker 2008; Chen et al. 2010a, 2010b; Gauthier et al. 2010; Churchill et al. 2013a; Nielsen et al. 2013a, 2013b; Werk et al. 2016; Tumlinson et al. 2017). In particular, this technique applied to close projected quasar pairs revealed that intermediate redshift quasars are surrounded by massive ($>10^{10}\ M_{\odot}$), metal-rich ($Z \gtrsim 0.1 Z_{\odot}$), and cool ($T \sim 10^{4}$ K) gas reservoirs (e.g., Bowen et al. 2006; Hennawi et al. 2006; Hennawi & Prochaska 2007; Decarli et al. 2009; Prochaska & Hennawi 2009; Farina et al. 2013, 2014; Prochaska et al. 2013a, 2013b; Johnson et al. 2015; Lau et al. 2016, 2018). However, the rapid drop in the number density of bright background sources with redshift causes absorption studies to lose effectiveness at $z \gtrsim 4$.

A promising way to push investigation of the CGM of quasars up to the epoch of reionization is to probe the cool gas in emission. The strong flux of UV photons radiating from the active galactic nucleus (AGN) can be reprocessed in the hydrogen Lyα line at 1215.7 Å (Lyman 1906; Millikan 1920) by the surrounding gas, giving rise to an extended "fuzz" of fluorescent Lyα emission (e.g., Rees 1988; Haiman & Rees 2001; Alam & Miralda-Escudé 2002). Several pioneering efforts have been performed to reveal such halos in the vicinity of $z \sim 2$–4 quasars (e.g., Heckman et al. 1991a, 1991b; Christensen et al. 2006; North et al. 2012; Hennawi & Prochaska 2013; Roche et al. 2014; Herenz et al. 2015; Arrigoni Battaia et al. 2016, 2019a). This led to the general consensus that 10–50 kpc nebulae are (almost) ubiquitous around intermediate-redshift quasars, and that a few objects (typically associated with galaxy overdensities) are surrounded by giant Lyα nebulae with sizes >300 kpc, i.e., larger than the expected virial radius for such systems (e.g., Cantalupo et al. 2014; Martin et al. 2014; Hennawi et al. 2015; Cai et al. 2017).

A change of gear in these searches was driven by the recent development of the new generation of sensitive integral field spectrographs (IFSs) on 10 m class telescopes, i.e., the Multi-Unit Spectroscopic Explorer (MUSE; Bacon et al. 2010) on the ESO/Very Large Telescope (VLT) and the Keck Cosmic Web Imager (KCWI; Morrissey et al. 2012, 2018) on the Keck II telescope. These instruments have been successfully exploited to map the diffuse gas in the CGM of hundreds of intermediate redshift galaxies (e.g., Wisotzki et al. 2016; Leclercq et al. 2017; Erb et al. 2018) and quasars (e.g., Martin et al. 2014; Husband et al. 2015; Borisova et al. 2016; Fumagalli et al. 2016; Arrigoni Battaia et al. 2018b, 2019a, 2019b; Ginolfi et al. 2018; Cai et al. 2019; Lusso et al. 2019). The picture emerging is that the cool gas around $z \sim 2$–4 radio-quiet quasars has a quiescent kinematics and it is likely to be constituted by a population of compact (with sizes of $\lesssim 50$ pc) dense ($n_{\rm H} \gtrsim 1\ {\rm cm}^{-3}$) clouds that are optically thin to the quasar radiation (e.g., Hennawi & Prochaska 2013; Arrigoni Battaia et al. 2015a; Hennawi et al. 2015; Cantalupo 2017; Cantalupo et al. 2019).

However, by $z = 4$, the universe is already 1.5 Gyr old and a population of massive, quiescent galaxies is already in place (e.g., Straatman et al. 2014, 2016). To probe the first stages of galaxy formation, it is thus necessary to push these studies to $z \gtrsim 6$. To date, extended Lyα halos have been reported only for a handful of $z \sim 6$ quasars via exploiting different techniques: narrowband imaging (Goto et al. 2009; Decarli et al. 2012; Momose et al. 2019), long-slit spectroscopy (Willott et al. 2011; Goto et al. 2012; Roche et al. 2014), and IFS (Farina et al. 2017; Drake et al. 2019). This small sample has shown that the first quasars can be surrounded by extended nebulae with luminosities up to $L({\rm Ly}\alpha) \sim 10^{44}\ {\rm erg\ s}^{-1}$ and sizes $\lesssim 40$ pkpc. However, a detailed interpretation of these results is hampered by the small number statistics and by the heterogeneity of the data.

To overcome these limitations, we started the Reionization Epoch QUasar InvEstigation with MUSE (REQUIEM) survey aimed at performing a statistical and homogeneous census of the close environment of the first quasars. In this paper, we report results from the investigation of the first 31 $5.7 < z < 6.6$ quasars part of this ongoing program, including the reanalysis of MUSE data from Farina et al. (2017) and Drake et al. (2019), focusing our attention on the properties of the extended Lyα halos as a tracer of the gas reservoirs able to fuel the activity of the first quasars. We defer the analysis of the close galactic environment of these systems to a future paper.

To summarize, the analysis of the MUSE observations (see Section 3) of the 31 targets presented in Section 2 with the procedure described in Section 4 led to the discovery of 12 extended Lyα nebulae above a surface brightness limit of ${\rm SB}_{{\rm Ly}\alpha} \sim$ few $\times 10^{18}\ {\rm erg\ s}^{-1}\ {\rm cm}^{-2}\ {\rm arcsec}^{-2}$ ($\sim 40\%$ of the cases; see Section 5). In Section 5, we report on the attributes of the detected halos, we compare them with the properties of the quasar host galaxies and of the central supermassive black holes, and we test for possible signatures of CGM evolution down to $z \sim 3$. Finally, a summary is given in Section 6.

Throughout this paper, we assume a concordance cosmology with $H_0 = 70\ {\rm km\ s}^{-1}\ {\rm Mpc}^{-1}$, $\Omega_{\rm M} = 0.3$, and $\Omega_{\Lambda} = 1 - \Omega_{\rm M} = 0.7$. In this cosmology, at $z = 6.2$ (the average redshift of our sample) the universe is 0.877 Gyr old, and an angular scale of $\theta = 1''$ corresponds a proper transverse separation of 5.6 kpc. We remind the reader that MUSE is able to cover the Lyα line

up to redshift $z \sim 6.6$ at a spectral resolution of $R = \lambda/\Delta\lambda \sim 3500$ at $\lambda \sim 9000$ Å with a spatial sampling of $0\farcs2 \times 0\farcs2$ (corresponding to 1.1 pkpc × 1.1 pkpc at $z = 6$) over a ~ 1 arcmin^2 field of view.

2. Sample Selection

Our sample consists of 31 quasars in the redshift range $5.77 < z < 6.62$ located in the southern sky (e.g., Fan et al. 2001, 2003, 2006; Willott et al. 2007, 2010; Venemans et al. 2013; Bañados et al. 2016; Jiang et al. 2016; Mazzucchelli et al. 2017; Reed et al. 2017; Matsuoka et al. 2018; Wang et al. 2019b; Yang et al. 2019b). This includes all available MUSE observations of $z > 5.7$ quasars present in the ESO Archive at the time of writing (2019 August). These quasars have an average redshift of $\langle z \rangle = 6.22$ and an average absolute magnitude of $\langle M_{1450} \rangle = -26.9$ mag (see Table 1 and Figure 1). Among these, only J2228+0110 is a confirmed radio-loud quasar (considering radio-loud quasars as having $R = f_{\nu,5\,\text{GHz}}/f_{\nu,4400\,\text{Å}} > 10$, Kellermann et al. 1989; Bañados et al. 2015b; E. Bañados et al. 2019, in preparation).

In the following, we will refer to the entire data set as our *full sample*, and to the subset of 23 quasars with $M_{1450} < -25.25$ mag and $5.95 < z < 6.62$ as our *core sample*. This well-defined subsample is highly representative of the high-z population of luminous quasars (see Figure 1) and largely overlaps with the survey of dust continuum and [C II] 158 μm fine-structure emission lines in $z > 6$ quasar host galaxies using the Atacama Large Millimeter Array (ALMA) presented in Decarli et al. (2017, 2018) and Venemans et al. (2018).

2.1. Notes on Individual Objects

J0305−3150—Farina et al. (2017) reported the presence of a faint nebular emission extending ~ 9 pkpc toward the southwest of the quasar. In addition, the presence of a Lyα emitter (LAE) at a projected separation of 12.5 kpc suggests that J0305−3150 is tracing an overdensity of galaxies. This hypothesis has been corroborated by recent high-resolution ALMA imaging that revealed the presence of three [C II] 158 μm emitters located within ~ 40 kpc and ~ 1000 km s^{-1} from the quasar (Venemans et al. 2019). These observations also showed the complex morphology of the host galaxy, possibly due to interactions with nearby galaxies (Venemans et al. 2019). Ota et al. (2018), using deep narrowband imaging obtained with the Subaru Telescope Suprime-Cam, reported an LAE number density comparable with the background. However, the displacement between the location of the redshifted Lyα emission and wavelengths with high response of the NB921 filter used (see Figure 2 in Ota et al. 2018) may have hindered the detection of galaxies associated with the quasar.

P231−20—ALMA observations of this quasar revealed the presence of a massive [C II] 158 μm bright galaxy in its immediate vicinity (with a projected separation of 13.8 kpc and a velocity difference of 591 km s^{-1}; see Decarli et al. 2017). A sensitive search for the rest-frame UV emission from this companion galaxy is presented in Mazzucchelli et al. (2019). An additional weaker [C II] 158 μm emitter has been identified by Neeleman et al. (2019) 14 kpc south–southeast of the quasar. Deep MUSE observations already revealed the presence of a ~ 18 pkpc Lyα nebular emission around this quasar (Drake et al. 2019).
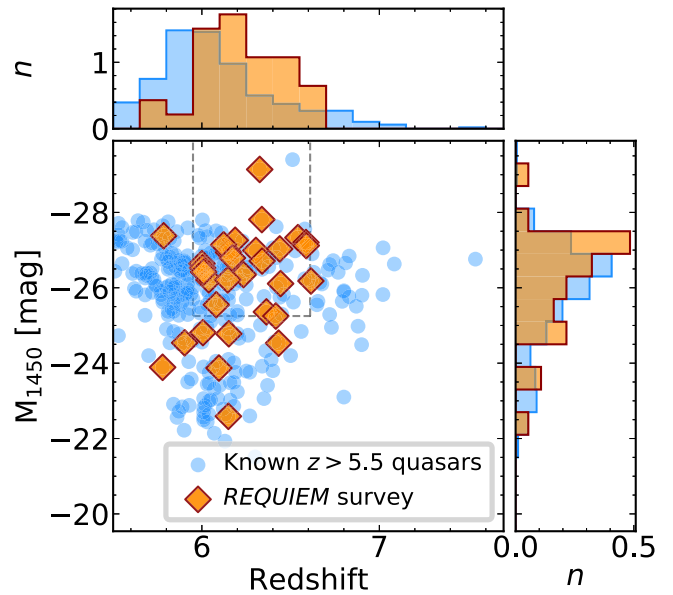
Figure 1. Distribution of all $z > 5.5$ quasars known to date in the redshift vs. absolute magnitude plane at 1450 Å (light blue circles and histograms). Orange diamonds and histograms mark targets from our survey. Histograms are normalized by the total number of targets and by the bin size (with steps 0.15 in redshift and of 0.6 mag in absolute magnitude). The limits in luminosity and redshift of our *core sample* (see Section 2) are plotted as gray dashed lines. The five quasars outside these boundaries are: J0129−0035 at $z = 5.78$, J1044 −0125 at $z = 5.78$, J2228+0110 at $z = 5.90$, J0055+0146 at $z = 6.01$, J2216 −0016 at $z = 6.10$, J2219+0102 at $z = 6.15$, J2229+1457 at $z = 6.15$, and J2318−3113 at $z = 6.44$. A 2D Kolmogorov–Smirnov test (Fasano & Franceschini 1987) performed with bootstrap resampling of the parent data set of the $5.95 < z < 6.62$ and $M_{1450} < -25.25$ mag quasars does not refute the null hypothesis that our *core sample* has a distribution different from the parent data set distribution (p-value $\gtrsim 0.2$).

P183+05—For this quasar, Bañados et al. (2019) reported the presence of a proximate damped Lyα absorption system (pDLA) located at $z = 6.40392$ (1400 km s^{-1} away from the quasar host galaxy), making this system the highest-redshift pDLA known to date. It shows an H I column density of $N_{\text{H I}} = 10^{20.77\pm0.25}$ cm^{-2} and relative chemical abundances typical of a high-redshift low-mass galaxy. The pDLA can act as a coronagraph, and by blocking its light, it allows one to perform sensitive searches for extended emission associated to the background quasar (e.g., Hennawi et al. 2009). The galaxy originating the pDLA is not detected as a Lyα line *down-the-barrel* in the MUSE quasar's spectrum (see Figure 15 in Appendix A). However, it could be located at a larger impact parameter (e.g., Neeleman et al. 2016, 2017, 2018; D'Odorico et al. 2018). The possibility to detect the galaxy in the full MUSE datacube, both in emission and as a shadow against the extended background Lyα halo, will be explored in a future paper of this series (E. P. Farina et al. 2019, in preparation).

J2329−0301—The Lyα halo of this quasar has been the subject of several studies (Goto et al. 2009, 2012; Willott et al. 2011; Drake et al. 2019; Momose et al. 2019). Goto et al. (2017) reported the complete absence of LAEs down to a narrowband magnitude of NB906 = 25.4 mag (at 50% completeness) in the entire field-of-view of the Subaru Telescope Suprime-Cam (~ 200 cMpc^2).

J0100+2802—With $M_{1450} = -29.09$ mag, J0100+2802 is the brightest (unlensed) quasar known at $z > 6$ (Wu et al. 2015). Subarcsecond resolution observations of the [C II] 158 μm and CO emission lines suggest that the host galaxy has a dynamical

<div align="center">

Table 1
Quasars Observed with MUSE in Decreasing Redshift Order

</div>

ID	R.A. (J2000)	Decl. (J2000)	Redshift	M_{1450} (mag)	Prog. ID.	Exp. Time (s)	Image Quality ($''$)	SB$^1_{5\sigma}$ (erg s^{-1} cm^{-2} arcsec^{-2})
J0305−3150	03:05:16.916	−31:50:55.90	6.6145 ± 0.0001[a]	−26.12	094.B-0893	8640.	0.53	0.29×10^{-17}
P323+12	21:32:33.191	+12:17:55.26	6.5881 ± 0.0003[b]	−27.06	0101.A-0656	2964.	0.85	0.48×10^{-17}
P231−20	15:26:37.841	−20:50:00.66	6.5864 ± 0.0005	−27.14	099.A-0682	11856.	0.63	0.30×10^{-17}
P036+03	02:26:01.876	+03:02:59.39	6.5412 ± 0.0018[c]	−27.28	0101.A-0656	2964.	0.61	0.33×10^{-17}
J2318−3113	23:18:18.351	−31:13:46.35	6.4435 ± 0.0004	−26.06	0101.A-0656	2964.	0.65	0.54×10^{-17}
P183+05	12:12:26.981	+05:05:33.49	6.4386 ± 0.0004	−26.98	099.A-0682	2964.	0.62	0.92×10^{-17}
J0210−0456	02:10:13.190	−04:56:20.90	6.4323 ± 0.0005[d]	−24.47	0103.A-0562	2964.	1.24	0.26×10^{-17}
J2329−0301	23:29:08.275	−03:01:58.80	6.4164 ± 0.0008[e]	−25.19	60.A-9321	7170.	0.65	0.18×10^{-17}
J1152+0055	11:52:21.269	+00:55:36.69	6.3643 ± 0.0005[m]	−25.30	0103.A-0562	2964.	1.18	0.90×10^{-17}
J2211−3206	22:11:12.391	−32:06:12.94	6.3394 ± 0.0010	−26.66	0101.A-0656	2964.	0.73	1.49×10^{-17}
J0142−3327	01:42:43.727	−33:27:45.47	6.3379 ± 0.0004	−27.76	0101.A-0656	2964.	0.71	1.11×10^{-17}
J0100+2802	01:00:13.027	+28:02:25.84	6.3258 ± 0.0010[f]	−29.09	0101.A-0656	2964.	1.29	1.13×10^{-17}
J1030+0524	10:30:27.098	+05:24:55.00	6.3000 ± 0.0002[g]	−26.93	095.A-0714	23152.	0.51	0.08×10^{-17}
P308−21	20:32:09.996	−21:14:02.31	6.2341 ± 0.0005	−26.29	099.A-0682	17784.	0.77	0.26×10^{-17}
P065−26	04:21:38.052	−26:57:15.60	6.1877 ± 0.0005	−27.21	0101.A-0656	2964.	0.68	0.25×10^{-17}
P359−06	23:56:32.455	−06:22:59.26	6.1722 ± 0.0004	−26.74	0101.A-0656	2964.	0.58	0.28×10^{-17}
J2229+1457	22:29:01.649	+14:57:08.99	6.1517 ± 0.0005[h]	−24.72	0103.A-0562	2964.	0.54	0.27×10^{-17}
P217−16	14:28:21.394	−16:02:43.29	6.1498 ± 0.0011	−26.89	0101.A-0656	2964.	0.90	0.32×10^{-17}
J2219+0102	22:19:17.217	+01:02:48.90	6.1492 ± 0.0002[e]	−22.54	0103.A-0562	2964.	0.69	0.48×10^{-17}
J2318−3029	23:18:33.100	−30:29:33.37	6.1458 ± 0.0005	−26.16	0101.A-0656	2964.	0.73	0.30×10^{-17}
J1509−1749	15:09:41.778	−17:49:26.80	6.1225 ± 0.0007	−27.09	0101.A-0656	2964.	0.88	0.46×10^{-17}
J2216−0016	22:16:44.473	−00:16:50.10	6.0962 ± 0.0003[i]	−23.82	0103.A-0562	2964.	1.12	0.48×10^{-17}
J2100−1715	21:00:54.616	−17:15:22.50	6.0812 ± 0.0005	−25.50	297.A-5054	13338.	0.67	0.23×10^{-17}
J2054−0005	20:54:06.481	−00:05:14.80	6.0391 ± 0.0001[j]	−26.15	0101.A-0656	3869.	0.81	0.24×10^{-17}
P340−18	22:40:48.997	−18:39:43.81	6.01 ± 0.05[k]	−26.36	0101.A-0656	2964.	0.55	0.26×10^{-17}
J0055+0146	00:55:02.910	+01:46:18.30	6.0060 ± 0.0008[h]	−24.76	0103.A-0562	2964.	0.75	0.27×10^{-17}
P009−10	00:38:56.522	−10:25:53.90	6.0039 ± 0.0004	−26.50	0101.A-0656	2964.	0.67	0.27×10^{-17}
P007+04	00:28:06.560	+04:57:25.68	6.0008 ± 0.0004	−26.59	0101.A-0656	2964.	1.19	0.35×10^{-17}
J2228+0110	22:28:43.535	+01:10:32.20	5.9030 ± 0.0002[l]	−24.47	095.B-0419	40950.	0.61	0.11×10^{-17}
J1044−0125	10:44:33.042	−01:25:02.20	5.7847 ± 0.0007[i]	−27.32	0103.A-0562	2964.	0.94	0.32×10^{-17}
J0129−0035	01:29:58.510	−00:35:39.70	5.7787 ± 0.0001[j]	−23.83	0103.A-0562	2964.	1.19	0.26×10^{-17}

Notes. Seeing and 5σ surface brightness limits have been estimated on pseudo-narrowband images obtained by collapsing five wavelength channels (for a total of 6.25 Å) at the expected location of the Lyα emission of the quasars. Unless otherwise specified, we report systemic redshifts measured from the [C II] 158 μm emission lines by Decarli et al. (2018).
[a] [C II] 158 μm redshift from Venemans et al. (2013).
[b] [C II] 158 μm redshift from Mazzucchelli et al. (2017).
[c] [C II] 158 μm redshift from Bañados et al. (2015a).
[d] [C II] 158 μm redshift from Willott et al. (2013).
[e] [C II] 158 μm redshift from Willott et al. (2017).
[f] [C II] 158 μm redshift from Wang et al. (2016).
[g] Redshift derived by De Rosa et al. (2011) from the fit of the Mg II broad emission line.
[h] [C II] 158 μm redshift from Willott et al. (2015).
[i] [C II] 158 μm redshift from Izumi et al. (2018).
[j] [C II] 158 μm redshift from Wang et al. (2013).
[k] The [C II] 158 μm emission of P340−18 was not detected in eight-minute ALMA integration by Decarli et al. (2018). We report the redshift inferred from the observed optical spectrum by Bañados et al. (2016).
[l] Redshift derived by Roche et al. (2014) from the measurement of the Lyα line.
[m] Izumi et al. (2018) report a slightly different (but consistent within the error) [C II] 158 μm redshift for J1152+0055: $z = 6.3637 \pm 0.0005$.

mass of only ∼$1.9 \times 10^{11}\ M_\odot$ (Wang et al. 2019a). Given this high luminosity, its proximity zone appears to be small [$R_p = (7.12 \pm 0.13)$ pMpc], implying that this quasar is relatively young, with a quasar age of $t_{QSO} \sim 10^5$ yr (Eilers et al. 2017; Davies et al. 2019b).

J1030+0524—Deep broadband optical and near-IR investigation evidenced an overdensity of Lyman-Break galaxies in the field of this quasar (Morselli et al. 2014; Balmaverde et al. 2017; Decarli et al. 2019b). Searches for the presence of Lyα extended emission around this target has already been investigated with sensitive *Hubble Space Telescope* (*HST*)

observations by Decarli et al. (2012) and with MUSE by Drake et al. (2019).

P308−21—The [C II] 158 μm emission line of this quasar host galaxy is displaced by ∼25 kpc and shows an enormous velocity gradient extending across more than $1000\ \mathrm{km\ s^{-1}}$ (Decarli et al. 2017). High-resolution ALMA and *HST* observations revealed that the host-galaxy emission is split into (at least) three distinct components. The observed gas morphology and kinematics is consistent with the close interaction of a single satellite with the quasar (Decarli et al. 2019a). Deep *Chandra* observations the companion galaxy

might contain a heavily obscured AGN (Connor et al. 2019). A direct comparison of our new MUSE data with the ALMA [C II] 158 μm and dust maps will be presented in a forthcoming paper (E. P. Farina et al. 2019, in preparation).

J2229+1457—With a size of only $R_p = (0.45 \pm 0.14)$ pMpc, the proximity zone of this object is the smallest among the 31 $5.8 \lesssim z \lesssim 6.5$ quasars investigated by Eilers et al. (2017). This suggests a short quasar age ($t_{QSO} \lesssim 10^5$ yr) for this object (Eilers et al. 2017; Davies et al. 2019b).

J2219+0102—This is the faintest target in our survey. Despite the low luminosity of the accretion disk, the host galaxy is undergoing a powerful starburst detected at mm wavelengths (with an inferred star formation rate of SFR $\sim 250\ M_\odot\ \mathrm{yr}^{-1}$) and appears to be resolved with a size of 2–3 kpc (Willott et al. 2017).

J2216−0016—The rest-frame UV spectrum of this faint quasar shows a N V broad absorption line (Matsuoka et al. 2016). The structure of the [C II] 158 μm line appears to be complex, suggesting the presence of a companion galaxy merging with the quasar host galaxy (Izumi et al. 2018)

J2100−1715—Decarli et al. (2017) reported the presence of a [C II] 158 μm bright companion located at a projected separation of 60.7 kpc, with a velocity difference of -41 km s^{-1} from the quasar's host galaxy. The search for the Lyα emission arising from this companion in the MUSE data is presented in Mazzucchelli et al. (2019). Drake et al. (2019) reported the absence of extended Lyα emission around this quasar.

P007+04—The broad Lyα line of this quasar is truncated by the presence of a pDLA (see Figure 15 in Appendix A). The analysis of the absorbing gas generating this feature and the search for its rest-frame UV counterpart will be presented in a future paper of this series (E. P. Farina et al. 2019, in preparation).

J2228+0110—A faint, extended Lyα emission has been detected by Roche et al. (2014) in deep long-slit spectroscopic observations of this faint radio-loud quasar (with radio-loudness $R \sim 60$; Zeimann et al. 2011; Bañados et al. 2015b). The presence of the halo was confirmed by Drake et al. (2019) with MUSE observations.

J1044−0125—ALMA 0″.2 resolution observations of the [C II] 158 μm fine structure line showed evidence of turbulent gas kinematics in the host galaxy and revealed the possible presence of a faint companion galaxy located at a separation of 4.9 kpc (Wang et al. 2019c).

3. Observations and Data Reduction

Observations of the quasars in our sample have been collected with the MUSE instrument on the VLT telescope *YEPUN* as a part of the ESO programs: 60.A-9321(A, Science Verification), 094.B-0893(A, PI: Venemans), 095.B-0419 (A, PI: Roche), 095.A-0714(A, PI: Karman), 099.A-0682 (A, PI: Farina), 0101.A-0656(A, PI: Farina), 0103.A-0562(A, PI: Farina), and 297.A-5054(A, PI: Decarli). Typically, the total time on target was ∼50 minutes, divided into two exposures of 1482 s differentiated by a $<5″$ shift and a 90° rotation. For eight targets, longer integrations have been acquired (ranging from 65 to 680 minutes), and the shift and rotation pattern were repeated several times (see Table 1).

Data reduction was performed as in Farina et al. (2017) using the MUSE DATA REDUCTION SOFTWARE version 2.6 (Weilbacher et al. 2012, 2014) complemented by our own set of custom-built routines. The basic steps are summarized in the following. Individual exposures were bias-subtracted, corrected

for flat field and illumination, and calibrated in wavelength and flux. We then subtracted the sky emission and resampled the data onto a 0″.2 × 0″.2 × 1.25 Å grid.[10] White light images were then created and used to estimate the relative offsets between different exposures of a single target. From these images, we also determined the relative flux scaling between exposures by performing force photometry on sources in the field. Finally, we average-combined the exposures into a single cube. Residual illumination patterns were removed using the ZURICH ATMOSPHERE PURGE (ZAP) software (version 2.0 Soto et al. 2016), setting the number of eigenspectra (nevals) to three and masking sources detected in the white light images. This procedure, however, comes at the price of possibly removing some astronomical flux from the cubes. In the following, we will present results from the "cleaned" data cubes. However, we also double-checked for extended emission in the data prior to the use of ZAP. To take voxel-to-voxel correlations into account, that can result in an underestimation of the noise calculated by the pipeline, we rescaled the variance datacube to match the measured variance of the background (see, e.g., Bacon et al. 2015; Borisova et al. 2016; Farina et al. 2017; Arrigoni Battaia et al. 2019a). The astrometry solution was refined by matching sources with the Pan-STARRS1 (PS1) data archive (Chambers et al. 2016; Flewelling et al. 2016) or with other available surveys if the field was not covered by the PS1 footprint. We corrected for reddening toward the quasar location using $E(B-V)$ values from Schlafly & Finkbeiner (2011) and assuming $R_V = 3.1$ (e.g., Cardelli et al. 1989; Fitzpatrick 1999). Absolute flux calibration was obtained matching the z-band photometry of sources in the field with PS1 and/or with the Dark Energy Camera Legacy Survey.[11] In Table 1, we report the 5σ surface brightness limits estimated over a 1 arcsec^2 aperture after collapsing five wavelength slices that were centered at the expected position of the Lyα line shifted to the systemic redshift of the quasar ($\mathrm{SB}^1_{5\sigma,\mathrm{Ly\alpha}}$). These range from $\mathrm{SB}^1_{5\sigma,\mathrm{Ly\alpha}} = 0.1$ to 1.1×10^{-17} erg s^{-1} cm^{-2} arcsec^{-2}, depending on exposure times, sky conditions, and on the redshift of the quasar. Postage stamps of the quasar vicinities and quasar spectra are shown in Appendix A.

4. Searching for Extended Emission

An accurate point-spread function (PSF) subtraction is necessary to recover the faint signal of the diffuse Lyα emission emerging from the PSF wings of the bright unresolved nuclear component. The steps we executed on each datacube to accomplish this goal are summarized in the following:

1. We removed possible foreground objects located in close proximity to the quasar. To perform this step, we first collapsed the datacube along wavelengths blueward of the redshifted Lyα line location. Due to the Gunn–Peterson effect, the resulting image is virtually free of any object with a redshift consistent with or larger than the quasar's one. For each source detected in this image, we extracted the emission over an aperture three times larger

---

[10] Cosmic rays could have an impact on the final quality of the cubes when only two exposures have been collected. Their rejection is performed by the pipeline in the post-processing of the data considering a sigma rejection factor of crsigma = 15.
[11] http://legacysurvey.org/

than the effective radius. We used this as an empirical model of the object's light profile.[12] This model was then propagated through the datacube by rescaling it to the flux of source measured at each wavelength channel. Finally, all these models were combined together and subtracted from the datacube.

2. An empirical model of the PSF was created directly from the quasar light by summing up spectral regions virtually free of any extended emission, i.e., $>2500\,\mathrm{km\,s^{-1}}$ from the wavelength of the Lyα line redshifted to the quasar's systemic redshift.[13] For this procedure, we excluded all channels where the background noise was increased by the presence of bright sky emission lines.

3. In each wavelength layer, the PSF model was rescaled to match the quasar flux measured within a radius of two spatial pixels, assuming that the unresolved emission of the AGN dominates within this region.

4. Following a procedure similar to those in, e.g., Hennawi & Prochaska (2013), Arrigoni Battaia et al. (2015b), and Farina et al. (2017), we created a smoothed $\chi_{x,y,\lambda}$ cube defined as:

$$\mathrm{SMOOTH}[\chi_{x,y,\lambda}]$$
$$= \frac{\mathrm{CONVOL}[\mathrm{DATA}_{x,y,\lambda} - \mathrm{MODEL}_{x,y,\lambda}]}{\sqrt{\mathrm{CONVOL}^2[\sigma^2_{x,y,\lambda}]}}, \qquad (2)$$

where $\mathrm{DATA}_{x,y,\lambda}$ is the datacube, $\mathrm{MODEL}_{x,y,\lambda}$ is the PSF model created in the step above, and $\sigma_{x,y,\lambda}$ is the square root of the variance datacube. The operation CONVOL is a convolution with a 3D Gaussian kernel with $\sigma_{\mathrm{spat}} = 0\rlap{.}''2$ in each spatial direction and $\sigma_{\mathrm{spec}} = 2.50\,\text{Å}$ in the spectral direction, and CONVOL^2 denotes a convolution with the square of the smoothing kernel used in CONVOL.

5. To identify significant extended emission, we then ran a friends-of-friends algorithm that connects voxels that have signal-to-noise ratio (S/N) > 2 in the $\mathrm{SMOOTH}[\chi_{x,y,\lambda}]$ cube. We chose a linking length of two voxels (in both spatial and spectral directions). Voxels located within the effective radius of a removed foreground source were excluded.[14] Additionally, voxels contaminated by instrumental artifacts were also excluded. We consider a group identified by this algorithm as a halo associated with the quasar if, at the same time: (i) there is at least one voxel with S/N > 2 within a radius of $1''$ in the spatial direction and within $\pm 250\,\mathrm{km\,s^{-1}}$ in the spectral direction from the expected location of the Lyα emission of the quasar; (ii) it contains more than 300 connected voxels[15]

(this was empirically derived to avoid contaminations from cosmic rays and/or instrument artifacts not fully removed by the pipeline); and (iii) it spans more than two consecutive channels in the spectral direction.

6. If a halo is detected, we created a three-dimensional mask containing all connected voxels ($\mathrm{MASK}_{x,y,\lambda}$) and used it to extract information from the $\mathrm{DATA}_{x,y,\lambda} - \mathrm{MODEL}_{x,y,\lambda}$ cube.

In Figure 2, we show the results of this procedure applied to the REQUIEM survey data set. For each object, we plot a $11'' \times 11''$ (roughly $60\,\mathrm{pkpc} \times 60\,\mathrm{pkpc}$ at $z = 6$) pseudo-narrowband image centered at the quasar location. The spectral region of the cube defining each narrowband image was set by the minimum ($\lambda_{\mathrm{min}}^{\mathrm{mask}}$) and maximum ($\lambda_{\mathrm{Max}}^{\mathrm{mask}}$) wavelengths covered by $\mathrm{MASK}_{x,y,\lambda}$ (see Table 2). The black contours highlight regions where significant (as described above) extended emission was detected.

In summary, we report the presence of 12 Lyα nebulae around $z > 5.7$ quasars, eight of which are newly discovered. In the following, we describe the procedure used to extract physical information about each detected nebula.

4.1. Spectra of the Extended Emission

We extract the nebular emission spectrum using a 2D mask obtained by collapsing $\mathrm{MASK}_{x,y,\lambda}$ along the spectral axis. The construction of a halo mask described in the previous section is instrumental in obtaining the highest S/N spectrum of a detected halo. However, given that this procedure is based on a fix cut in S/N per voxel, it inevitably results in a loss of information at larger radii. For each halo, we thus also extract a spectrum from the circular aperture with radius equal to the distance between the quasar and the most distant significant voxel detected in the collapsed $\mathrm{MASK}_{x,y,\lambda}$ ($d_{\mathrm{QSO}}^{\mathrm{mask}}$; see Table 2). Spectra extracted over the collapsed mask and over the circular aperture (plotted in red and yellow, respectively, in Figure 3) have similar shapes, but the latter shows a systematically higher flux density at each wavelength.

We estimate the central wavelength (λ_{c}) as a nonparametric flux-and-error–weighted mean of the emission between $\lambda_{\mathrm{min}}^{\mathrm{mask}}$ and $\lambda_{\mathrm{Max}}^{\mathrm{mask}}$ (see Table 2 and Figure 3), i.e., without assuming any particular shape for the Lyα line. While Table 3 reports only measurements from the *masked* spectrum, we point out that the central wavelengths measured from the 2D masks and from the circular aperture extraction are consistent within the errors, with an average difference of only $(-5 \pm 37)\,\mathrm{km\,s^{-1}}$. In order to reduce the effects of noise spikes, the FWHMs of the nebular emission were estimated after smoothing spectra extracted from the 2D masks with a Gaussian kernel of $\sigma = 2.5\,\text{Å}$. The derived FHWMs are shown as gray horizontal bars in Figure 3 and listed in Table 3. Finally, total fluxes were calculated by integrating the spectra extracted over the circular apertures between $\lambda_{\mathrm{min}}^{\mathrm{mask}}$ and $\lambda_{\mathrm{Max}}^{\mathrm{mask}}$. If a nebula was not detected, we extracted the spectrum over a circular aperture with a fixed radius of 20 pkpc (corresponding to $3\rlap{.}''5$ at $z = 6$). From this, we derived the 1σ detection limit as $\sigma_{\mathrm{Lim}}^2 = \sum_{-500\,\mathrm{km\,s^{-1}}}^{+500\,\mathrm{km\,s^{-1}}} \sigma_\lambda^2 / N_\lambda$, where σ_λ^2 is the variance at each wavelength and N_λ is the number of spectral pixels in the $\pm 500\,\mathrm{km\,s^{-1}}$ stretch from the quasar's systemic redshift.

---

[12] By construction, we are following the average starlight emission profile of a galaxy. However, nebular line emission can extend on larger scales, and thus is not reproduced well by our empirical model. We also stress that the expected improvement in seeing with wavelength ($\propto \lambda^{-0.2}$) has a negligible impact in the spectral range we are considering.

[13] In Farina et al. (2017), we showed that PSF models created from nearby stars and directly from the quasar itself provide similar results in terms of detecting extended emission.

[14] The empirical procedure used to remove foreground sources intrinsically conceals information (possibly) present at their center. We thus decided to mask these regions to avoid false detections and/or bias estimates of the halo properties. However, this may result in an underestimate of the total halo emission.

[15] As a rule of thumb, for a spatially unresolved source, 300 voxels correspond to a cylinder with a base of $1.5\,\mathrm{arcsec}^2$ and a height of $160\,\mathrm{km\,s^{-1}}$.
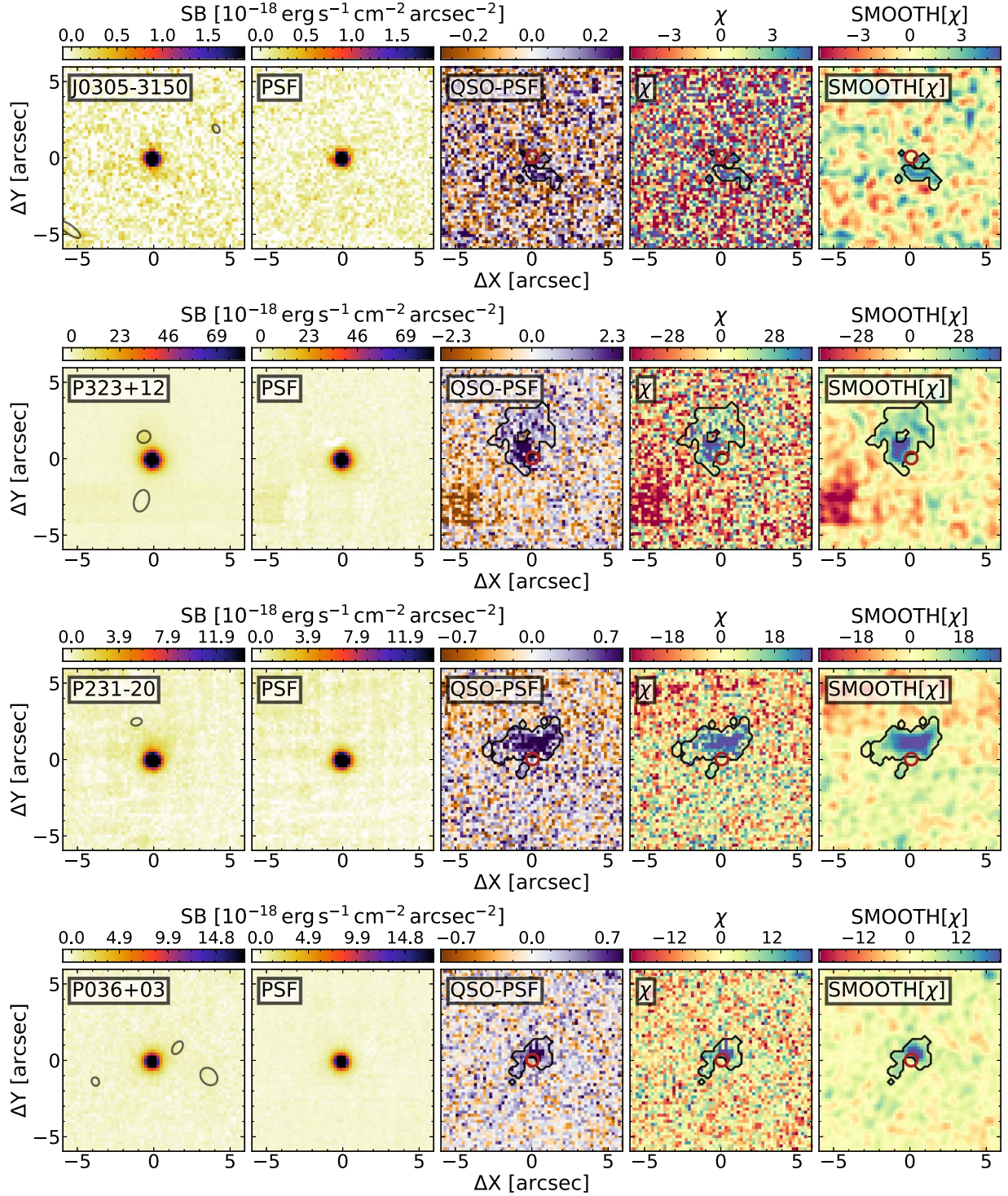
Figure 2. Results from the PSF-subtraction procedure described in Section 4. The different panels show the pseudo-narrowband images obtained by collapsing (from left to right) the $DATA_{x,y,\lambda}$, $MODEL_{x,y,\lambda}$, $DATA_{x,y,\lambda} - MODEL_{x,y,\lambda}$, $\chi_{x,y,\lambda}$, and $SMOOTH[\chi_{x,y,\lambda}]$ cubes in the wavelength range where extended emission was detected. If no significant nebular emission is present, the collapsed region is between -500 and $+500$ km s^{-1}. Black contours are constructed by collapsing $MASK_{x,y,\lambda}$ along the velocity axis. These are the regions used to extract the spectra of the halos in Section 4.1. In the left-most panel, the location of the detected (and removed) foreground sources are marked as gray ellipses. Note that saturation spikes from nearby bright stars (e.g., in the bottom left corner of the quasar P323+12, or on the top of J1509−1749) and/or instrumental artifacts such as IFU-to-IFU edge effects (e.g., for the quasars P183+05 and P217−16) have been masked during the halo identification procedure but are still shown here. (An extended version of this figure is available.)

4.2. Surface Brightness Profiles

The right-hand panels of Figure 3 show circularly averaged surface brightness profiles of the extended emission around each quasar. These are extracted from pseudo-narrowband images constructed by summing up spectral channels located between -500 and $+500$ km s^{-1} of the quasar's systemic redshift. The choice of a fixed width for the entire sample facilitates a uniform comparison of both detections and

Table 2
Summary of MASK$_{x,y,\lambda}$ Properties of Identified Nebulae

ID	λ_{min}^{mask}–λ_{max}^{mask} (Å)	d_{Max}^{mask} (″/pkpc)	d_{QSO}^{mask} (″/pkpc)	A_{Halo}^{mask} (arcsec^2)	d_{QSO}^{fix} (″/pkpc)
J0305−3150	9255.0–9265.0	3.1/16.8	2.5/13.5	1.8	1.3/7.2
P323+12	9182.5–9248.8	4.6/24.7	3.7/20.2	8.6	3.6/19.7
P231−20	9200.0–9253.8	5.1/27.6	3.1/16.8	7.8	2.8/15.3
P036+03	9150.0–9178.8	3.6/19.4	1.8/9.9	2.8	1.5/8.1
J2318−3113	⋯	⋯	⋯	⋯	⋯
P183+05	⋯	⋯	⋯	⋯	⋯
J0210−0456	⋯	⋯	⋯	⋯	⋯
J2329−0301	9003.8–9036.3	4.0/22.3	2.0/11.2	6.9	1.7/9.1
J1152+0055	⋯	⋯	⋯	⋯	⋯
J2211−3206	⋯	⋯	⋯	⋯	⋯
J0142−3327	⋯	⋯	⋯	⋯	⋯
J0100+2802	⋯	⋯	⋯	⋯	⋯
J1030+0524	8870.0–8897.5	6.1/34.0	3.7/20.7	10.3	1.3/7.3
P308−21	8781.3–8826.3	7.7/43.2	4.9/27.4	18.2	2.0/11.3
P065−26	8701.3–8756.3	4.4/24.7	2.7/15.0	7.2	1.4/8.0
P359−06	8700.0–8745.0	3.0/16.9	1.6/9.1	2.7	1.6/8.8
J2229+1457	⋯	⋯	⋯	⋯	⋯
P217−16	⋯	⋯	⋯	⋯	⋯
J2219+0102	⋯	⋯	⋯	⋯	⋯
J2318−3029	⋯	⋯	⋯	⋯	⋯
J1509−1749	⋯	⋯	⋯	⋯	⋯
J2216−0016	⋯	⋯	⋯	⋯	⋯
J2100−1715	⋯	⋯	⋯	⋯	⋯
J2054−0005	⋯	⋯	⋯	⋯	⋯
P340−18	8470.0–8548.8	3.2/18.4	2.6/14.6	3.0	1.8/10.5
J0055+0146	⋯	⋯	⋯	⋯	⋯
P009−10	8508.8–8521.3	2.7/15.4	1.5/8.6	1.4	1.4/8.2
P007+04	⋯	⋯	⋯	⋯	⋯
J2228+0110	8356.3–8416.3	5.2/29.7	2.8/16.0	10.2	2.1/12.2
J1044+0125	⋯	⋯	⋯	⋯	⋯
J0129−0035	⋯	⋯	⋯	⋯	⋯

Note. For each detected nebula, we report the spectral range where significant emission was detected (λ_{min}^{mask}–λ_{max}^{mask}), along with its maximum extent projected on the sky (d_{Max}^{mask}), the distance between the quasar and the furthest significant voxel (d_{QSO}^{mask}), and the total area covered by the mask (A_{Halo}^{mask}, see Section 4 for further details). In addition, we also list the distance form the quasar where the circularly averaged surface brightness profile drops below a limit of $(1 + z)^4 \times 3 \times 10^{-18}$ erg s^{-1} cm^{-2} arcsec^{-2} (d_{QSO}^{fix}; see Section 4.2).

nondetections of nebular emission. In addition, this velocity range corresponds to 30 Å, roughly matching the width of the pseudo-narrowband images used to extract surface brightness profiles by Arrigoni Battaia et al. (2019a) and by Cai et al. (2019) for their samples of $z \sim 2$–3 quasars. However, the size of the bin selected by Arrigoni Battaia et al. and by Cai et al. is twice as large as ours in velocity space. This is also much narrower than previous narrowband studies targeting high-redshift quasars: e.g., ∼100 Å in Decarli et al. (2012) or ∼160 Å in Momose et al. (2019). Although this choice may lead to the loss of some signal from the wings of the nebulae, it allows us to optimize the S/N of the extended emission while still being sensitive to faint emission that may be present at larger scales. Before extracting the profile binned in annuli with radii evenly spaced in logarithmic space, we masked regions where apparent instrumental artifacts were present and regions located within the effective radius of the removed foreground sources. Errors associated to each bin of the surface brightness profile were estimated from the collapsed variance datacube.

In addition, from the pseudo-narrowband images, we also derive a noise-independent measurement of the size of the nebulae (d_{QSO}^{fix}, see Table 2). This is the distance from a quasar where the circularly averaged surface brightness profile drops below a surface brightness of $(1 + z)^4 \times 3 \times 10^{-18}$ erg s^{-1} cm^{-2} arcsec^{-2}. This value has been chosen to have $d_{QSO}^{fix} \approx d_{QSO}^{mask}$ for data collected with the shortest exposure times.

4.3. Moment Maps

In order to trace the kinematics of the detected extended emission, we produced the zeroth, first, and second-moment maps of the flux distribution in velocity space (see Figure 4). These maps encode information about the variation of the line centroid velocity and width at different spatial locations. To create the maps, we first smoothed each wavelength layer with a 2D Gaussian kernel with $\sigma = 1$ spatial pixel. We then extracted the different moments within the MASK$_{x,y,\lambda}$ region (i.e., only voxels significantly associated with the halo are included in the maps). Given the complex kinematics of the Lyα emission observed around high-redshift quasars (e.g., Martin et al. 2015; Borisova et al. 2016; Arrigoni Battaia et al. 2018b, 2019a; Ginolfi et al. 2018; Drake et al. 2019) and the relatively low spectral resolution of MUSE, the moments are estimated in a nonparametric way by flux-weighting each voxel. In other words, no assumption was made about the 3D shape of the line-emitting region.
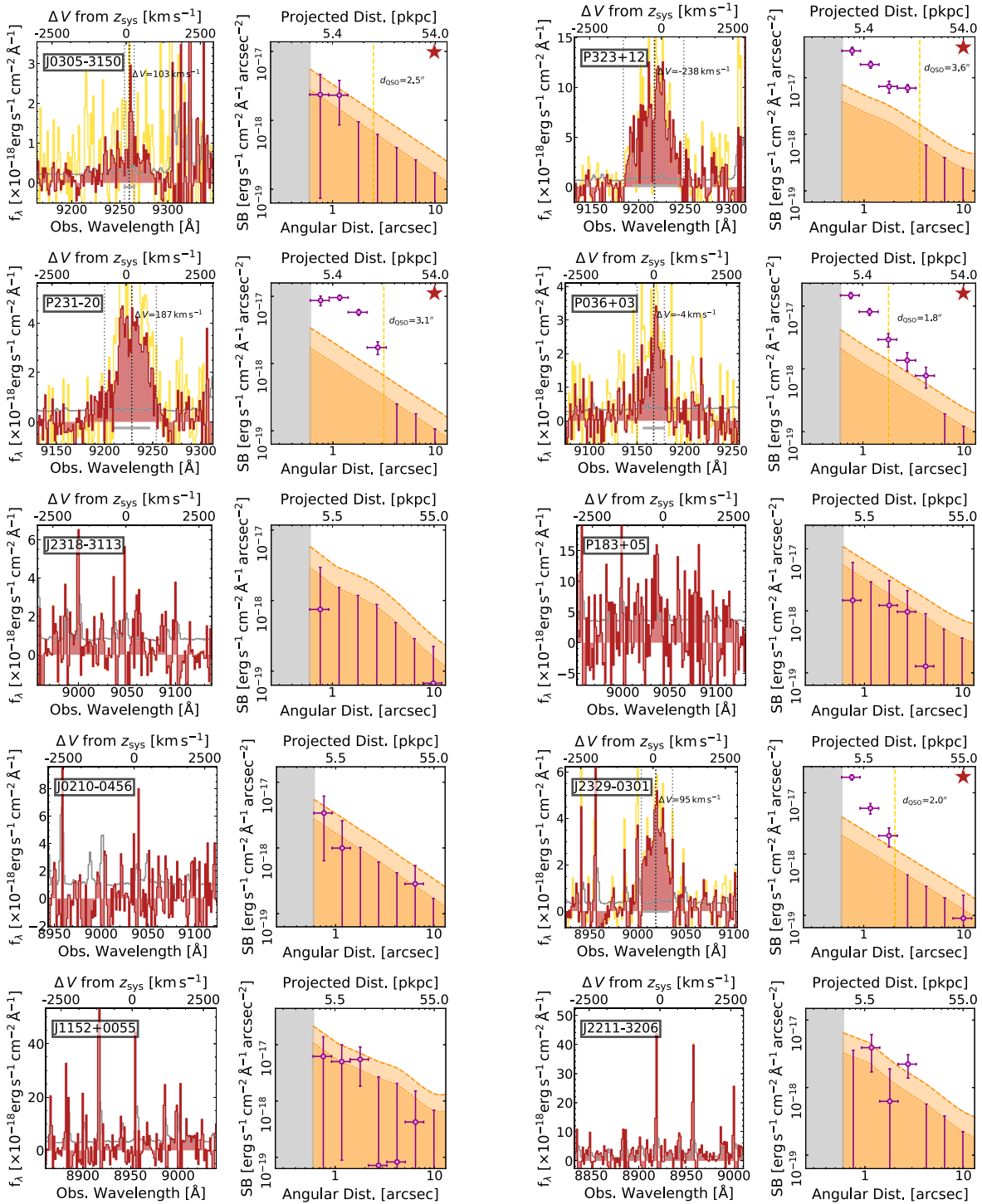
Figure 3. Atlas of spectra and surface brightness profiles of extended emission detected in the REQUIEM survey. Left-hand panel: spectrum of the nebular emission extracted over the collapsed halo mask as described in Section 4.1 (red shaded histogram) with corresponding 1σ error (gray histogram). The spectrum extracted over a circular aperture of radius d_{QSO} is also shown as a yellow histogram. Vertical dotted lines mark the wavelength range where the extended emission was detected and the location of its flux-weighted centroid. In the cases where no halo was detected, the spectrum extracted from a circular aperture of radius 20 pkpc is plotted. Right-hand panel: surface brightness profile extracted over circular annuli evenly spaced in logarithmic space (purple points). The formal 1 and 2σ errors in surface brightness are plotted as orange shaded regions (see Section 4.2 for further details). Stars in the top right corners indicate objects for which significant extended emission has been detected.

5. Results and Discussion

The analysis of the fields of the 31 quasars that constitute the REQUIEM survey revealed the presence of extended Lyα emission around ∼39% of the sample (12 out of 31 targets, 11/ 23 considering only our *core sample*). At face value, this detection rate is lower than the 100% reported for $z \sim 3$ quasars by Borisova et al. (2016) and Arrigoni Battaia et al. (2019a). However, only ∼50% of the Arrigoni Battaia et al. (2019a) sample would be detected if their surface brightness limit were rescaled to compensate for the effects of the
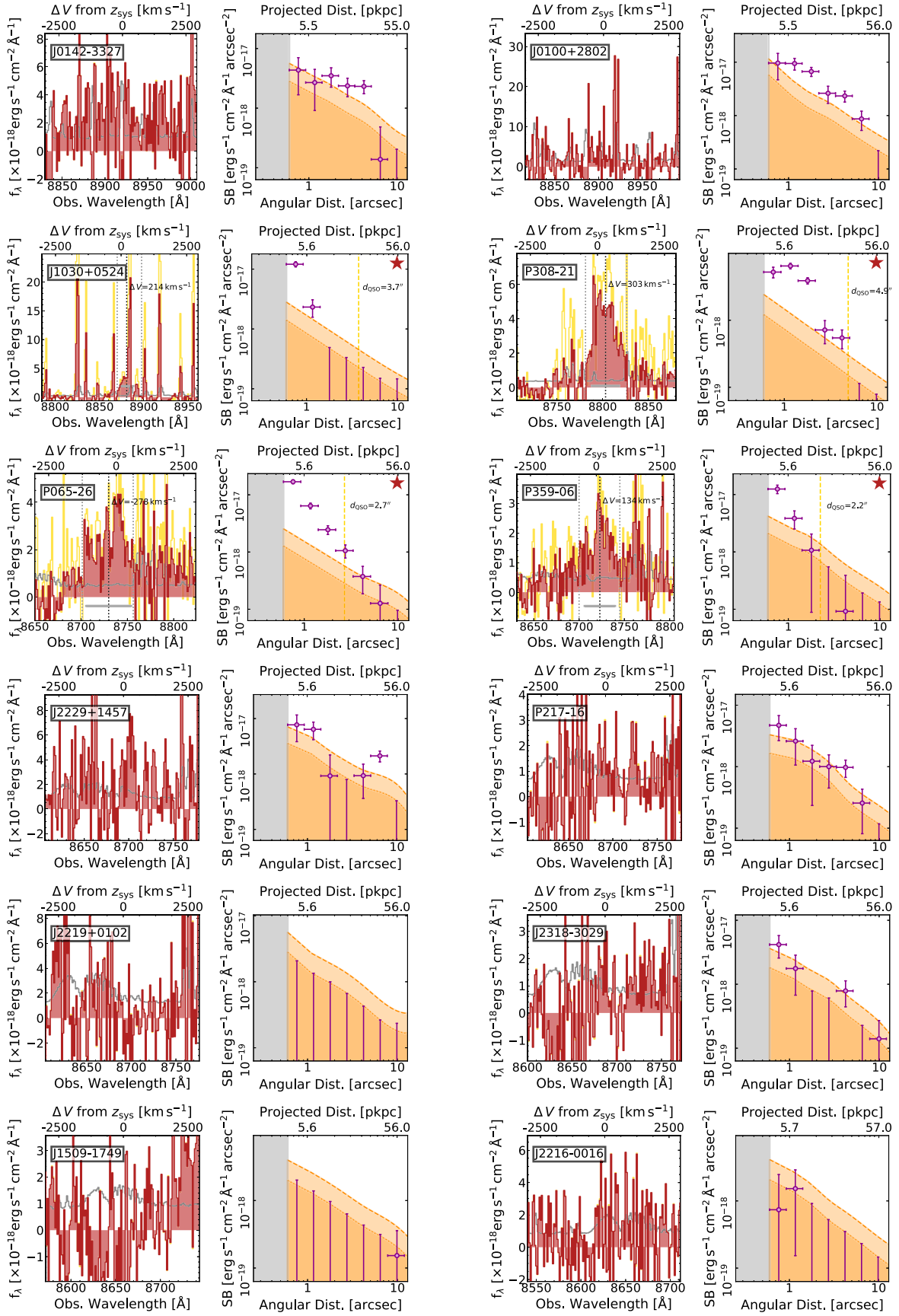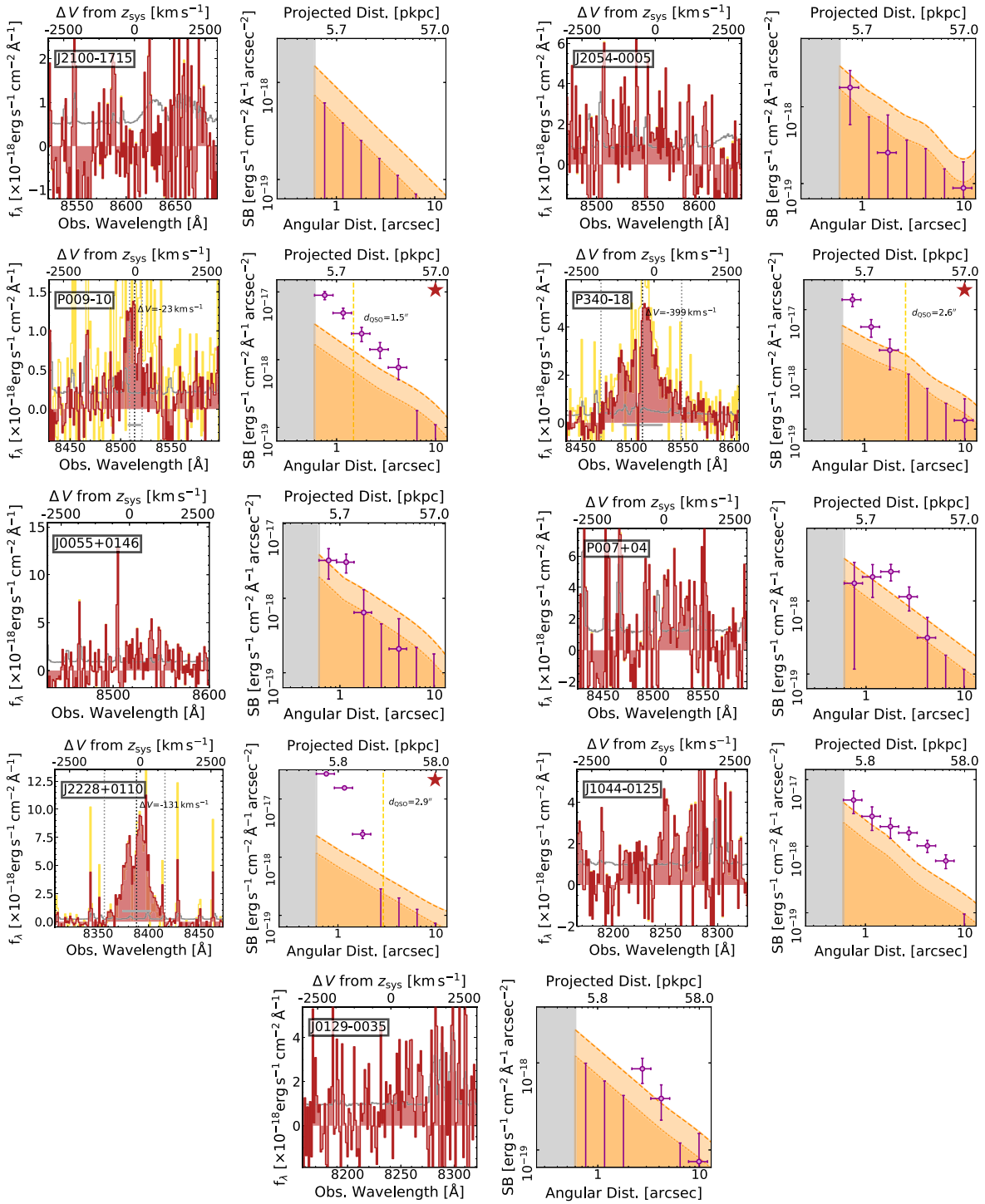
Figure 3. (Continued.)

Figure 3. (Continued.)

cosmological dimming (a factor of $\sim 10\times$ from $z \sim 3$ to $z \sim 6$). The nebulae detected at $z \sim 6$ show a variety of morphologies and properties, spanning a factor of 25 in luminosity (from 8×10^{42} to 2×10^{44} erg s^{-1}), have FWHM ranging from ~ 300 to ~ 1700 km s^{-1}, and maximum sizes from ~ 8 to ~ 27 pkpc. In the following, we investigate the origin of this emission, relate it to the properties of the central powering source, and compare with lower-redshift samples.

5.1. Extended Halos and Quasar Host Galaxies

Direct detections of the stars of the host galaxy of the first quasars still elude us (e.g., Decarli et al. 2012; Mechtley et al. 2012; see also our Appendix C). On the other hand, gas and dust in the interstellar medium are routinely detected at mm and submm wavelengths. For instance, for all but two quasars in our sample (i.e., J2228+0110, and P340−18), sensitive measurements of the [C II] 158 μm emission line and of the

Table 3
Spectral Properties of the Extended Emission

ID	$\lambda_{c,Ly\alpha}$ (Å)	$z_{Ly\alpha}$	$\mathrm{FWHM}_{Ly\alpha}$ (km s^{-1})	$F_{Ly\alpha}$ (10^{-17} erg s^{-1} cm^{-2})	$L_{Ly\alpha}$ (10^{43} erg s^{-1})
J0305−3150	9259.9 ± 1.0	6.6171 ± 0.0008	325 ± 85	1.6 ± 0.4	0.8 ± 0.2
P323+12	9217.2 ± 2.2	6.5819 ± 0.0018	1385 ± 145	40.5 ± 1.2	20.1 ± 0.6
P231−20	9228.3 ± 1.9	6.5911 ± 0.0016	1180 ± 85	22.2 ± 0.6	11.0 ± 0.3
P036+03	9167.5 ± 1.6	6.5411 ± 0.0013	695 ± 90	7.8 ± 0.4	3.8 ± 0.2
J2318−3113	...	...	...	<0.4	<0.2
P183+05	...	...	...	<1.2	<0.6
J0210−0456	...	...	...	<0.5	<0.2
J2329−0301	9018.8 ± 1.7	6.4188 ± 0.0014	830 ± 60	11.0 ± 0.3	5.1 ± 0.1
J1152+0055	...	...	...	<2.1	<0.9
J2211−3206	...	...	...	<0.9	<0.4
J0142−3327	...	...	...	<0.6	<0.3
J0100+2802	...	...	...	<1.0	<0.5
J1030+0524	8880.3 ± 1.5	6.3048 ± 0.0012	590 ± 120	5.6 ± 0.7	2.5 ± 0.3
P308−21	8803.2 ± 1.7	6.2414 ± 0.0014	1020 ± 60	20.3 ± 0.7	8.8 ± 0.3
P065−26	8729.8 ± 2.3	6.1810 ± 0.0019	1675 ± 90	15.4 ± 0.6	6.6 ± 0.2
P359−06	8722.8 ± 1.9	6.1753 ± 0.0016	1160 ± 330	7.8 ± 0.4	3.3 ± 0.2
J2229+1457	...	...	...	<0.4	<0.2
P217−16	...	...	...	<0.3	<0.1
J2219+0102	...	...	...	<0.5	<0.2
J2318−3029	...	...	...	<0.3	<0.1
J1509−1749	...	...	...	<0.4	<0.2
J2216−0016	...	...	...	<0.5	<0.2
J2100−1715	...	...	...	<0.2	<0.1
J2054−0005	...	...	...	<0.3	<0.1
P340−18	8510.5 ± 2.5	6.0007 ± 0.0020	1320 ± 155	18.8 ± 0.8	7.5 ± 0.3
J0055+0146	...	...	...	<0.3	<0.1
P009−10	8513.8 ± 1.2	6.0033 ± 0.0010	395 ± 60	2.3 ± 0.2	0.9 ± 0.1
P007+04	...	...	...	<0.5	<0.2
J2228+0110	8388.0 ± 1.7	5.8999 ± 0.0014	940 ± 65	20.3 ± 0.4	7.8 ± 0.1
J1044+0125	...	...	...	<0.3	<0.1
J0129−0035	...	...	...	<0.3	<0.1

Note. The reported central wavelengths ($\lambda_{c,Ly\alpha}$) and FWHMs ($\mathrm{FWHM}_{Ly\alpha}$) are derived from the spectrum of the nebular emission extracted from the collapsed $\mathrm{MASK}_{x,y,\lambda}$ as described in Section 4.1. The total fluxes ($F_{Ly\alpha}$) are instead derived from spectra extracted over a circular aperture of radius d_{QSO}^{mask}. In the cases of nondetections, 3σ limits on fluxes are reported.

underlying far-infrared continuum have been collected; see Decarli et al. (2018), Venemans et al. (2018), and references therein. These observations provide direct insights regarding the properties of the host galaxies—including, among others, precise systemic redshifts, dynamics of the gas, and star formation rates. In the following, we will test for connections between these properties of quasar host galaxies and the extended Lyα halos where they reside.

5.1.1. Velocity Shifts with Respect to the Systemic Redshifts

We first estimate the velocity difference (ΔV_{sys}) between the flux-weighted centroid of the extended emission and the precise systemic redshift of the quasar host galaxies provided by the [C II] 158 μm line. If no measurement of the [C II] 158 μm emission line is available in the literature (see Table 1), we consider systemic redshifts from the quasar broad Lyα or Mg II emission lines—including the empirical correction for Mg II-based systemic redshifts from Shen et al. (2016). The velocity difference is defined as:

$$\Delta V_{sys} = \frac{c(z_{Ly\alpha} - z_{sys})}{1 + z_{sys}} \qquad (3)$$

where c is the speed of light. This means that a positive ΔV_{sys} corresponds to a halo shifted redward of the systemic redshift.

All the detected halos have velocity shifts between $\Delta V_{sys} = -500$ and $+500$ km s^{-1}, with an average $\langle \Delta V_{sys} \rangle = (+71 \pm 31)$ km s^{-1} and a median of $+54$ km s^{-1}. This value agrees with $\langle \Delta V_{sys} \rangle = (+69 \pm 36)$ km s^{-1} (with a median of $+112$ km s^{-1}) calculated taking only [C II] 158 μm redshifts into account (see the left-hand panel of Figure 5). These small velocity differences hint at a strong connection between the extended halos and $z \sim 6$ quasar host galaxies. Much larger shifts are reported for Lyα nebulosities around intermediate-redshift quasars. For instance, Borisova et al. (2016) measured a median shift of 1821 km s^{-1} in a sample of bright $3 \lesssim z \lesssim 4$ quasars. Similarly, in their sample of 61 $z \sim 3$ quasars, Arrigoni Battaia et al. (2019a) reported a large shift between Lyα halos and their best estimates of the quasar systemic redshifts, with a median of 782 km s^{-1}. We argue that the discrepancy between intermediate- and high-redshift halos is related to the large intrinsic uncertainties in the C IV-based systemic redshifts used in Borisova et al. and in Arrigoni Battaia et al. (on the order of ~400 km s^{-1}; e.g., Richards et al. 2002; Shen et al. 2016). Indeed, the median shift for the sample of Arrigoni Battaia et al. (2019a) reduces to 144 km s^{-1} when the peak of the broad Lyα line of the $z \sim 3$ quasars themselves is used as a tracer of the systemic redshift. This matches the median shift between the halo and the [C II] 158 μm redshifts observed in the REQUIEM sample.
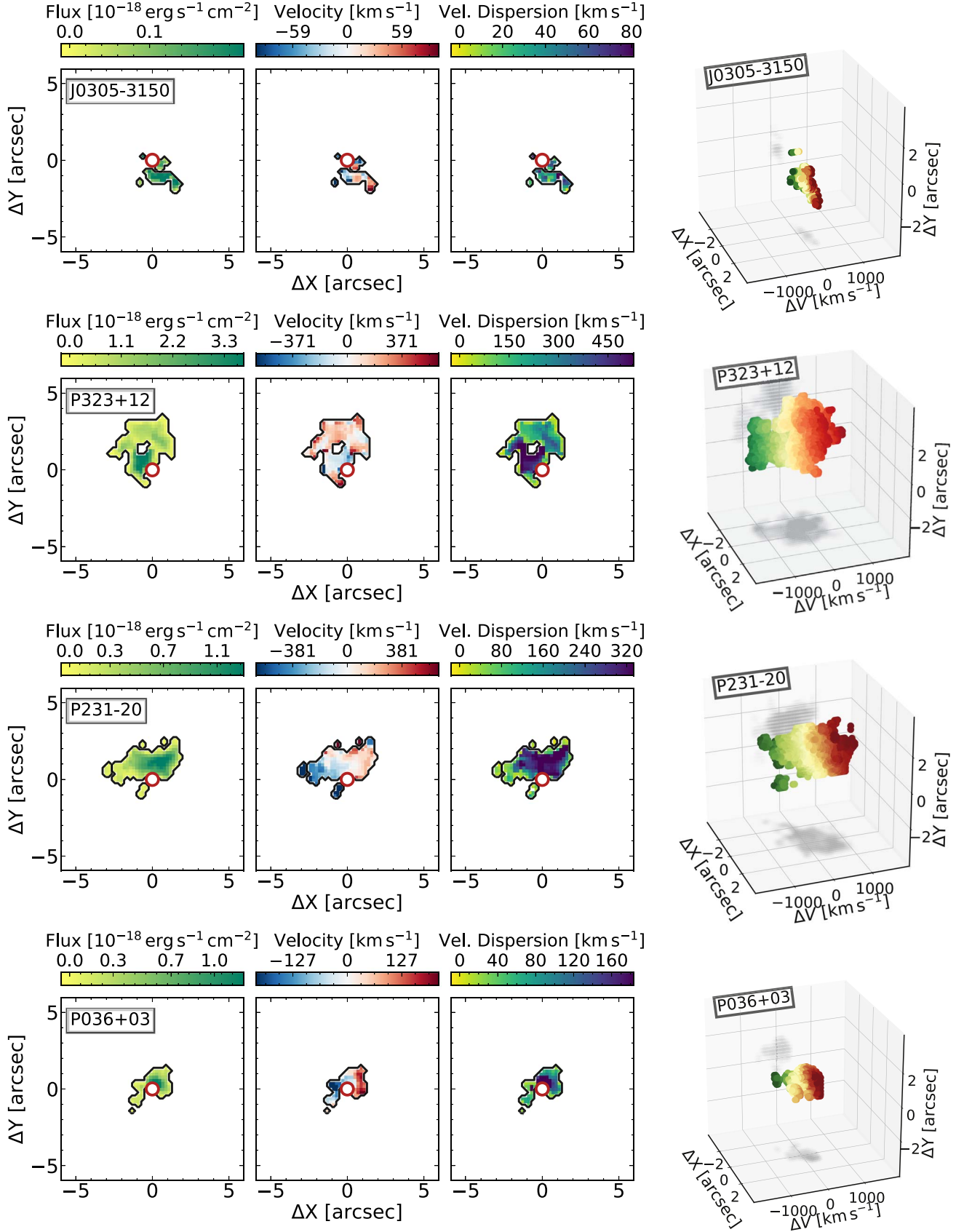
Figure 4. Spatially resolved kinematics of the halos detected in our sample. From left to right: integrated flux (zeroth-moment), velocity field with respect to the flux-weighted centroid of the line emission (first-moment), and velocity dispersion (second-moment). These maps were obtained as described in Section 4.3. Note that the maps are not corrected for the finite spectral resolution of MUSE. In the wavelength range explored by our sample, this washes away any information with $\sigma \lesssim 35 \text{ km s}^{-1}$. The right-most column shows the 3D visualization of each nebula. Here, ΔX goes from east to west, ΔY from south to north, and ΔV from green to red, with respect to the centroid of the extended emission.
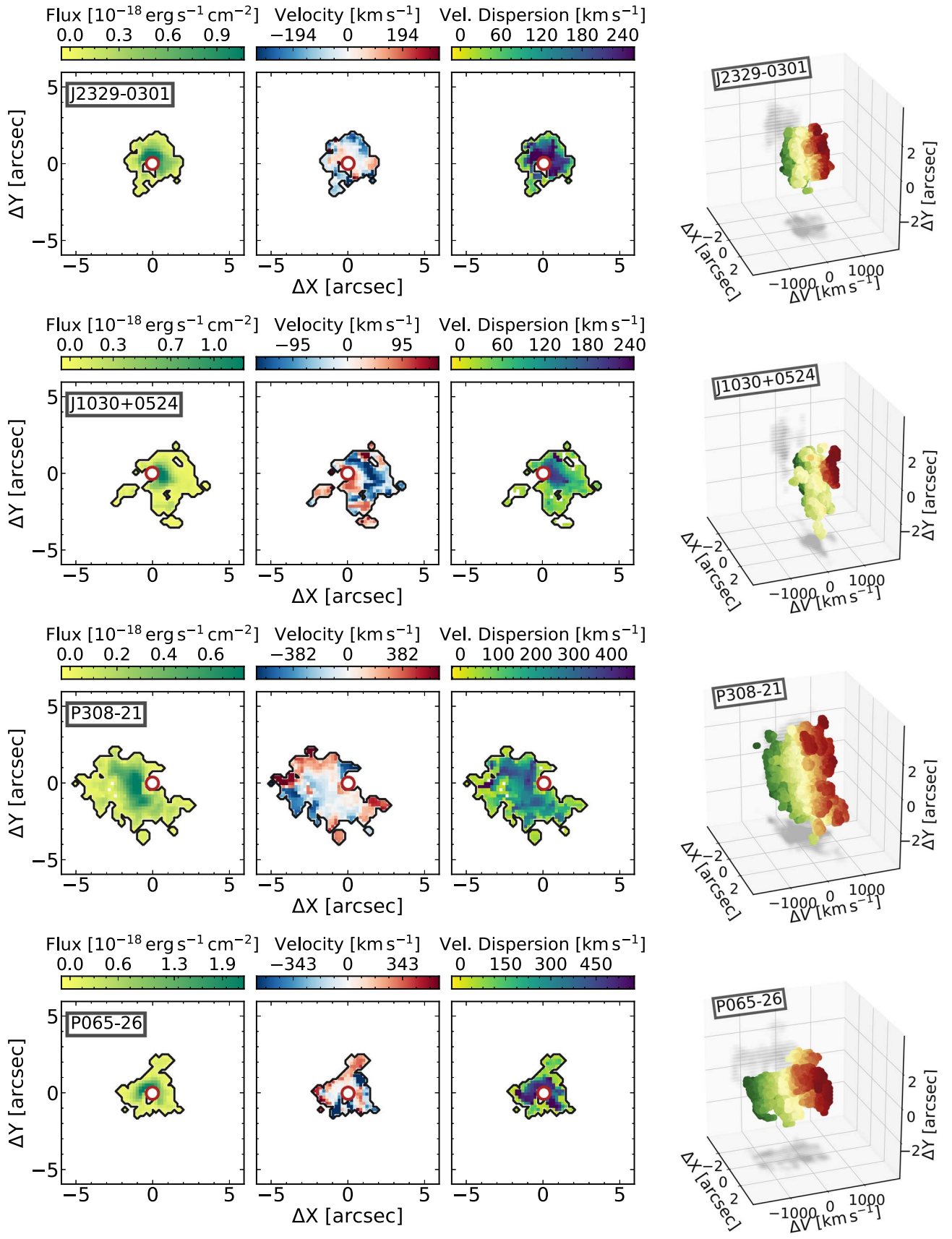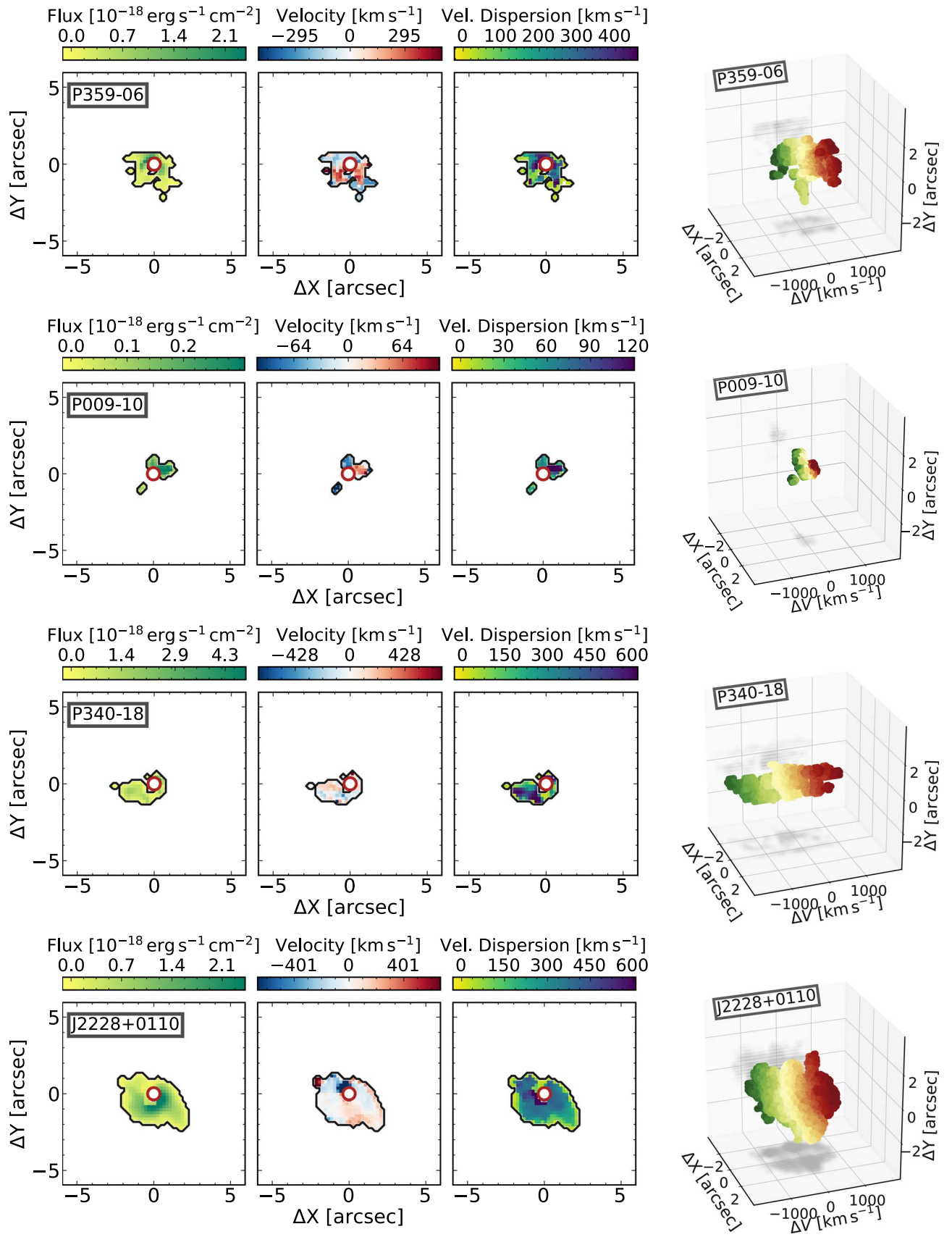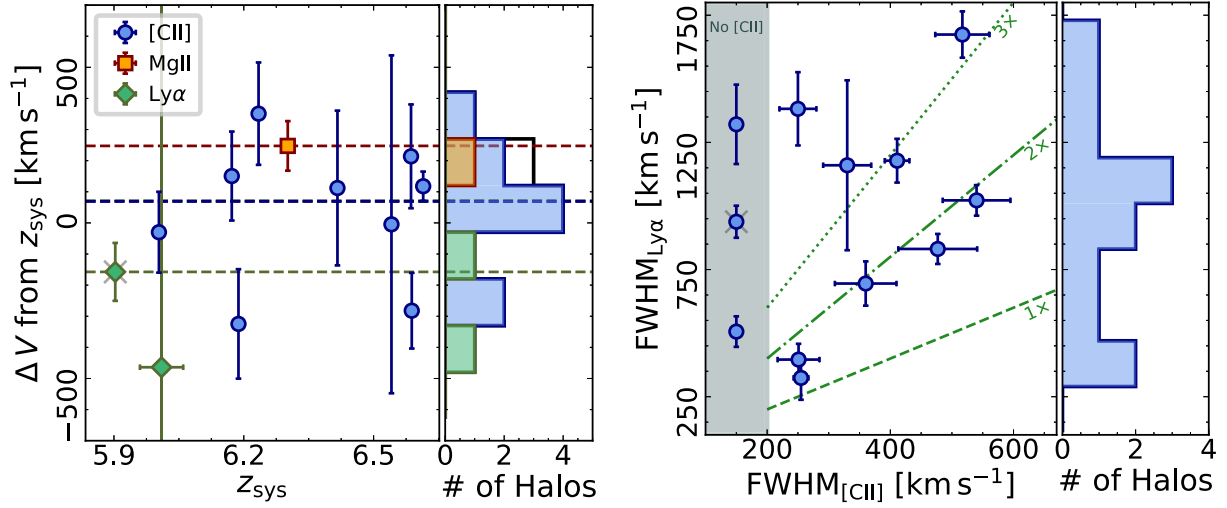
Figure 4. (Continued.)

Figure 4. (Continued.)

Figure 5. Left panel: velocity difference between the flux-weighted centroid of the nebular emission and the systemic redshift of the quasar (see Equation (3)). Different symbols indicate different emission lines used to derive the quasar redshifts (i,e, blue points for [C II] 158 μm, orange squares for Mg II, and green diamonds for Lyα; see Table 1 for details). Horizontal dashed lines indicate the weighted average velocity difference of the different lines. The error-weighted average shift calculated for the entire sample is $\langle \Delta V_{sys} \rangle = (+71 \pm 31)$ km s^{-1}. This is shown as a black dashed line that overlaps with the average estimated from the [C II] 158 μm redshifts only. Histograms on the left-hand side of this panel display the distribution of the shifts, color-coded as on the right-hand side. Right panel: comparison between the FWHM of the detected extended Lyα emission (FWHM$_{Ly\alpha}$) and of the [C II] 158 μm line arising from the quasar's host galaxy (FWHM$_{C[II]}$). To guide the eye, green lines mark FWHM$_{Ly\alpha}$ that are 1, 2, and 3× wider than FWHM$_{C[II]}$. The wide distribution of the FWHM$_{Ly\alpha}$ (ranging from $\sim$250 to $\sim$1750 km s^{-1}) is apparent in the histogram on the left-hand side of this panel. In both panels, gray crosses mark targets that are not part of our *core sample* (see Section 2).

5.1.2. FWHM of the Extended Emission

The right-hand panel of Figure 5 presents the distribution of FWHM of the detected halos with respect to the [C II] 158 μm lines (FWHM$_{[C II]}$). FWHM$_{Ly\alpha}$ appears to be consistently a factor >2× larger than FWHM$_{[C II]}$. Given that the Lyα and the [C II] 158 μm are tracing different gas components, a different broadening of the two lines is indeed expected. (Sub)arcsecond investigation of [C II] 158 μm emission lines reveled that $z \sim 6$ quasar host galaxies are compact objects with sizes of a few kiloparsecs or less (e.g., Wang et al. 2013; Decarli et al. 2018; Neeleman et al. 2019; Venemans et al. 2019), while extended emission is detected at scales of dozens of kiloparsecs (see Table 2). *Zoom-in* simulations of massive $z > 6$ dark matter halos hosting quasars show that the deep potential well of stellar component dominates the kinematics in the central regions, while dark matter prevails at $\gtrsim 10$ pkpc (e.g., Dubois et al. 2012; Costa et al. 2015), giving rise to the difference between the velocities of the dense gas component traced by the [C II] 158 μm and of the cool gas responsible for the Lyα emission. A direct interpretation of this result is, however, not trivial. The resonant nature of the Lyα line and the turbulent motion of the gas due to interactions and feedback effects are likely to contribute to the broadening of the line emission. Moreover, one can speculate that the presence of cool streams, often invoked to replenish the central galaxy with gas, could contribute to the larger observed FWHM (Di Matteo et al. 2012, 2017; Feng et al. 2014). A more detailed investigation of these different possibilities will be provided in T. Costa et al. (2019, in preparation).

5.1.3. The SFR of the Quasar Host Galaxies

It is tempting to explore the possibility that the intense starbursts observed at mm wavelengths directly influence the powering of the extended Lyα emission. SFR-based Lyα luminosities ($L_{Ly\alpha}^{SFR}$) are expected to follow the linear relation:

$$\frac{L_{Ly\alpha}^{SFR}}{10^{42} \text{ erg s}^{-1}} = 1.62 \frac{\text{SFR}}{M_\odot \text{ yr}^{-1}}, \quad (4)$$

for which we assume the Hα calibration relation (e.g., Kennicutt & Evans 2012) and the case B recombination Lyα-to-Hα line ratio. Star formation rates can be derived either from the [C II] 158 μm emission line or from rest frame far-infrared dust continuum luminosity of the quasar hosts. [C II] 158 μm estimates, however, depend on the (unknown) dust metallicity, especially in the case of compact starbursts (e.g., De Looze et al. 2014). The dust continuum, on the other hand, can be used to estimate SFRs more directly by assuming that the dust is heated by star formation (i.e., considering that the quasar has a negligible contribution to the observed emission Leipski et al. 2014) and that the dust spectral energy distribution is well-parameterized by a modified blackbody with a (typical) temperature of $T_{dust} = 47$ K and a spectral index of $\beta = 1.6$ (Beelen et al. 2006; Barnett et al. 2015). Conveniently, we detected the rest-frame far-infrared dust continuum significantly for all quasars in our sample, except J2228+0110. In the following, we will thus consider SFRs based on the dust continuum from Venemans et al. (2018) and references therein. We stress that, in high-z quasar host galaxies, SFRs derived from [C II] 158 μm and from far-infrared continuum correlate, albeit with a large scatter; see the discussions in, e.g., Decarli et al. (2018) and Venemans et al. (2018).

Figure 6 shows that Lyα luminosities of the extended emission are broadly independent of the SFRs of the quasar host galaxies and are typically well below the expectation based on Equation (4) (shown as a green dashed line). The resonant nature of the Lyα line and the large mass of dust present in the host galaxies ($M_{dust} = 10^7$–10^9 $M_\odot$; Venemans et al. 2018) may be responsible for the suppression of the Lyα
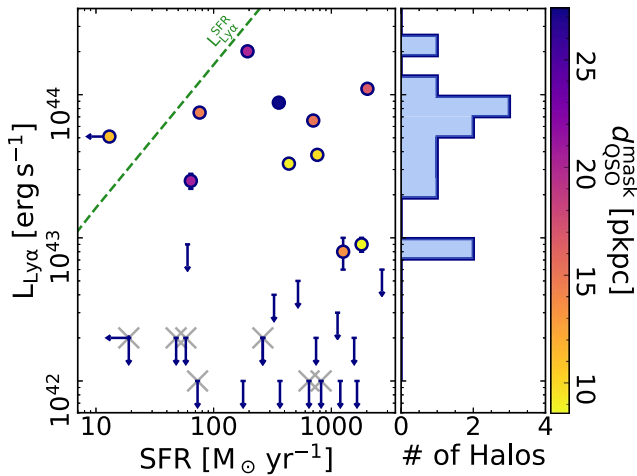
Figure 6. Total Lyα luminosity of the extended halos ($L_{\mathrm{Ly}\alpha}$; see Table 3) vs. star formation rate derived from the dust continuum emission of the quasar host galaxies (SFR). The 3σ upper limits on $L_{\mathrm{Ly}\alpha}$ and on the SFR are shown as downward and leftward arrows, respectively. Different colors show the value of $d_{\mathrm{QSO}}^{\mathrm{mask}}$ (see Table 2). Green dashed line indicates the unobscured Lyα emission expected from UV photons generated in intense starbursts, such as detected at mm wavelengths (Equation (4)). Most of the detected halos have $L_{\mathrm{Ly}\alpha}$ below this prediction. Gray crosses represent quasars that are not part of our *core sample* (see Section 2).

emission. For examples of this process, see Kunth et al. (1998), Verhamme et al. (2006), Gronwall et al. (2007), Atek et al. (2008), and Sobral & Matthee (2019); see also Mechtley et al. (2012) for a study of the host galaxy of the $z \sim 6.4$ quasar J1148+5251. The cumulative effect can be quantified by the so-called Lyα escape fraction ($f_{\mathrm{esc,Ly}\alpha}$; e.g., Kennicutt & Evans 2012). The median value of $f_{\mathrm{esc,Ly}\alpha}$ estimated for our sample is $\lesssim 1\%$. This is an order of magnitude lower than typically reported for $z \sim 6$ LAEs (e.g., Ono et al. 2010; Hayes et al. 2011) but consistent with the most massive, highly star-forming galaxies observed in the 3D-*HST*/CANDELS survey (Oyarzún et al. 2017). However, this value should be considered with some caution. The precise estimate of $f_{\mathrm{esc,Ly}\alpha}$ is strongly affected by different properties of the host galaxy, e.g., neutral hydrogen column density, neutral fraction, geometry, gas-to-dust ratio, etc. (Draine 2011; Hennawi & Prochaska 2013, and references therein), and by the *patchiness* of the dust cocoon (e.g., Casey et al. 2014). In addition, other mechanisms could contribute to the observed Lyα emission, in particular the presence of the strong radiation field generated by the quasar (e.g., Cantalupo et al. 2005; see also our Section 5.3).

5.2. The Kinematics of the Gas

In Figure 4, we presented the two-dimensional flux-weighted maps of the velocity centroid and dispersion distribution of the extended Lyα emission (see Section 4.3 for details). In this section, we investigate these resolved kinematics maps in order to identify signatures of ordered motion, in/outflows, rotations, etc. We remind the reader that these maps were computed in a nonparametric way in the regions identified by MASK$_{x,y,\lambda}$, and that velocity shifts are not relative to the quasar's systemic redshift.
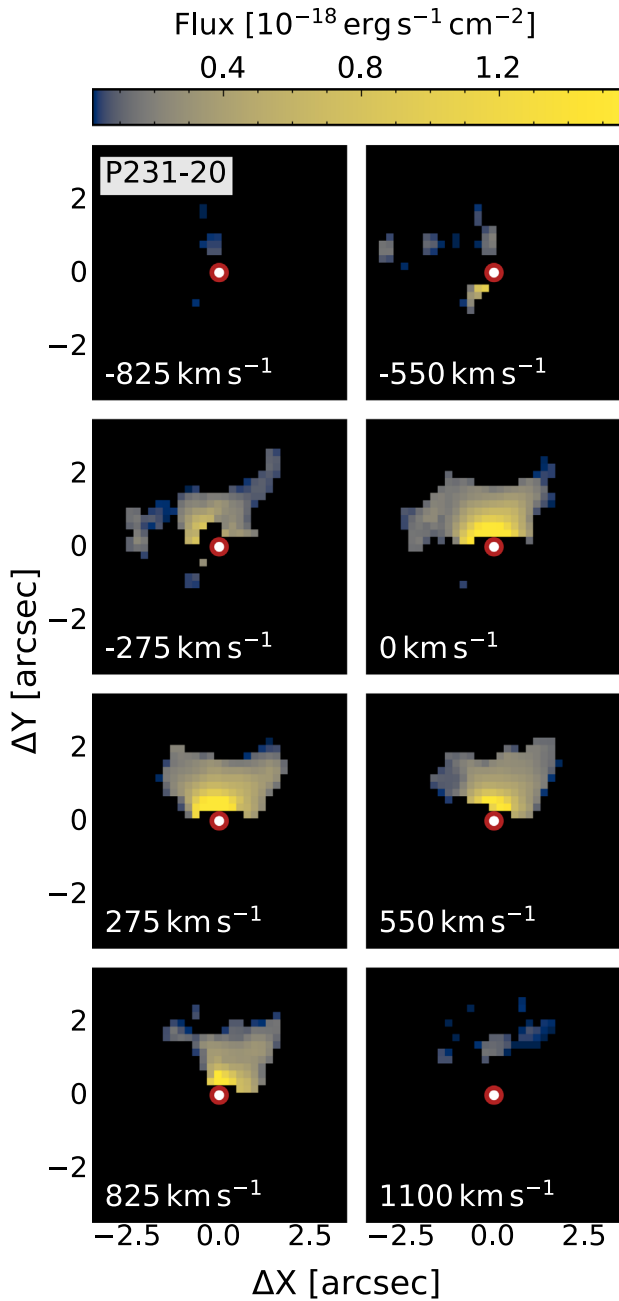
5.2.1. Velocity Fields

The relatively low S/N of the first moment maps (see Figure 4) makes it hard to infer the potential presence of ordered motion in the gas. In addition, due to the resonant nature of the Lyα line, the signature of coherent motion could be hindered by radiative transfer effects (e.g., Cantalupo et al. 2005). Indeed, the majority of the halos identified in the REQUIEM survey do not show evidence of rotation, as it was reported in extended Lyα halos at $z \sim 2$–4 (Borisova et al. 2016; Arrigoni Battaia et al. 2019a; Cai et al. 2019).

A noticeable exception is the nebular emission around the quasar P231−20. A velocity gradient can be seen ranging from -200 to $+800$ km s^{-1} east to west (see Figure 7). Intriguingly, two [C II] 158 μm-bright companions located within $\lesssim 14$ kpc from the quasar host galaxy have been discovered (Decarli et al. 2017; Neeleman et al. 2019). Both the velocity shear and the presence of a rich environment are reminiscent of the enormous Lyα nebular emission observed around the quasar SDSS J1020+1040 at $z = 3.2$ by Arrigoni Battaia et al. (2018b), albeit on a smaller scale. This system is considered a prototype for investigations into the feasibility of inspiraling accretion onto a massive galaxy at $z \sim 3$. Indeed, simulations predict that baryons assemble in rotational structures, gaining angular momentum from their dark matters halos (e.g., Hoyle 1951; Fall & Efstathiou 1980; Mo et al. 1998) and from accretion streams (e.g., Chen et al. 2003; Kereš & Hernquist 2009; Kereš et al. 2009; Brook et al. 2011; Stewart et al. 2017). In this scenario, the cool accreting gas should be able to shape the central galaxy, delivering both fuel for star formation and angular momentum to the central regions (e.g., Sales et al. 2012; Bouché et al. 2013). High-resolution ($\sim 0''35$) observations of the [C II] 158 μm emission of the quasar host galaxy of P231−20 do not show a strong signature of rotation (Neeleman et al. 2019). This supports the idea that the system recently underwent a merger event with the close companion galaxy, located at a separation of 9 kpc and -135 km s^{-1} (Decarli et al. 2017; Neeleman et al. 2019), that perturbed the gas distribution.

If one assumes that the gas in the extended halo of P231−20 is (at first order) gravitationally bound, it is possible to approximate the dynamical mass of the system as $M_{\mathrm{dyn}} = 1.16 \times 10^5 \, v_{\mathrm{circ}} \, d$ where d is the diameter of the nebular emission in pkpc and v_{circ} its circular velocity in km s^{-1}. Given that the gas shows ordered motion, v_{circ} can be expressed as $v_{\mathrm{circ}} = 0.75 \, \mathrm{FWHM}_{\mathrm{Ly}\alpha}/\sin i$, with the (unknown) inclination typically considered to be $i = 55°$. This gives us a dynamical mass of $M_{\mathrm{dyn}} \sim 1.5 \times 10^{13} \, M_\odot$. Notwithstanding the large uncertainties associated with this measurement, the estimated dynamical mass is remarkably similar to the mass predicted for the Lyα emission around the $z = 2.28$ radio-quiet quasar UM287 (Cantalupo et al. 2014).[16] Martin et al. (2015, 2019) interpreted this emission, which extends out to ~ 500 kpc, as a large protogalactic disk. Deeper MUSE observations are, however, necessary to fully capture the complex kinematics of this system.

---

[16] Estimates of the cool gas mass are strongly dependent on the assumed physical conditions of the gas. Combining photoionization models with sensitive searches for He II and C IV extended emission around UM287, Arrigoni Battaia et al. (2015a) derived extreme gas clumping factors (and thus higher densities) and a much lower mass of cool gas present in this nebula: $M_{\mathrm{cool}} \lesssim 6.5 \times 10^{10} \, M_\odot$.

Figure 7. Velocity field of the extended Lyα nebular emission detected around the quasar P231−20, convolved with a 3D Gaussian kernel with $\sigma_{spat} = 0''2$ in the spatial and $\sigma_{spec} = 2.50$ Å in the spectral direction. Zero velocity is set to the [C II] 158 μm redshift of the quasar ($z_{sys} = 6.5864 \pm 0.0005$, while in Figure 4 velocity differences are relative to the flux-weighted centroid of the extended emission). The red circle in the center of each image marks the location of the quasar. Only voxels that are part of $MASK_{x,y,\lambda}$ are shown. Here, ΔX goes from east to west, ΔY from south to north. The bulk of the emission is redshifted with respect to the quasar's systemic redshift, and the nebula shows a velocity gradient going from east to west.

The low incidence of clearly rotating structures in our sample is broadly in agreement with the results of Dubois et al. (2012), who resimulated two massive (0.5 and $2.5 \times 10^{12} M_\odot$) $z \sim 6$ halos. They show that a significant fraction of the gas in the halo can fall almost radially toward the center. The reduced angular momentum inside the virial radius (mostly due to the isotropic distribution of the 0 and to gravitational instabilities

and mergers; see also Prieto et al. 2015) allows for efficient funnelling of gas to the central regions of the halos, potentially sustaining the rapid growth of the first supermassive black holes.

5.2.2. Velocity Dispersion

The second-moment maps presented in Figure 4 show that the detected extended Lyα halos have average flux-weighted velocity dispersions ($\langle \sigma_{Ly\alpha} \rangle$) spanning from $\langle \sigma_{Ly\alpha} \rangle \sim 30$ to $460\,km\,s^{-1}$ with an average of $320 \pm 120\,km\,s^{-1}$. Note that these values have been corrected for the limited spectral resolution of MUSE according to: $(\sigma_{Ly\alpha}^{corr.})^2 = (\sigma_{Ly\alpha}^{meas.})^2 - (\sigma_{Res.}^\lambda)^2$, where $\sigma_{Res.}^\lambda \sim 35\,km\,s^{-1}$ at the wavelengths explored in our sample. The relatively quiescent $\langle \sigma_{Ly\alpha} \rangle$ values are consistent with measurements reported by Borisova et al. (2016), Arrigoni Battaia et al. (2019a), and Cai et al. (2019) around bright $z \sim 2$–4 quasars.

At $z \sim 3.7$ Borisova et al. (2016) reported a larger velocity dispersion ($\langle \sigma_{ly\alpha} \rangle > 400\,km\,s^{-1}$) for a halo around a radio-loud quasar than for halos around radio-quiet quasars. In the REQUIEM sample, there is one radio-loud quasar, J2228 +0110. It shows a flux-weighted velocity dispersion of $(350 \pm 90)\,km\,s^{-1}$, in agreement with the rest of our (radio-quiet) sample. This dispersion is consistent with Arrigoni Battaia et al. (2019a), who derived similar kinematics for nebulae around radio-loud and radio-quiet quasars at $z \sim 3.2$.[17]

Ginolfi et al. (2018) suggested that the high velocity dispersions observed for the Lyα extended emission around the broad absorption line quasar J1605−0112 at $z = 4.9$ could be linked to an outflow of material escaping the central black hole. Our sample contains only one broad absorption line quasar (J2216−0016) that is 2.9 mag fainter than J1605−0112. For this object, we do not detect the presence of any significant extended emission. Given the generally quiescent motion of the nebulae in our sample, it is unlikely we are probing fast outflows driven by the quasar, which are expected to be on the order of $\gtrsim 1000\,km\,s^{-1}$ (e.g., Tremonti et al. 2007; Villar-Martín 2007; Greene et al. 2012). Nonetheless, we cannot exclude this scenario for the halos associated with the quasars P065−26 and P340−18, where the observed gas velocities are on the order of FWHM $\gtrsim 1500\,km\,s^{-1}$. Simulations of luminous ($> few \times 10^{46}\,erg\,s^{-1}$) quasars indeed predict AGN-driven winds with such large velocities, but these could happen at different scales, ranging from less than 1 kpc to several tens (e.g., Costa et al. 2015; Bieri et al. 2017). However, given the current spatial resolution of our data, we are not sensitive to the presence of extreme kinematics on scales $\lesssim 5$ kpc (where the such an emission would be diluted by the flux of the central AGN).

Is the gas gravitationally bound to the halo? Recent observations (both in absorption and in emission) of the gas in the CGM of quasars have revealed velocity dispersions consistent with the gravitational motion within dark matter halos with masses $M_{DM} \gtrsim 10^{12.5}\,M_\odot$ (e.g., Prochaska & Hennawi 2009; Lau et al. 2018; Arrigoni Battaia et al. 2019a). These are typical masses of halos hosting quasars, derived from strong quasar–quasar and quasar–galaxy clustering observed out to $z \sim 4$ (e.g., Shen et al. 2007; White et al. 2012; Eftekharzadeh et al. 2015; García-Vergara et al. 2017; He et al. 2018;

---

[17] It is worth noting that the radio-loud quasars in both our and the Arrigoni Battaia et al. samples are a few magnitudes fainter than the one sampled by Borisova et al. (2016).

Timlin et al. 2018). At $z \sim 6$, however, such a direct measurement still eludes us. Nevertheless, we can gain some insight by comparing the number density of bright quasars and massive dark matter halos (e.g., Shankar et al. 2010), under the assumption that there is a correlation between the luminosity (mass) of a quasar and the mass of the dark matter halo it is embedded in (see, e.g., Volonteri et al. 2011). By integrating the Kashikawa et al. (2015) luminosity function at $z = 6.3$ (i.e., the average redshift of our survey), we can expect a number density of $\phi(M_{1450} < -25.25) = 2.5 \times 10^{-9}$ Mpc^{-3} for quasars brighter than $M_{1450} = -25.25$ mag.[18] If we assume a high duty cycle of $f_{\mathrm{duty}} = 0.9$, as predicted by Shankar et al. (2010), we can infer that the integral of the halo mass function from Behroozi et al. (2013) matches the integral of the luminosity function for masses $M_{\mathrm{DM}} \sim 10^{12.8} M_{\odot}$.

We can now compare this value to the masses derived from the velocity dispersions observed in the detected halos. Indeed, if we assume an NFW (Navarro et al. 1997) density profile and the concentration-mass relation presented in Dutton & Macciò (2014),[19] the 1D rms velocity dispersion ($\sigma_{\mathrm{1D}}^{\mathrm{rms}}$) can be directly related with the maximum circular velocity ($V_{\mathrm{circ}}^{\mathrm{Max}}$) as: $\sigma_{\mathrm{1D}} = V_{\mathrm{circ}}^{\mathrm{Max}}/\sqrt{2}$ (Tormen et al. 1997). The average $\sigma_{\mathrm{1D}}^{\mathrm{rms}}$ in the REQUIEM sample is $\langle \sigma_{\mathrm{1D}}^{\mathrm{rms}} \rangle = (340 \pm 125)$ km s^{-1}, consistent with the gravitational motion in a $M_{\mathrm{DM}} \sim 10^{12.5} M_{\odot}$ halo at $z = 6$ (see Figure 8). Although most of the detected nebulae are associated with quasars confined to a narrow luminosity range (i.e., between $M_{1450} \sim -26$ mag and -27.5 mag), no clear dependency between the velocity dispersion of the nebulae and M_{1450} is observed (see Figure 8). This suggests that the mechanisms responsible for the broadening of the Lyα line do not depend on the rest-frame UV emission of the central supermassive black hole.
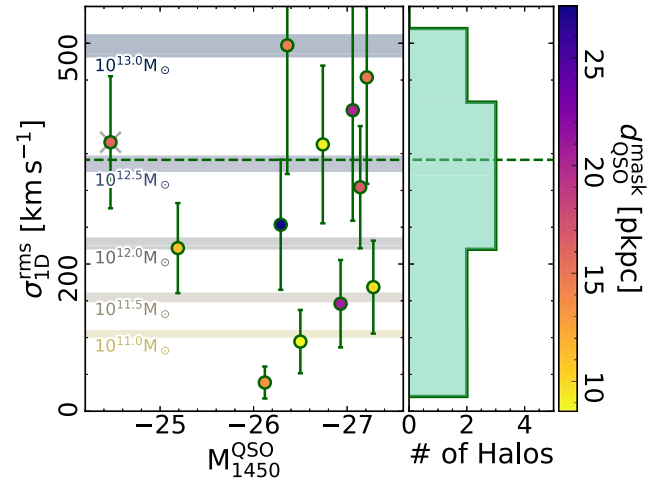
5.3. The Powering Mechanism(s) of the Extended Halos

The currently favored mechanism to explain the extended emission observed around quasars is Lyα fluorescence, i.e., the recombination emission following photoionization of cool ($T \sim 10^4$ K) gas by the strong quasar radiation field (e.g., Hennawi & Prochaska 2013; Arrigoni Battaia et al. 2016, 2019a; Cantalupo 2017). In general, if we assume that quasars are surrounded by a population of cool spherical gas clouds, we can directly infer the surface brightness of the fluorescence emission in two limiting regimes:

(i) The gas in the clouds is optically thick (i.e., with $N_{\mathrm{H\,I}} \gg 10^{17.2}$ cm^{-2}). In this case, it is able to self-shield from the quasar's radiation and the Lyα emission originates from a thin, highly ionized envelope around each individual cloud.

(ii) The gas is optically thin (i.e., with $N_{\mathrm{H\,I}} \ll 10^{17.2}$ cm^{-2}) and is maintained in a highly ionized state by the quasar radiation. In this case, the Lyα emission originates from the entire volume of each cloud.

Figure 8. One-dimensional root-mean-square velocity dispersion measured in each detected nebulosity ($\sigma_{\mathrm{1D}}^{\mathrm{rms}}$) vs. the monochromatic luminosity of the quasars (M_{1450}^{QSO}). Points are color-coded by the size of the recovered halo ($d_{\mathrm{QSO}}^{\mathrm{mask}}$). Horizontal bands are velocity dispersions expected for NFW dark matter halos with masses ranging from 10^{11} to $10^{13} M_{\odot}$. Lower and upper limits of each band correspond to estimates at $z = 5.9$ and $z = 6.6$, respectively. Despite the large scatter, the average velocity dispersion of the nebulae (plotted as a green dashed line) is consistent with values expected in a $z \sim 6$ dark matter halo of $M_{\mathrm{DM}} \sim 10^{12.5} M_{\odot}$.

In the following, we will exploit the formalism presented in Hennawi & Prochaska (2013) to gain insight into the physical status of the gas surrounding the first quasars.

5.3.1. Optically Thick Scenario

If the gas is optically thick, the Lyα surface brightness of the extended emission is expected to be proportional to the flux of ionizing photons coming from the central AGN (Φ) to the covering fraction of optically thick clouds ($f_{\mathrm{C}}^{\mathrm{thick}}$), and to the fraction of incident photons converted into Lyα by the cloud's envelope (η_{thick}) (see also Hennawi et al. 2015; Cantalupo 2017; Farina et al. 2017):

$$\mathrm{SB}_{Ly\alpha}^{\mathrm{thick}} = \frac{\eta_{\mathrm{thick}} h \nu_{\mathrm{Ly\alpha}}}{4\pi(1+z)^4} f_{\mathrm{C}}^{\mathrm{thick}} \Phi\left(\frac{R}{\sqrt{3}}\right), \quad (5)$$

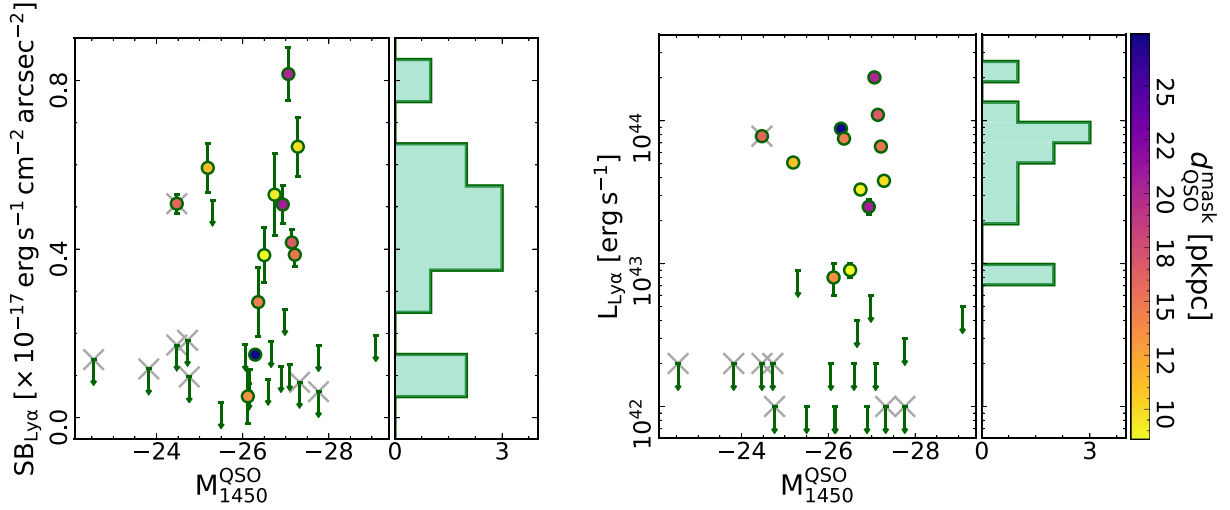where we considered the cool gas clouds to be uniformly spatially distributed in a spherical halo of radius R. Here, Φ can be expressed as a function of the luminosity of the quasar as:

$$\Phi(r) = \int_{\nu_{\mathrm{LL}}}^{\infty} \frac{F_{\nu}}{h\nu} d\nu = \frac{L_{\nu_{\mathrm{LL}}}}{4\pi r^2} \int_{\nu_{\mathrm{LL}}}^{\infty} \frac{1}{h\nu}\left(\frac{\nu}{\nu_{\mathrm{LL}}}\right)^{\alpha_{\mathrm{UV}}} d\nu, \quad (6)$$

where we considered that, blueward of the Lyman limit (ν_{LL}) the quasar spectral energy distribution has the form $L_{\nu} = L_{\nu_{\mathrm{LL}}}(\nu/\nu_{\mathrm{LL}})^{\alpha_{\mathrm{UV}}}$ with $\alpha_{\mathrm{UV}} = -1.7$. The luminosity at the Lyman edge ($L_{\nu_{\mathrm{LL}}}$) can be directly derived from M_{1450} as: $M_{912} = M_{1450} + 0.33$ (see Lusso et al. 2015). Considering $\eta_{\mathrm{thick}} = 0.66$, we can thus write:

$$\frac{\mathrm{SB}_{Ly\alpha}^{\mathrm{thick}}}{10^{-17} \, \mathrm{erg \, s^{-1} \, cm^{-2} \, arcsec^{-2}}} = 21.0\left(\frac{1+z}{1+6.2}\right)^{-4}$$
$$\times \left(\frac{f_{\mathrm{C}}^{\mathrm{thick}}}{0.5}\right)\left(\frac{R}{20 \, \mathrm{pkpc}}\right)^{-2}\left(\frac{L_{\nu_{\mathrm{LL}}}}{10^{31} \, \mathrm{erg \, s^{-1} \, Hz^{-1}}}\right). \quad (7)$$

---

[18] Note that, at these redshifts, the quasar luminosity function is not well-constrained. For instance, using the luminosity function inferred from a sample of 52 SDSS quasars from Jiang et al. (2016), the number density of $z = 6.3$ quasars is $\phi(M_{1450} < -25.25) = 2.6 \times 10^{-10}$ Mpc^{-3}.

[19] The Planck cosmology (Planck Collaboration et al. 2014) used in Dutton & Macciò (2014) is different from the one considered in this paper. However, the effects of this discrepancy are negligible in the context of our calculations.

Figure 9. Left panel: average surface brightness vs. M_{1450}. The 3σ upper limits for nondetected nebulae are shown as downward arrows. Colormap of the points is the same as in Figure 6. For consistency with Section 4.2, here the average $SB_{Ly\alpha}$ is calculated using a circular aperture of radius d_{QSO}^{mask} (or 20 pkpc if the halo was not detected) on pseudo-narrowband images obtained collapsing the datacube between ± 500 km s^{-1} relative to the quasar's systemic redshift. Targets not part of our *core sample* are marked with gray crosses (see Section 2). Right panel: same as the left panel, but with the total Lyα luminosity of the extended halo as the y-axis.

Considering that our *core sample* has an average luminosity at the Lyman edge of $\langle L_{\nu_{LL}} \rangle = 2 \times 10^{31}$ erg s^{-1} Hz, the optically thick scenario predicts a surface brightness of $SB_{Ly\alpha}^{thick} \sim 40 \times 10^{-17}$ erg s^{-1} cm^{-2} arcsec^{-2}, i.e., $\gtrsim 2$ orders of magnitude higher than observed (see Figure 9). Despite the presence of unknowns such as the geometry of the quasar emission or the covering fraction of optically thick clouds, which may be on the order of 60% within a projected distance of 200 pkpc from $z \sim 2$–3 quasars (e.g., Prochaska et al. 2013a), this discrepancy points to a different scenario for the origin of the extended Lyα emission. The optically thick regime is also disfavored by the absence of a clear correlation between $SB_{Ly\alpha}$ and $L_{\nu_{LL}}$ (and thus M_{1450}) as expected from Equation (7) (see Figure 9).

5.3.2. Optically Thin Scenario

If the quasar radiation is sufficiently intense to keep the gas highly ionized (i.e., if the neutral fraction $x_{HI} = n_{HI}/n_H \ll 1$), the expected average surface brightness arising from these optically thin clouds is independent of the quasar luminosity and can be expressed as:

$$\frac{SB_{Ly\alpha}^{thin}}{10^{-19} \text{ erg s}^{-1} \text{ cm}^{-2} \text{ arcsec}^{-2}} = 3.6\left(\frac{1+z}{1+6.2}\right)^{-4}$$
$$\times \left(\frac{f_C^{thin}}{0.5}\right)\left(\frac{n_H}{1 \text{ cm}^{-3}}\right)\left(\frac{N_H}{10^{20.5} \text{ cm}^{-2}}\right), \quad (8)$$

where f_C^{thin} is the covering fraction of optically thin clouds, and n_H and N_H are the cloud's hydrogen volume and column densities, respectively. For further details, see Gould & Weinberg (1996), Osterbrock & Ferland (2006), and Hennawi & Prochaska (2013). Assuming photoionization equilibrium allows us to express the neutral column density averaged over

the area of the halo ($\langle N_{HI} \rangle$) in terms of $L_{\nu_{LL}}$ and $L_{Ly\alpha}$:

$$\frac{\langle N_{HI} \rangle}{10^{17.2} \text{ cm}^{-2}} = 0.1\left(\frac{L_{Ly\alpha}}{10^{44} \text{ erg s}^{-1}}\right)$$
$$\times \left(\frac{L_{\nu_{LL}}}{10^{31} \text{ erg s}^{-1} \text{ Hz}^{-1}}\right)^{-1}. \quad (9)$$

Given the observed luminosities of the nebulae in our core sample ($L_{Ly\alpha} \lesssim 10^{44}$ erg s^{-1}; see Table 3) we obtain $\langle N_{HI} \rangle \ll 10^{17.2}$ cm^{-2}, consistent with the optically thin regime. However, we stress that $\langle N_{HI} \rangle$ is obtained by averaging over the whole area of the halo. So, while $\langle N_{HI} \rangle \gg 10^{17.2}$ cm^{-2} definitively determines the clouds to be optically thick, a small value of $\langle N_{HI} \rangle$ does not provide the same clear result, since individual clouds may still be optically thick while being surrounded by a thinner medium.

Under the assumption that the clouds are optically thin, it is of interest to use Equation (8) to derive constraints on the gas volume density (n_H). Studies of absorption systems associated with gas surrounding $z \sim 2$ quasars suggest that N_H is almost constant within an impact parameter 200 pkpc at a median value of $N_H = 10^{20.5}$ cm^{-2} (e.g., Lau et al. 2016). If $z \sim 6$ quasars are embedded in halos with similar hydrogen column densities, our observations imply $n_H > 1$ cm^{-3}. Intriguingly, similarly high gas densities have been invoked to explain the Lyα emission in giant nebulae discovered around $z \sim 2$–3 quasars (Cantalupo et al. 2014; Arrigoni Battaia et al. 2015a, 2018b; Hennawi et al. 2015; Cai et al. 2018).

5.3.3. Other Possibilities

In addition, other mechanisms have been proposed to explain the presence of extended Lyα nebulae, including gravitational cooling radiation (e.g., Haiman et al. 2000; Fardal et al. 2001; Furlanetto et al. 2005; Dijkstra & Loeb 2009), shocks powered by outflows (e.g., Taniguchi & Shioya 2000; Mori et al. 2004), or resonant scattering of Lyα photons (e.g., Gould & Weinberg 1996; Dijkstra & Loeb 2008).

However, Lyα emission coefficients for collisional excitation are exponentially dependent on the temperature (Osterbrock & Ferland 2006). The concurrence of a very narrow density and temperature range for all the gas in every observed Lyα nebula would thus be necessary to validate this. Instead, recombination radiation has a much weaker dependence on temperature (Osterbrock & Ferland 2006), providing a more natural explanation for the Lyα extended emission in the presence of a strong ionizing flux (e.g., Borisova et al. 2016). In addition, the relatively quiescent motion of the gas in the detected halos (see Section 5.2) is not easily reconciled with shock-powered emission (see also discussion in Arrigoni Battaia et al. 2019a).

On the other hand, resonant scattering of Lyα photons from the central AGNs and from young stars in the host galaxies can provide a relevant contribution to the emission, if the gas is optically thick at the Lyα transition ($N_{H\,I} \gtrsim 10^{14}\,cm^{-2}$). This was proposed as the main process powering the extended Lyα emission detected around $3 \lesssim z \lesssim 6$ Lyα emitters by Wisotzki et al. (2016). Hennawi & Prochaska (2013) showed that the surface brightness of extended Lyα emission produced via resonant scattering by neutral gas in the CGM ($SB_{Ly\alpha}^{scatt.}$) is expected to be directly proportional to the flux of ionizing photons emitted close to the Lyα resonance ($L_{\nu L y\alpha}$). Given that the peak of the Lyα line of $z \sim 6$ quasars is typically absorbed by neutral hydrogen, there is no direct way to test for the presence of such a correlation in the REQUIEM survey. In any case, Arrigoni Battaia et al. (2019a) reported the lack of significant correlation between the surface brightness of Lyα halos and the luminosity of the peak of the Lyα line of $z \sim 3$ quasars. In addition, we do not detect clear signals of the characteristic double-peaked profiles expected for resonantly trapped Lyα photons (e.g., Dijkstra 2017). However, to properly test this scenario, a detailed analysis of the Lyα line shape must be performed on spectra with high S/N and high spectral resolution.

We stress that all the aforementioned mechanisms can be in place at the same time and contribute at different levels to the observed emission. Additional factors can also modulate the total luminosity of the halos. For instance, the presence of dust on scales larger than 20 kpc (e.g., Ménard et al. 2010; Roussel et al. 2010) can destroy Lyα photons, and/or the variability of the quasar emission (e.g., MacLeod et al. 2012; Yang et al. 2019c) can be faster than the response of the halo (with a strong dependence on n_H) and wash out some of the expected correlations. Future observations of nonresonant lines such as He II or Hα will be instrumental in disentangling different emission mechanisms (e.g., Arrigoni Battaia et al. 2015a; Leibler et al. 2018; Cantalupo et al. 2019). This is particularly challenging at $z > 6$, where only space-based observations will have the sensitivity necessary to provide additional information about the gas surrounding the first quasars.

5.4. Lyα Nebulae and Galaxy Overdensities

Several giant Lyα nebulae extending to scales ≫100 kpc have recently been reported in the literature (Cantalupo et al. 2014; Hennawi et al. 2015; Arrigoni Battaia et al. 2018b, 2019b; Cai et al. 2018; Lusso et al. 2019). The incidence of such large nebulae has been estimated to be on the order of few percent at $z \sim 2$–3 (Hennawi & Prochaska 2013; Arrigoni Battaia et al. 2016, 2019a). A larger sample of $z \gtrsim 6$ quasars is necessary to assess if this low occurrence holds at high redshifts. In any case, all $z < 4$ giant nebulae appear to be

invariably associated with overdensities of AGN and galaxies, suggesting a connection between protocluster structures and extremely extended emission: see, e.g., Hennawi et al. (2015) and Arrigoni Battaia et al. (2018a), but cf. Bădescu et al. (2017) for examples of large Lyα blobs located at the outskirts of high-density regions.

We can qualitatively test this scenario at $z > 6$, by searching for peculiarities in the nebulae associated with quasars for which deep ALMA observations have revealed the presence of bright [C II] 158 μm companions (i.e., J0305−3150, P231−20, P308−21, and J2100−1715; see Section 2 and Decarli et al. 2017; Willott et al. 2017; Venemans et al. 2019).[20] J2100 −1715 has a [C II] 158 μm companion located at a separation of ∼60 kpc (Decarli et al. 2017; Neeleman et al. 2019), but does not show the presence of any significant extended Lyα emission. J0305−3150, although located in an overdensity with three [C II] 158 μm and one LAE emitter (Farina et al. 2017; Venemans et al. 2019), shows a very faint halo. Finally, P231−20 and P308−21 host halos that are among the brightest and most extended in the REQUIEM survey, and both are in the middle of gravitational interactions with their companions (Decarli et al. 2019a; Neeleman et al. 2019).

The variety of the Lyα emission observed in this (small) sample of quasars with companions suggests that, at $z > 6$, bright and extended Lyα halos may be associated with ongoing merger events. If this is the case, P323+12, which exhibits the brightest nebular emission in our sample, is likely to be in a gravitational interaction. Mazzucchelli et al. (2017) presented low-resolution NOEMA observations on the [C II] 158 μm emission line of this source, without detecting a merger. However, testing the merger scenario requires higher sensitivity and better spatial resolution— for example, with ALMA or NOEMA.

5.5. The Average Surface Brightness Profile

In this section, we will infer the average surface brightness profile of the Lyα emission around quasars in the REQUIEM survey, and we will compare its shape with lower-redshift studies. To avoid selection effects, we will focus only on our *core sample*. We remind the reader that this consists of 23 radio-quiet quasars at an average redshift of $\langle z \rangle = 6.27$ and absolute magnitude ranging from $M_{1450} = -25.2$ mag to -29.1 mag, with an average of $\langle M_{1450} \rangle = -27.1$ mag (see Section 2). As a lower-redshift comparison, we will use the following studies (see Figure 10): (i) Cai et al. (2019), who investigated with KCWI 16 quasars at $2.20 < z < 2.38$ (with an average of $\langle z \rangle = 2.27$) and absolute magnitude between $M_{1450} = -29.0$ mag and -26.1 mag (with $\langle M_{1450} \rangle = -27.3$ mag); (ii) *QSO MUSEUM* (Arrigoni Battaia et al. 2019a), a MUSE investigation for extended Lyα emission around a sample of 61 quasars at $3.03 < z < 3.46$ (with $\langle z \rangle = 3.21$) with absolute magnitudes in the range -28.3 mag $< M_{1450} < -25.6$ mag (with $\langle M_{1450} \rangle = -27.2$ mag); and (iii) Borisova et al. (2016), who explored with MUSE the vicinity of 19 bright (-29.0 mag $< M1450 < -26.8$ mag, and $\langle M_{1450} \rangle = -28.0$ mag) quasars at $3.02 < z < 3.91$ (with $\langle z \rangle = 3.36$).[21]

The extended nebulae detected in the REQUIEM survey appear to have complex morphologies and clear asymmetries

---

[20] We note that MUSE observations for all these quasars have been gathered with integration times >3× longer than the median of our sample (see Table 1).
[21] The average surface brightness profile for the Borisova et al. sample is presented in Marino et al. (2019).
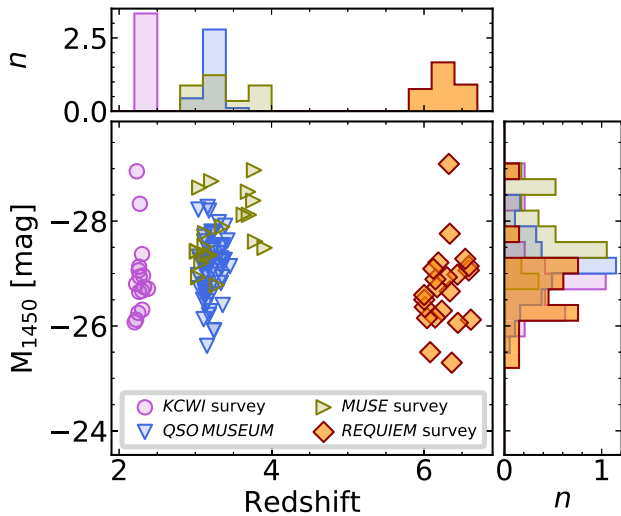
Figure 10. Redshift vs. M_{1450} distribution of the quasars part of the surveys from: Cai et al. (2019), consisting of 16 quasars, shown as magenta circles and histograms; Arrigoni Battaia et al. (2019a), consisting of 61 quasars, shown as light blue downward-pointing triangles and histograms; and Borisova et al. (2016), shown as green rightward-pointing triangles and histograms. The 23 quasars part of our *core sample* are shown as orange diamonds and histograms. Histograms are normalized by the total number of targets and by the bin size (with steps 0.3 in redshift and of 0.3 mag in absolute magnitude). The average absolute magnitudes of the Cai et al. sample, the Arrigoni Battaia et al. sample, and our *core* sample are nearly identical, while the quasars studies in Borisova et al. are, on average, ∼0.7 mag brighter.

(see Figure 2). We proceeded following the standard approach in the literature, and we obtained the surface brightness profiles averaging over circular apertures centered on the location of the quasars. As explained in Section 4.2, single profiles were extracted from pseudo-narrowband images created by collapsing the data cubes over 30 Å centered at the location of the Lyα line, redshifted to the quasar's systemic redshift. To create the stacked profile, we first correct these profiles for cosmological dimming (i.e., by a factor $(1 + z)^4$) and then we average over them with equal weights. This prevents the introduction of biases toward deeper exposures and/or brighter objects (the marginal variations caused by the use of the median to combine the different radial profiles are discussed in Appendix D). We also create the stacked profile only using the subsample of quasars for which an extended emission has been detected with significance. The results of this procedure are plotted in Figure 11, where the average surface brightness profile obtained for all quasars is depicted by orange triangles and the one from quasars embedded in halos by purple circles (the average radial profile for the entire *core sample* is tabulated in Table 4 in Appendix D). For comparison, the average profiles from Arrigoni Battaia et al. (2019a), Cai et al. (2019), and Marino et al. (2019) are displayed as magenta, light blue, and olive solid lines, respectively.

In order to extract information from the stacked profiles, we perform a fit with an exponential function: $(1 + z)^4 \, \mathrm{SB}_{\mathrm{Ly}\alpha}(r) = C \exp(-r/r_h)$, where C is the normalization and r_h is the scale length of the profile. The resulting parameters are $C = (3.0 \pm 0.4) \times 10^{-14}$ erg s^{-1} cm^{-2} arcsec^{-2} and $r_h = (9.4 \pm 0.8)$ kpc for the full sample and $C = (5.6 \pm 0.8) \times 10^{-14}$ erg s^{-1} cm^{-2} arcsec^{-2} and $r_h = (6.4 \pm 0.3)$ kpc for the stack quasars with detected halos. As expected, while the two profile match within the errors, the latter appears slightly more

concentrated due to the stronger signal in the central ∼20 kpc. In the following, we will keep showing both profiles. In the discussion, however, we will focus solely on the one that includes all quasars, as it is more representative of the full high-z quasar population.

The scale length derived for $z \sim 6.2$ quasars is a factor of ∼2× smaller than the $r_h = (15.5 \pm 0.5)$ pkpc and $r_h = (21.1 \pm 0.9)$ pkpc measured for radio-quiet quasars at $z \sim 3.2$ (Arrigoni Battaia et al. 2019a) and at $z \sim 2.3$ (Cai et al. 2019), suggesting that extended halos are more compact at higher redshift. For comparison, the sample of Lyα emitters in the *Hubble* Ultra Deep Field shows a much milder evolution of halo scale length, increasing from $r_h = (3.8 \pm 1.3)$ pkpc at $5 < z \lesssim 6$ to $r_h = (4.4 \pm 1.5)$ pkpc at $3 \lesssim z < 4$ (Leclercq et al. 2017). However, we should note that, given the difference in apparent brightness of the quasars, the cosmological evolution of the angular diameter distance, and the factor ∼8× difference in sensitivity due to redshift dimming, our observations are more sensitive to regions closer to the quasar while Cai et al. (2019), Arrigoni Battaia et al. (2019a), and Borisova et al. (2016) are more sensitive to extended emission at larger scales.

Arrigoni Battaia et al. (2019a) reported a strong evolution of the average properties of the extended emission with cosmic time. This was based on the comparison of the average surface brightness radial profiles of their quasars split into a $z \sim 3.3$ and a $z \sim 3.1$ subsamples and the results obtained from a narrowband survey of bright radio-quiet quasars at $z \sim 2.2$ (Arrigoni Battaia et al. 2016). Recently, Cai et al. (2019) showed that studies based on narrowband imaging underestimated the total nebular emission by an order of magnitude (see also discussion in Borisova et al. 2016). The new IFU observations revealed a less pronounced evolution, with halos surrounding quasars at $z \sim 2$ being ∼0.4 dex fainter than at $z \sim 3$ (Cai et al. 2019). In the following, we will test if this trend holds out to the redshifts provided by the REQUIEM survey.

In the optically thin scenario, the Lyα surface brightness scales as $\mathrm{SB}_{\mathrm{Ly}\alpha} \propto n_H N_H$ (see Equation (8)). If the gas clouds are bound to the dark matter halo hosting the quasar (see Section 5.2), it can be shown that $N_H \propto n_H R_{\mathrm{vir}}$, where R_{vir} is the virial radius; for a similar argument applied to Mg II absorbers in the CGM of $z \sim 1$ galaxies, see Churchill et al. (2013b). Furthermore, given the inferred high densities ($n_H > 1 \, \mathrm{cm}^{-3}$), the emitting gas is not likely to trace the evolution of the cosmic mean density. We thus expect the size of the nebular emission to scale with the growth of R_{vir} with cosmic times. For the sake of simplicity, we will consider that quasars are hosted by massive halos with $M_{\mathrm{DM}} = 10^{12.5} \, M_\odot$ independent of their redshift (see, e.g., discussion in Shen et al. 2007; He et al. 2018). Thus, the virial radius $R_{\mathrm{vir}}(z) = [3M_{\mathrm{DM}}/4\pi\rho_c(z)]^{\frac{1}{3}}$ depends only on the critical density of the universe at a determined redshift [$\rho_c(z)$]. For the considered halo, the virial radius calculated at $z = 6.28$ increases by a factor ∼1.6× down to $z = 3.36$, and by a factor ∼2.2× down to $z = 2.27$.

In Figure 12, we show the average surface brightness profiles at $z = 6.28, 3.36, 3.34, 3.11$, and 2.27, normalized by the virial radius. At all the these redshifts, the emitting gas appears to be located well within R_{vir} and the average profile becomes brighter at higher redshifts (with the $z \sim 3$ and $z \sim 6$
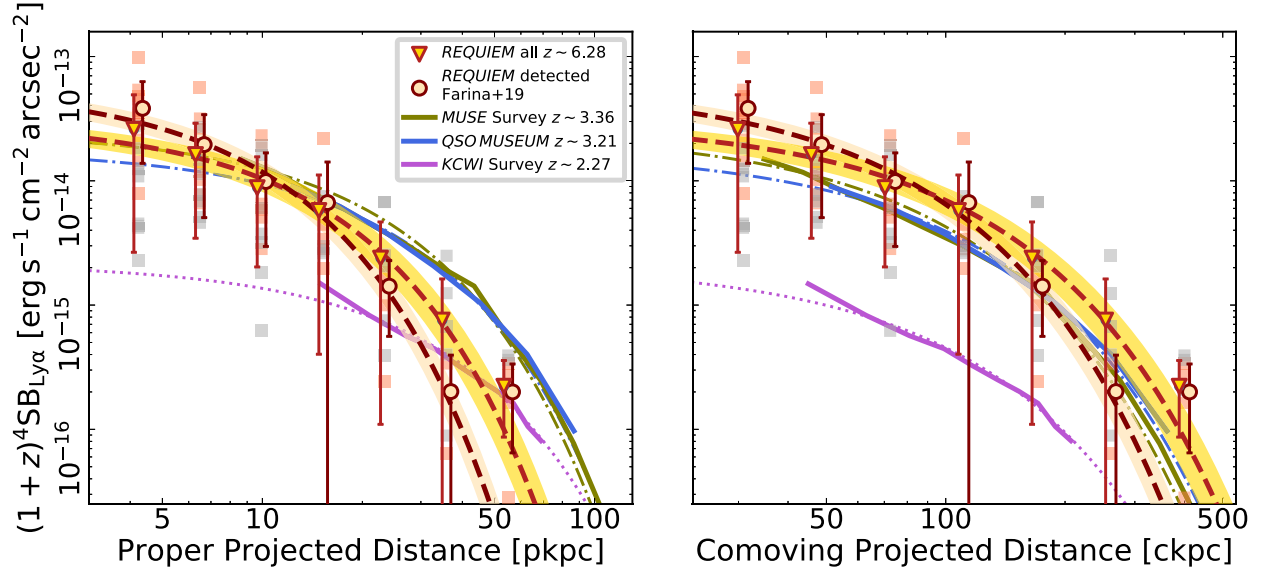
Figure 11. Left panel: average Lyα surface brightness profile of the *core sample* of our REQUIEM survey. We show the individual circularly averaged profiles extracted around each quasar as orange squares for detected halos and gray squares for nondetections. Sum-averaged profiles considering all quasars (orange triangles) or only significantly detected halos (purple circles) are also shown, together with their respective best exponential fits (orange and purple dashed lines; shaded regions provide 1σ uncertainties in the fit). Data points have been slightly shifted along the *x*-axis, for the sake of clarity. The average surface brightness profiles of the extended emission around quasars at $z \sim 2.27$ (magenta line; Cai et al. 2019), $z \sim 3.21$ (light blue line; Arrigoni Battaia et al. 2019a), and $z \sim 3.36$ (olive green line; Marino et al. 2019) are also plotted. The corresponding exponential best fits are shown in the same color palette. Note that all measurements are corrected for the $(1 + z)^4$ factor to compensate for cosmological dimming. Right panel: same as left panel, but in comoving units.

Table 4
Average and Median Lyα Surface Brightness Profile Around Quasars in the
Core Sample of the REQUIEM Survey

Radius (pkpc)	Average Lyα SB	rms	Median Lyα SB	25th Percentile	75th Percentile
			$(10^{-16}$ erg s^{-1} cm^{-2} arcsec^{-2})		
4.2	259.2	232.7	198.7	101.3	345.7
6.5	162.7	128.2	120.8	77.9	175.5
9.9	88.1	67.9	60.5	37.6	106.7
15.3	57.7	53.7	39.2	28.0	65.5
23.4	23.9	22.8	18.5	8.8	25.3
35.9	7.6	8.7	4.0	2.1	9.6
55.0	2.2	1.4	2.1	1.6	3.4

Note. All measurements are corrected for cosmological surface brightness dimming.

profiles being consistent within the scatter). If we model the profiles normalized by the virial radius via an exponential function, $(1 + z)^4 \, \mathrm{SB}_{\mathrm{Ly\alpha}}(r) = C_h \exp(-x/x_h)$, with C_h and x_h as free parameters and $x = r/R_{\mathrm{vir}}$, we obtain: $C_h = (3.0 \pm 0.4) \times 10^{-14}$ erg s^{-1} cm^{-2} arcsec^{-2} and $x_h = (0.15 \pm 0.01)$ for the full quasar sample, and $C_h = (5.6 \pm 0.8) \times 10^{-14}$ erg s^{-1} cm^{-2} arcsec^{-2} and $x_h = (0.13 \pm 0.01)$ kpc for the subsample of detected halos. The value of x_h measured at $z \sim 6.28$ matches the $x_h = 0.14$, 0.16, 0.15, and 0.16 estimated for quasars at $z \sim 3.36$, $z \sim 3.34$, $z \sim 3.11$, and $z \sim 2.27$ respectively. This suggests a scenario where the (average properties of the) extended Lyα emission mirrors the cosmic evolution of the dark matter halos they reside in (see also Section 5.2). On the other hand, C_h rapidly increases with redshift from $z \sim 2$ to $z \sim 3$, and grows much more gradually between $z \sim 3$ and $z \sim 6$. This behavior is described by the gray dashed line in Figure 12. This is the expected average
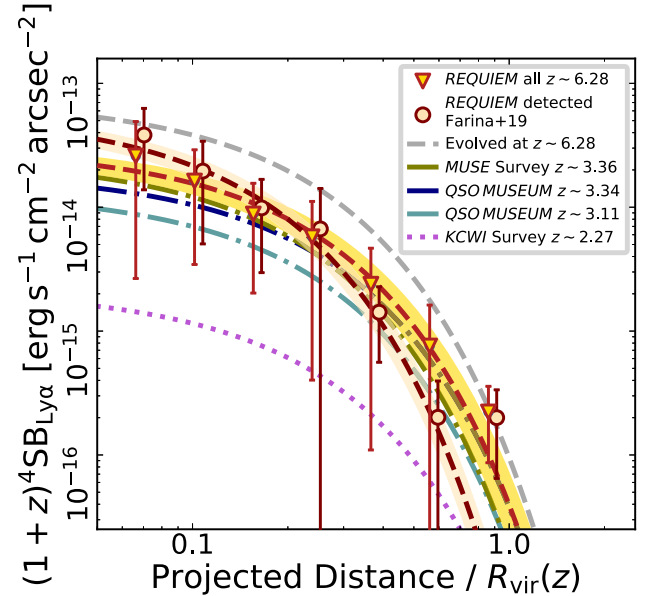
Figure 12. Average, cosmological dimming–corrected, surface brightness profiles of the extended emission around quasars with the radius normalized to the virial radius $R_{\mathrm{vir}}(z)$ of a $10^{12.5}$ $M_{\odot}$ dark matter halo located at different redshifts. Color code of the data points and curves is the same as in Figure 11. In addition, following Arrigoni Battaia et al. (2019a), we split the quasars part of the *QSO MUSEUM* in two subsamples with median redshifts $z = 3.11$ and $z = 3.34$. The corresponding exponential fits of the surface brightness profiles are plotted as light and dark blue dashed–dotted lines, respectively. Gray dashed line shows the profile expected if the evolutionary trend observed between $z = 2.27$ and $z = 3.36$ is extrapolated linearly in redshift to $z = 6.28$.

profile of the extended emission if the increase of the normalization observed between $z \sim 2.27$ and $z \sim 3.36$ were to keep its pace linearly with redshift up to $z \sim 6.28$. The observed profile from the REQUIEM survey lies ~ 0.4 dex below this prediction.

Intriguingly, hydrodynamical cosmological simulations show that high-z galaxies in dark matter halos of $M_{DM} \gtrsim 10^{12} M_\odot$ are mainly fed by cool gas streams (coexisting with a hot, shocked medium) down to redshift $z \sim 2$–3. Below this "critical" redshift, these cool streams are not able to balance the virial shock heating and are suppressed (e.g., Dekel & Birnboim 2006; Dekel et al. 2009, 2019). This theoretical picture would naturally explain the observed evolution of the surface brightness profile. Under the assumption that the emission arises from optically thin clouds of gas, the surface brightness is expected to scale as: $SB_{Ly\alpha} \propto (1 + z)^4 f_C^{thin} n_H N_H$, where N_H is proportional to the total mass in cool gas M_{cool} (e.g., Hennawi & Prochaska 2013; Arrigoni Battaia et al. 2019a; see also our Section 5.3). Thus, the small variation in Lyα surface brightness reported between $z \sim 6$ and $z \sim 3$ suggests that cool streams are able to replenish the CGM with gas, permitting M_{cool} to keep pace with M_{DM}. The consequent heating of massive halos at $z \lesssim 3$ may be responsible for the drop of cool gas in the CGM and thus of the average Lyα emission. However, this picture clashes with the large amount of cool gas revealed by absorption studies of the CGM around $0.5 \lesssim z \lesssim 2$ quasars (e.g., Bowen et al. 2006; Farina et al. 2013, 2014; Prochaska et al. 2014; Johnson et al. 2015).

5.6. Extended Emission and Quasar Near Zones

Near the end of the cosmic reionization epoch, the large fraction of neutral hydrogen present in the universe suppresses virtually all the emission blueward of the Lyα line (e.g., Gunn & Peterson 1965). However, the intense radiation of a luminous quasar is able to ionize the surrounding gas, creating a bubble of enhanced transmission in the Lyα forest in its immediate vicinity known as the proximity (or near) zone (e.g., Cen & Haiman 2000; Madau & Rees 2000; Haiman & Cen 2001).

The size of the proximity zone (R_p) is traditionally defined as the distance out to which the Lyα transmission, smoothed on a scale of 20 Å, first falls below 10% (Fan et al. 2006). Absorption studies of the first quasars revealed that proximity zones can extend to several proper megaparsecs (Fan et al. 2006; Carilli et al. 2010; Venemans et al. 2015; Eilers et al. 2017), i.e., on scales much larger than the one probed by the extended Lyα emission around quasars (typically $\lesssim 100$ kpc). Proximity zones are thus expected to be more sensitive to the state of the IGM than to the quasar's CGM (e.g., Fan et al. 2006).

The interpretation of the magnitude of R_p depends on the neutral fraction of the surrounding IGM. If the gas is close to fully neutral, the size of the resulting proximity zone will reflect the ionized bubble carved out by the quasar:

$$R_p = \left(\frac{3 \dot{N}_{ion} t_{QSO}}{4 \pi n_H x_{H\,I}} \right)^{\frac{1}{3}}, \qquad (10)$$

where $\dot{N}_{ion}$ is the emission rate of the ionizing photons and t_{QSO} is the age of the quasars. Alternatively, if the gas is already mostly ionized, the proximity zone size instead reflects the distance out to which the ionizing flux from the quasar is enough to keep the Lyα forest sufficiently transparent (Bolton & Haehnelt 2007). The size of the proximity zone can still vary with the age of the quasar if the quasar is sufficiently young, such that the IGM gas has not yet reached photoionization

equilibrium with the newly enhanced ionizing flux (Eilers et al. 2017, 2018; Davies et al. 2019b).

Once the dependence on the quasar luminosity is removed, the typical size for the "corrected" near zone of a $z \sim 6$ quasar is $R_p^{corr} = R_p \times 10^{-0.4(-27.0-M_{1450})/2.35} \sim 5$ pMpc. Deviations below $R_{p,corr} \sim 3$ pMpc should be very rare unless nonequilibrium photoionization is at play (Eilers et al. 2017; Davies et al. 2019b). Thus, the discovery of quasars with exceptionally small proximity zones and no evidence for significantly neutral gas by Eilers et al. (2017) implies that these objects must have been shining for $t_{QSO} \lesssim 10^5$ yr; see Eilers et al. (2018) and Davies et al. (2019b) for further details.

Interestingly, this value is comparable to the light-crossing time, given the size of the nebulae observed in our survey: $t_{cross} = d_{QSO}/c \sim 3 \times 10^4$ yr for $d_{QSO} = 10$ pkpc. This suggests that if a quasar in our sample has a peculiarly small R_p^{corr}, then its extended emission should also be small or nonexistent (see discussion in Eilers et al. 2018). We remind the reader that the recombination timescales as $t_{rec} = 1/n_e \alpha_A$, where the electron density can be calculated as $n_e = n_H(1 + Y/2X)$ (assuming that all helium is doubly ionized) and the case A recombination coefficient evaluated at $T = 10^5$ K is $\alpha_A = 4.2 \times 10^{-13}$ cm^3 s^{-1} (Osterbrock & Ferland 2006). Thus, for the volume densities inferred in Section 5.3, we obtain values of $t_{rec} \lesssim 10^5$ yr. This means that, in the case of intermittent quasar activity, the extended Lyα halo would disappear if the timescale in which the quasar is inactive is $t_{off} > t_{rec}$.

We can test this scenario within our REQUIEM survey. Indeed, our targets overlap with the Eilers et al. (2017) sample in six quasars, two of which have $R_{p,corr} \lesssim 3$ pMpc: J2229+1457 with $R_p^{corr} = (1.07 \pm 0.33)$ pMpc, and J0100+2802 with $R_p^{corr} = (3.09 \pm 0.06)$ pMpc.[22] It is alluring that none of these young quasar candidates show an extended Lyα halo. Deeper MUSE observations complemented with sensitive NIR spectroscopy aimed to confirm the true nature of these small zones (e.g., Eilers et al. 2018) will provide new information on the nature of this class of objects (A.-C. Eilers et al. 2019, in preparation).

5.7. Is the Halo Around P323+12 Lensed?

The procedure to find and remove low-redshift contaminants described in Section 4 revealed the presence of a galaxy located within the bright halo detected in association with the quasar P323+12, i.e., $1\farcs6$ NNE from the quasar at R.A.$_{J2000}$ = 21:32:33.22 and decl.$_{J2000}$ = +12:17:56.8 (see Figure 13). This galaxy is spatially resolved in deep near-infrared imaging collected with LBT/LUCI2+ARGOS (see Section C). The detection of the Ca H&K $\lambda\lambda 3969,3934$ (hereafter Ca HK; see Figure 13) in the galaxy spectrum determined its redshift at $z_{gal} = 0.711 \pm 0.001$. In the following, we check the possibility that this galaxy could act as a lens and thus enhance the total luminosity observed for this halo.

The expected radius of the Einstein ring (θ_E) can be estimated by assuming the potential well of the galaxy is well-described by a singular isothermal sphere (SIS). This allows us to directly relate θ_E to the velocity dispersion of the SIS (σ_{SIS}),

---

[22] The proximity zone sizes are calculated from ESI/Keck II spectra considering the Planck Collaboration et al. (2014) cosmology. The R_p^{corr} values for the remainder quasars part of both the Eilers et al. and the REQUIEM survey samples are: J0210−0456 with $R_p^{corr} = (3.47 \pm 0.34)$ pMpc, J2329−0301 with $R_p^{corr} = (4.86 \pm 0.70)$ pMpc, J1030+0524 with $R_p^{corr} = (5.95 \pm 0.36)$ pMpc, and J2054−0005 with $R_p^{corr} = (4.32 \pm 0.19)$ pMpc.
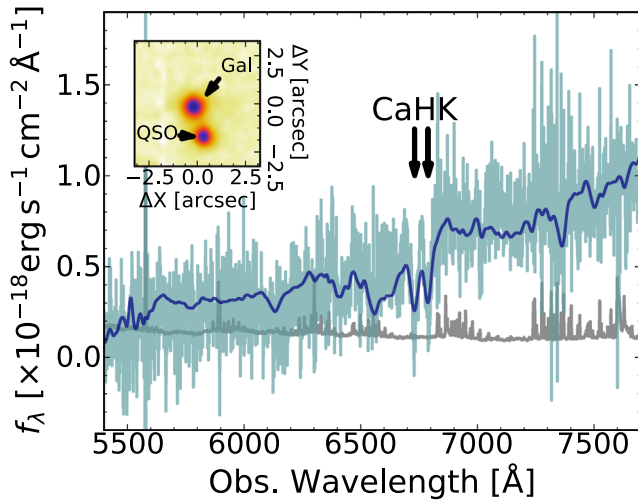
Figure 13. Spectrum of the foreground galaxy located $1''\!57$ north–northeast of the optical position of the quasar P323+12 (light blue). The elliptical galaxy template from Mannucci et al. (2001) redshifted to $z_{\rm gal} = 0.711$ and rescaled to the flux observed in the Pan-STARRS i-band $i_{\rm PS1,gal} = 23.29$ mag is shown as a dark blue line (see Section 5.7 for details). The inset plots the location of the galaxy with respect to the quasar in the pseudo-broadband image obtained by collapsing the MUSE cube between 8200 and 9200 Å.

to the angular diameter distance between the halo and the lens ($D_{\rm LH}$), and to the angular diameter distance between the halo and the observer ($D_{\rm H}$) (e.g., Narayan & Schneider 1990; Peacock 1999; Chieregato et al. 2007):

$$\theta_{\rm E} = 4\pi \left(\frac{\sigma_{\rm SIS}}{c} \right)^2 \frac{D_{\rm LH}}{D_{\rm H}}. \tag{11}$$

Given the relatively low S/N per pixel and spectral resolution (i.e., $R = \lambda/\Delta\lambda \sim 2700$ at ~ 6800 Å) of the spectrum in our data, we assume that $\sigma_{\rm SIS} = \sigma_\star$ (i.e., the velocity dispersion of the galaxy) and we infer $\sigma_\star$ from the Faber–Jackson relation (Faber & Jackson 1976). Using the updated relation from Nigoche-Netro et al. (2010), a galaxy with an r-band absolute magnitude of $M_r = -20.44$ mag has a $\sigma_\star = 100$ km s^{-1}. Plugging these values in Equation (11), we obtain $\theta_{\rm E} \sim 0''\!2$. This is well below the current spatial resolution of our MUSE observations (see Table 1), and thus our measurements are not significantly biased by lensing.

Given the estimated size of the Einstein ring, the new AO system GALACSI on MUSE (Stuik et al. 2006) should be able to resolve it. Future high spatial resolution observations of this system will allow us to investigate the extended halo of a $z \sim 6.6$ quasar in unprecedented detail.

6. Summary and Conclusions

We have conducted a sensitive search for extended Lyα emission around a sample of 31 $5.7 < z < 6.6$ quasars spanning absolute magnitudes from $M_{1450} = -22.5$ mag to $M_{1450} = -29.1$ mag. This ongoing VLT/MUSE effort represents the first statistical study of the CGM of quasars during the epoch of reionization (see Figure 14). After subtracting the contribution of the central AGN, we unveil the presence of significant extended Lyα emission around 12 targets. The detected nebulosities extend out to ~ 30 kpc from the quasars
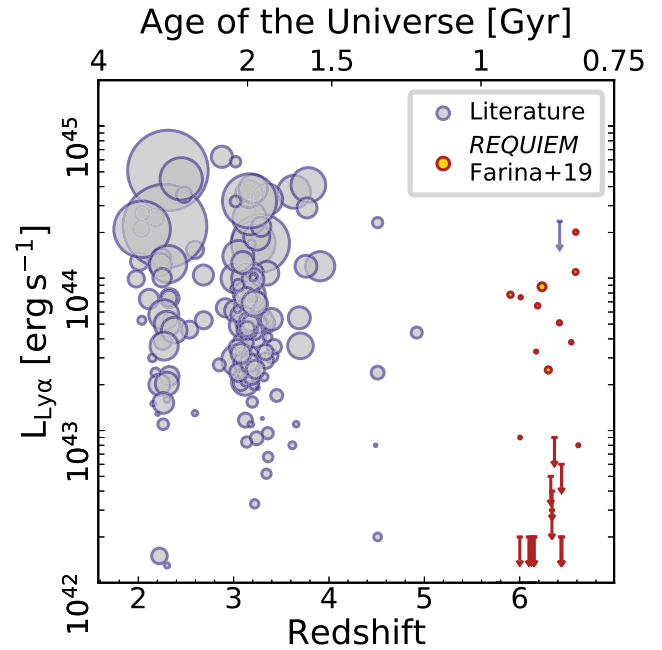
Figure 14. Redshift vs. total luminosity of all extended Lyα nebulae associated with QSOs known to date. Gray and orange points are data from the literature and from the REQUIEM survey, respectively. The size of the point is proportional to the area (in pkpc^2) covered by each halo. Downward-pointing arrows are 3σ upper limits estimated integrating the nominal surface brightness limits over circular apertures with radius 20 pkpc. All values are conformed to the concordance cosmology used in this paper (see Table 5 in Appendix E). However, effects of different sensitivities and observing techniques are not taken into account.

and show a variety of morphologies and physical properties. The study of these systems reveals that:

(i) The redshift of the extended emission aligns well with the systemic redshift of the quasar host galaxies traced by the [C II] 158 μm line, with an average shift of $\langle \Delta V_{\rm sys} \rangle = (69 \pm 36)$ km s^{-1}.

(ii) The luminosities of the halos appear to be independent of the amount of star formation in the host galaxy and of the UV luminosity of the central AGN.

(iii) The velocity dispersion of the gas in the halos is consistent with gravitational motion in dark matter halos of $M_{\rm DM} \lesssim 10^{13}\,M_\odot$ at $z \sim 6$.

(iv) For most of our objects, we do not find clear evidence of rotation or ordered motion. However, the extended emission around the quasar P231+20 shows indications of a rotational pattern.

(v) The surface brightness of the detected halos is consistent with the emission expected from optically thin clouds illuminated by the quasars. However, this requires high volume densities, on the order of $n_{\rm H} \gtrsim 1$ cm^{-3}.

(vi) The average surface brightness profile of the halos is fit well by an exponential curve. After correcting for redshift dimming and scaling distances by the virial radius of a halo of $10^{12.5}\,M_\odot$, we observe no strong evolution of the profile between $z \sim 6$ and $z \sim 3$, followed by a decline in surface brightness down to $z \sim 2$.

(vii) The two quasars that have peculiarly small near zones ($R_{\rm p}^{\rm corr} \lesssim 3$ pMpc) do not show evidence for extended emission. This is consistent with a scenario where these quasars that have been shining for less than $\sim 10^5$ yr.

We can ask ourselves if the reservoirs of cool gas observed around the first quasars are sufficient to sustain the enormous star formation rates of the host galaxies (with depletion time of $t_{\rm dep} \sim 10$–100 Myr) and fast growth of the central supermassive black holes. Little evolution in the characteristics of the extended Lyα halos is observed between $z \sim 6$ and $z \sim 3$, suggesting that the emitting clouds retain similar properties within this redshift range. In this idealized model, and assuming a spherical distribution for the clouds, the total mass in cool gas can be calculated as:

$$M_{\rm cool} = \pi R f_c N_{\rm H} \frac{m_p}{X}. \tag{12}$$

Given that the extended emissions occur on scales of 10–30 pkpc, we can roughly estimate $M_{\rm cool} \gtrsim 10^9\, M_\odot$ around the first quasars. In general, hydrodynamical cosmological simulations are necessary to follow the complex journey of this gas from the IGM down to the host galaxy. However, given the observed kinematics, we can assume that the angular momentum has little impact in the accretion process and consider the freefall time ($t_{\rm ff} = \sqrt{3\pi/32\, G\, \rho} \sim 50$ Myr) as the minimum timescale over which gas inflows. This implies that, potentially, the rate of gas supply (on the order of $\dot{M}_{\rm cool} \sim 10$–$100\, M_\odot\ {\rm yr}^{-1}$) is compatible with the SFR estimated for the quasar host galaxies. Further investigations of the detected nebulae are necessary to fully capture the physical status of the emitting material, but our REQUIEM survey suggests that the halos of the first quasars contain sufficient fuel to maintain the high observed rate of gas consumption.

As the first IFS study aimed at mapping the Lyα emission around a statistical sample of $z > 6$ quasars, the REQUIEM survey demonstrates that direct detection of the CGM of the first massive galaxies is possible in 1–10 hr of VLT/MUSE per target. The detected nebulae are unique targets for future multiband follow-up observations to characterize the distribution of the gas and to constrain its physical conditions. In the near future, we will exploit the rich data set provided by the REQUIEM survey to study the clustering of galaxies around these quasars (Paper II), to search for UV-bright counterparts of high-z absorption selected galaxies (Paper III), and to perform a detailed comparison between the dynamics of the host galaxies and the properties of the extended emission (Paper IV).

Appendix A
Atlas of the Quasars Part of the REQUIEM Survey

In Figure 15, we show the RGB postage stamps of the quasar vicinity created by combining three 2000 km s^{-1} wide pseudo-narrowband images: one located 16,000 km s^{-1} blueward, one 5000 km s^{-1} redward, and one at the redshifted Lyα wavelength. The spectra of the quasars extracted over apertures with a radius two times larger than the seeing are also shown.
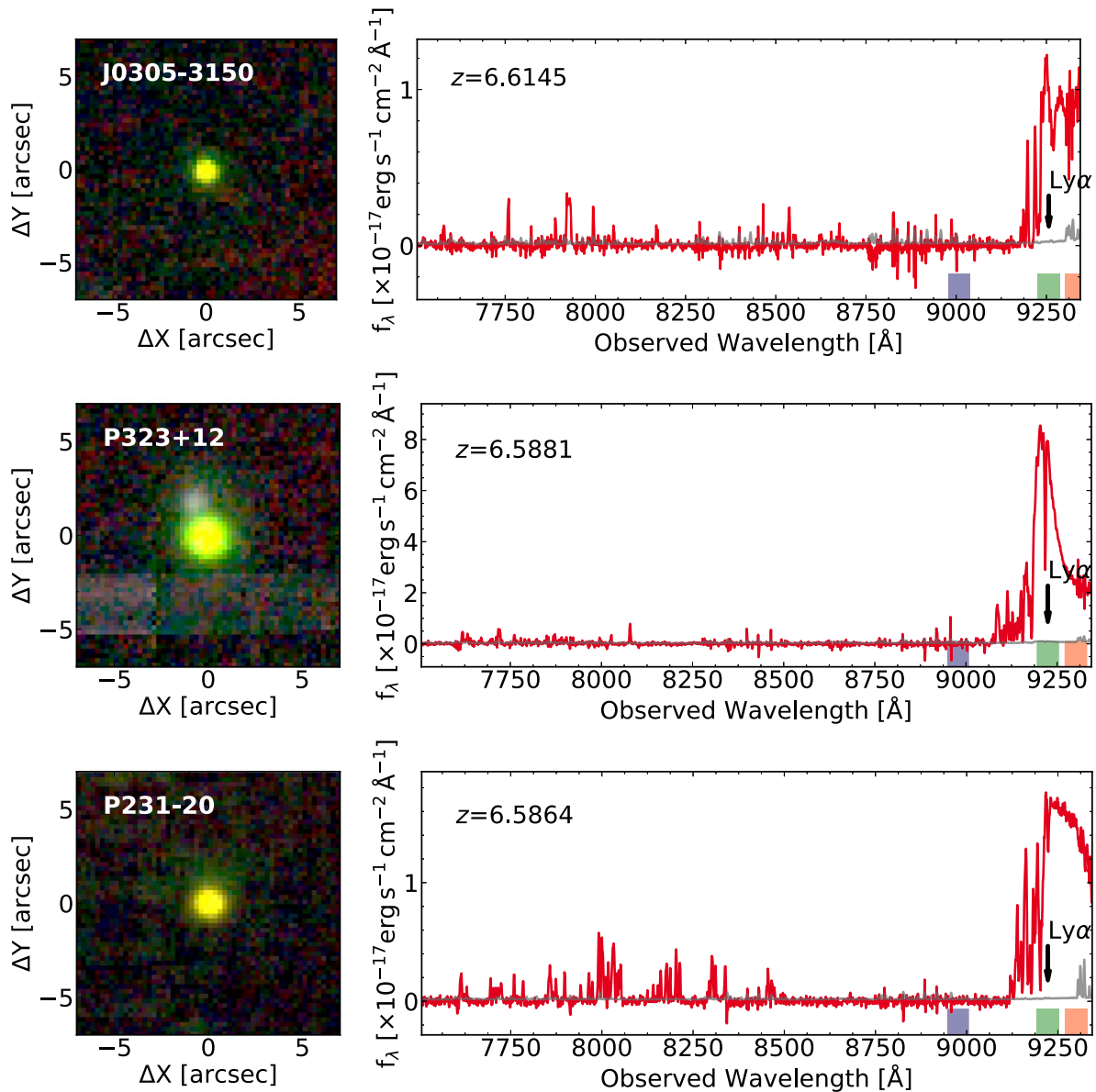
Figure 15. RGB images (left) and spectra (right) of the high-redshift quasars targeted in the REQUIEM survey (ordered by decreasing redshift). The wavelength ranges used to create the RGB images are highlighted with red, green, and blue boxes in the right panels. The wavelength of the Lyα line redshifted at z_{sys} is marked with a black arrow. (An extended version of this figure is available.)

Appendix B
The Spectrum of P009−10

The spectrum of P009−10 plotted in Figure 15 shows a deviation from the typical blue slope of quasars at $\lambda > 8700\,\text{Å}$. This behavior appears to be independent from the spectrophotometric star used for flux calibration and from the frames used to correct for flat field. We argue that this is most probably due to imperfect illumination correction due to the rapid variation of the sky conditions occurred during the observation of the target during the night of 2018 August 3. This is supported by the strong variation on the background in the red side of different MUSE IFUs. However, given that the Lyα line is redshifted at $\lambda \sim 8500\,\text{Å}$, this has no impact on the current analysis.

Appendix C
Analysis of the LBT/LUCI2 + ARGOS Images of P323+12

High-resolution *Ks*-band images of the quasar P323+12 have been collected with the Large Binocular Telescope (LBT; Hill & Salinari 2004; Hill et al. 2012) high with the Advanced Rayleigh-guided Ground-layer adaptive Optics System (*ARGOS*; Rabien et al. 2010, 2019) coupled with LUCI 2 (i.e., LBT Utility Camera in the Infrared; Seifert et al. 2003; Ageorges et al. 2010). Data were collected on 2017 October 25 during an *ARGOS* commissioning run. The total time on targets was 660 s, divided in 263 individual 2.51 s exposures. The data reduction has been performed with standard IRAF routines following the procedure described in Farina et al. (2018) and Georgiev et al. (2019). We registered
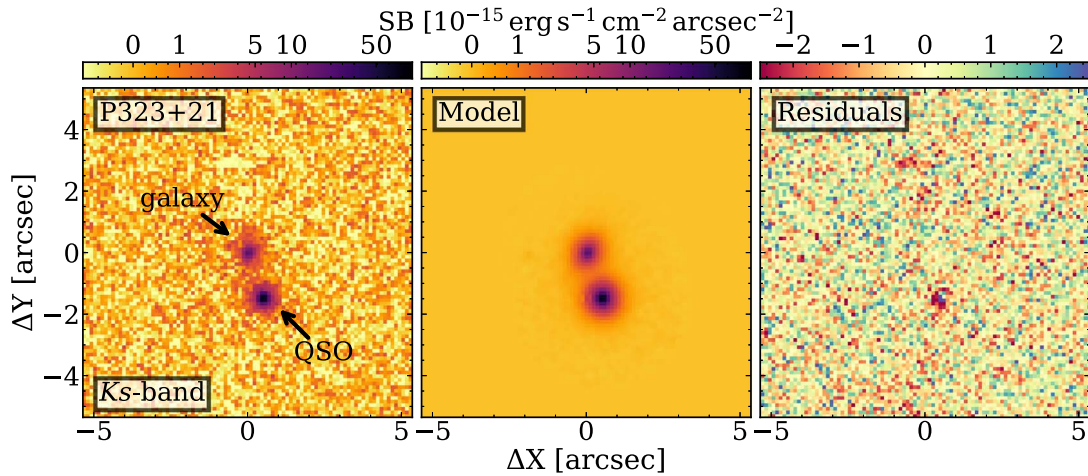
Figure 16. Results from the modeling of the quasar and close-by galaxy on the *Ks*-band images obtained with LBT/LUCI 2+ARGOS. Different panels show, from left to right: zoom-in on the $10'' \times 10''$ region centered on the galaxy; model of the quasar and galaxy emission; residuals after model subtraction (see Appendix C for details). In all panels, north is up and west is right.

the image to the WCS using the ASTROMETRY.NET software (Lang et al. 2010). The absolute flux calibration was achieved by matching sources with the 2MASS catalog (Cutri et al. 2003) and considering a Vega to AB conversion in the K_s band of $m_{AB} - m_{Vega} = 1.85$ mag. Uncertainty in the zero point is on the order of 0.1 mag. During the observations, the DIMM seeing was $1''34$ in the optical. The three green light (532 nm) lasers focused at 12 km used by *ARGOS* to correct for the ground-layer turbulence, allowed us to enhance the *Ks*-band image quality to $0''27$ (FWHM of an unresolved source) of the entire LUCI 2 field of view. The 5σ detection limit for a point source (estimated from the rms of the sky counts integrated over the radius of an unresolved source) is $Ks_{lim} = 23.9$ mag.[25]

We exploit this data to look for the possible presence of multiple lensed images of the quasar generated by the presence of the $z = 0.711$ elliptical galaxy located $1''6$ NNE from the quasar (see Section 5.7). First, we construct a spatially variable PSF model and evaluate it at the quasar location; for further details, see Farina et al. (2018) and Georgiev et al. (2019). Next, we use this model to subtract both the emission from both the quasar and the close-by galaxy using the GALFIT v3.0.5 package (Peng et al. 2010, 2011; see also our Figure 16). The galaxy emission is represented well by a Sérsic profile (Sérsic 1963) with magnitude $Ks_{gal} = (20.26 \pm 0.16)$ mag, effective radius $R_e = (1.1 \pm 0.3)''$, and Sérsic index $n = (4.9 \pm 2.1)$. The quasar is unresolved, with apparent magnitude $Ks_{QSO} = (19.33 \pm 0.11)$ mag (see Figure 16). This implies that the host galaxy is either compact (with radius <1.5 pkpc) or its emission is below a surface brightness of $\mu_{Ks,host} > 22.7$ mag arcsec^{-1} 5σ limit over a 1 arcsec^2 aperture). These limits are slightly looser, but consistent with those obtained by Mechtley et al. (2012) on the host galaxy of the $z = 6.42$ quasar J1148+5251.

In the residual image, we do not detect any source in the close proximity of the galaxy (down to a 2σ surface brightness limit of $\mu_{Ks,lim} > 23.7$ mag arcsec^{-1} over an aperture of 1 arcsec^2) that could be interpreted as multiple images of the quasar. This supports our simple model presented in Section 5.7, where we showed that the Einstein ring is expected to be smaller than the separation between the quasar and the galaxy (i.e., $<1''6$).

Appendix D
The Median Surface Brightness Profile

In Figure 17, we show the surface brightness profile computed by median combining the profiles extracted from the pseudo-narrowband images of quasars part of the *core sample* of our REQUIEM survey (see Section 4.2). Given the relatively small number of $z > 5.5$ quasars observed with MUSE, we are not able to estimate the incidence of outliers in our sample, such as the nebulae with sizes $\gg 100$ pkpc observed around $\sim 1\%$ of intermediate-redshift quasars (e.g., Hennawi et al. 2015; Arrigoni Battaia et al. 2019a). We thus consider the average surface brightness profile presented in Section 5.5 to be a more befitting depiction of the diffuse Lyα emission around $z \sim 6$ quasars. We notice, however, that our results do not depend on the type of profile chosen. A fit with the exponential function $(1 + z)^4 \, SB_{Ly\alpha}(r) = C \exp(-r/r_h)$ shows that the median profile has a slightly fainter normalization $[C = (2.2 \pm 0.3) \times 10^{-14} \, erg \, s^{-1} \, cm^{-2} \, arcsec^{-2}]$ and a similar scale length $[r_h = (8.9 \pm 0.6) \, kpc]$ with respect to the average profile (see Section 5.5 and Figure 17).

Measured average and median surface brightness radial profiles of the extended Lyα emission around $z \sim 6$ quasars are tabulated in Table 4.
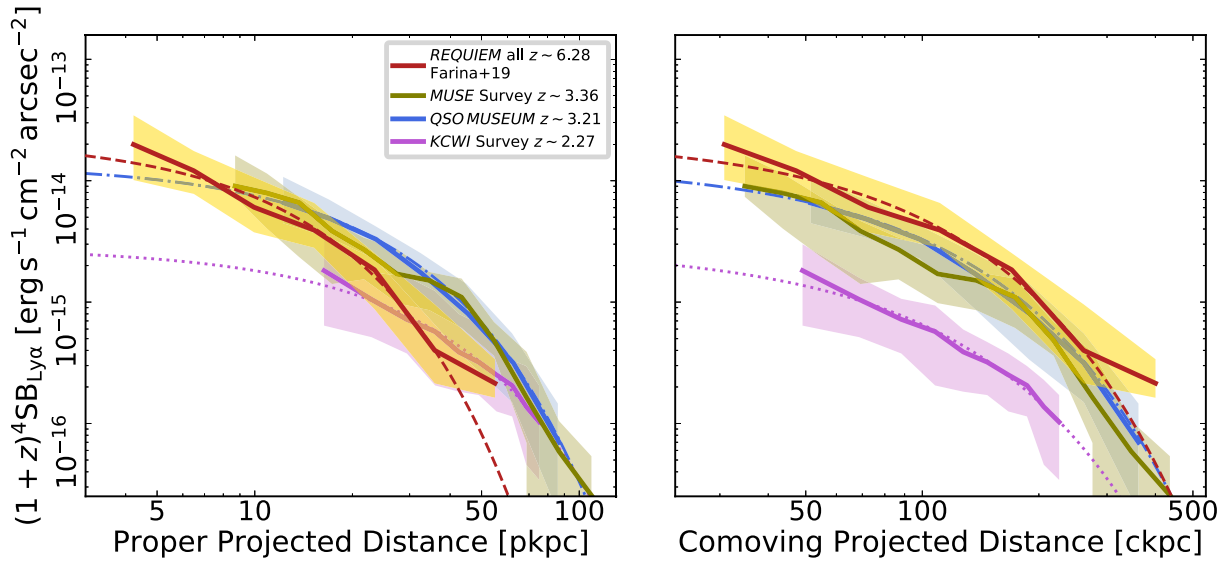
Figure 17. Left panel: median Lyα surface brightness profiles around quasars at different redshifts. Measurements from the *core sample* of our REQUIEM survey are shown as a dark orange line, those of Marino et al. (2019) as an olive green line, those of Arrigoni Battaia et al. (2019a) as a light blue line, and those of Cai et al. (2019) as a magenta line. All data are corrected for cosmological dimming. Shaded regions represents the 25th–75th percentiles in each quasar sample. Exponential best fits are shown in the same color palette. Right panel: same as left panel, but in comoving units.

Appendix E
List of Known Lyα Nebulae Associated with Quasars

Table 5 lists sizes and luminosities of the extended Lyα nebulae associated with quasars known as of the end of 2019

October. Data are homogenized to the cosmology used in this paper. However, no attempt has been made to correct for the different sensitivities or for the diverse observing techniques employed in the listed studies.

Table 5
Lyα Nebulae Associated with Quasars from the Literature

ID	Type	z	$d_{\mathrm{Ly\alpha}}$ (pkpc)	$L_{\mathrm{Ly\alpha}}$ (10^{43} erg s^{-1})	References
Q1658+575	QSO-RL	1.979	89	9.9	Heckman et al. (1991a)
Q0017+154	QSO-RL	2.012	97	12.9	Heckman et al. (1991a)
Q1354+258	QSO-RL	2.032	88	21.1	Heckman et al. (1991a)
Q0225−014	QSO-RL	2.037	44	5.3	Heckman et al. (1991a)
Q1345+258	QSO-RL	2.039	79	26.8	Heckman et al. (1991a)
Jackpot	4 × QSO	2.040	310	21.0	Hennawi et al. (2015)
Q0445+097	QSO–RL	2.113	106	7.3	Heckman et al. (1991a, 1991b)
J0112−0048	QSO	2.149	42	3.0	Fathivavsari et al. (2016)
Q0109+176	QSO-RL	2.157	26	1.5	Heckman et al. (1991a)
Q1318+113	QSO-RL	2.176	96	25.0	Heckman et al. (1991a, 1991b)
J1154−0215	QSO	2.181	50	2.4	Fathivavsari et al. (2016)
Q2125+0112	QSO	2.203	19	1.3	Cai et al. (2019)
Q0050+0051	QSO	2.222	116	2.0	Cai et al. (2019)
Q0814+3250	QSO	2.222	85	0.2	Cai et al. (2019)
Q1228+3128	QSO	2.231	124	12.3	Cai et al. (2019)
J2233−606	QSO	2.238	105	13.6	Bergeron et al. (1999)
Q1444+3904	QSO	2.250	101	10.1	Cai et al. (2019)
Q1426+2555	QSO	2.256	96	3.9	Cai et al. (2019)
Q2127+0049	QSO	2.261	58	1.1	Cai et al. (2019)
Q0107+0314	QSO	2.262	114	1.5	Cai et al. (2019)
Q1227+2848	QSO	2.268	164	5.8	Cai et al. (2019)
Q2123−0050	QSO	2.271	154	3.6	Cai et al. (2019)
Slug	2 × QSO	2.279	460	22.0	Cantalupo et al. (2014), Martin et al. (2015, 2019)
Q0052+0140	QSO	2.300	127	2.0	Cai et al. (2019)
Q1416+2649	QSO	2.301	141	5.0	Cai et al. (2019)
J1058+0315	QSO	2.302	34	1.6	Fathivavsari et al. (2016)
Q0848−0114	QSO	2.302	28	0.1	Cai et al. (2019)
MAMMOTH-1	QSO	2.311	442	51.0	Cai et al. (2017)

Table 5
(Continued)

ID	Type	z	$d_{Ly\alpha}$ (pkpc)	$L_{Ly\alpha}$ (10^{43} erg s^{-1})	References
Q1230+3320	QSO	2.313	204	12.4	Cai et al. (2019)
Q2150+053	QSO-RL	2.323	87	7.4	Heckman et al. (1991a)
Q0048+0056	QSO	2.327	104	2.3	Cai et al. (2019)
Q2222+051	QSO-RL	2.328	104	7.4	Heckman et al. (1991a)
NDFWS J143725+351048	QSO	2.332	80[a]	5.3	Yang et al. (2009)
Q2121+0052	QSO	2.377	141	4.6	Cai et al. (2019)
ELAN0101+020	$2 \times$ QSO	2.450	232	45.0	Cai et al. (2018)
J0049+3510	QSO	2.480	85	35.4	Barrio et al. (2008)
TXS 1436+157	QSO-RL	2.537	92	4.6	Roettgering et al. (1997), van Ojik et al. (1997), Humphrey et al. (2013)
Q2206−199	QSO	2.577	80	...[b]	Møller et al. (2000)
J0953+0349	QSO	2.594	29	1.3	Fathivavsari et al. (2016)
Q2338+042	QSO-RL	2.594	94	15.4	Heckman et al. (1991a), Lehnert & Becker (1998)
Q0758+097	QSO-RL	2.683	110	10.5	Heckman et al. (1991a, 1991b)
Q0730+257	QSO-RL	2.686	93	5.3	Heckman et al. (1991a)
AMS05	QSO	2.850	66	2.7	Smith et al. (2009)
Q0805+046	QSO-RL	2.877	116	62.8	Heckman et al. (1991a, 1991b)
Q0941+261	QSO-RL	2.913	99	6.4	Heckman et al. (1991a, 1991b)
J1253+1007	QSO	3.015	49	8.5	Fathivavsari et al. (2016)
CTS A31.05	QSO	3.020	120	6.1	Borisova et al. (2016)
J1135−0221	$2 \times$ QSO	3.020	60	32.0	Arrigoni Battaia et al. (2019b)
UM669	QSO	3.021	160	10.0	Borisova et al. (2016)
J0952+0114	QSO	3.020	58[a]	58.3	Marino et al. (2019)
Q0041−2638	QSO	3.036	170	2.9	Borisova et al. (2016)
SDSSJ0219−0215	QSO	3.036	87[a]	3.5	Arrigoni Battaia et al. (2019a)
Q1205−30	QSO	3.047	81[a]	5.8	Arrigoni Battaia et al. (2019a)
Q1759+7539	QSO	3.049	65	9.0	Christensen et al. (2006)
Q1205−30	QSO	3.040	40	6.3	Weidinger et al. (2004, 2005), Fynbo et al. (2000)
HE0940−1050	QSO	3.050	170	14.0	Borisova et al. (2016)
SDSSJ1342+1702	QSO	3.053	100[a]	2.4	Arrigoni Battaia et al. (2019a)
SDSSJ0947+1421	QSO	3.073	80[a]	2.0	Arrigoni Battaia et al. (2019a)
LBQS1209+1524	QSO	3.075	108[a]	3.2	Arrigoni Battaia et al. (2019a)
AWL 11	QSO	3.079	130	4.9	Borisova et al. (2016)
SDSSJ0100+2105	QSO	3.097	67[a]	5.0	Arrigoni Battaia et al. (2019a)
TEX1033+137	QSO-RL	3.097	122[a]	12.7	Arrigoni Battaia et al. (2019a)
Q-N1097.1	QSO	3.099	87[a]	3.0	Arrigoni Battaia et al. (2019a)
Q0058−292	QSO	3.101	109[a]	3.8	Arrigoni Battaia et al. (2019a)
S3 1013+20	QSO-RL	3.108	110[a]	5.6	Arrigoni Battaia et al. (2019a)
SDSSJ1240+1455	QSO	3.113	40	4.2	Matsuda et al. (2011)
CTS A11.09	QSO	3.121	150	2.1	Borisova et al. (2016)
J0525−233	QSO-RL	3.123	77[a]	1.2	Arrigoni Battaia et al. (2019a)
CT 656	QSO	3.125	130	2.8	Borisova et al. (2016)
SDSSJ1209+1138	QSO	3.126	83[a]	2.3	Arrigoni Battaia et al. (2019a)
CTSH22.05	QSO	3.127	123[a]	7.4	Arrigoni Battaia et al. (2019a)
UM672	QSO-RL	3.127	93[a]	6.5	Arrigoni Battaia et al. (2019a)
CTS B27.07	QSO	3.132	160	10.0	Borisova et al. (2016)
Q0140−306	QSO-RL	3.132	113[a]	5.1	Arrigoni Battaia et al. (2019a)
UM683	QSO	3.132	142[a]	7.9	Arrigoni Battaia et al. (2019a)
SDSSJ2100−0641	QSO	3.136	68[a]	2.1	Arrigoni Battaia et al. (2019a)
SDSSJ0814+1950	QSO-RL	3.137	50[a]	2.6	Arrigoni Battaia et al. (2019a)
SDSSJ0827+0300	QSO-RL	3.137	57[a]	0.8	Arrigoni Battaia et al. (2019a)
PKS0537−286	QSO-RL	3.141	112[a]	4.6	Arrigoni Battaia et al. (2019a)
Q2138−4427	QSO	3.142	82[a]	4.7	Arrigoni Battaia et al. (2019a)
SDSSJ1550+0537	QSO	3.147	99[a]	5.6	Arrigoni Battaia et al. (2019a)
LBQS1244+1129	QSO	3.157	101[a]	5.2	Arrigoni Battaia et al. (2019a)
6dF J0032−0414	QSO-RL	3.162	149[a]	35.7	Arrigoni Battaia et al. (2019a)
UM24	QSO	3.163	107[a]	2.6	Arrigoni Battaia et al. (2019a)
SDSSJ0905+0410	QSO-RL	3.165	98[a]	2.8	Arrigoni Battaia et al. (2019a)
PKS1017+109	QSO	3.167	185[a]	24.9	Arrigoni Battaia et al. (2019a)
SDSSJ1020+1040	$3 \times$ QSO	3.167	297	32.2	Arrigoni Battaia et al. (2018b)
SDSSJ2319−1040	QSO	3.172	86[a]	3.2	Arrigoni Battaia et al. (2019a)
SDSSJ1243+0720	QSO-RL	3.178	89[a]	5.1	Arrigoni Battaia et al. (2019a)
Q2204−408	QSO	3.179	30[a]	1.1	Arrigoni Battaia et al. (2019a)
J0823+0529	QSO	3.188	45	16.8	Fathivavsari et al. (2016)

Table 5
(Continued)

ID	Type	z	$d_{\mathrm{Ly}\alpha}$ (pkpc)	$L_{\mathrm{Ly}\alpha}$ (10^{43} erg s^{-1})	References
UM678	QSO	3.188	150	7.8	Borisova et al. (2016)
SDSSJ2348−1041	QSO	3.190	92[a]	2.3	Arrigoni Battaia et al. (2019a)
SDSSJ1032+1206	QSO-RL	3.195	58[a]	1.5	Arrigoni Battaia et al. (2019a)
Q0052−3901A	QSO-RL	3.203	120[a]	9.8	Arrigoni Battaia et al. (2019a)
UM670	QSO	3.203	92[a]	2.8	Arrigoni Battaia et al. (2019a)
Q1425+606	QSO	3.204	37	10.1	Christensen et al. (2006)
SDSSJ0819+0823	QSO	3.205	158[a]	38.7	Arrigoni Battaia et al. (2019a)
CTS G18.01	QSO	3.207	240	17.0	Borisova et al. (2016)
PKS1614+051	QSO	3.215	50	2.0	Husband et al. (2015)
UM679	QSO	3.215	94[a]	4.5	Arrigoni Battaia et al. (2019a)
PKS1614+051	QSO-RL	3.217	66	7.3	Hu & Cowie (1987)
CT-669	QSO	3.218	97[a]	11.0	Arrigoni Battaia et al. (2019a)
PKS1614+051	QSO	3.210	40	10.3	Matsuda et al. (2011)
Q0115−30	QSO	3.221	46[a]	0.3	Arrigoni Battaia et al. (2019a)
Q2139−4434	QSO	3.221	140[a]	6.8	Arrigoni Battaia et al. (2019a); Lusso et al. (2019)
Q2139−4433	QSO	3.229	100[a]	2.5	Lusso et al. (2019)
SDSSJ1307+1230	QSO	3.229	117[a]	7.0	Arrigoni Battaia et al. (2019a)
Q0347−383	QSO	3.230	113[a]	4.1	Arrigoni Battaia et al. (2019a)
SDSSJ2321+1558	QSO	3.241	71[a]	0.9	Arrigoni Battaia et al. (2019a)
SDSSJ1025+0452	QSO	3.243	144[a]	18.7	Arrigoni Battaia et al. (2019a)
CTS C22.31	QSO	3.246	101[a]	5.0	Arrigoni Battaia et al. (2019a)
Q0057−3948	QSO	3.251	107[a]	5.1	Arrigoni Battaia et al. (2019a)
Q1451+122	QSO	3.253	16	1.9	Christensen et al. (2006)
Q0042−2627	QSO	3.280	320	17.0	Borisova et al. (2016)
SDSSJ1557+1540	QSO	3.288	107[a]	21.8	Arrigoni Battaia et al. (2019a)
Q2233+131	QSO	3.301	11	1.2	Christensen et al. (2006)
Q0956+122	QSO	3.309	90	5.6	Fumagalli et al. (2016)
Q0956+1217	QSO	3.316	106[a]	5.3	Arrigoni Battaia et al. (2019a)
SDSSJ0125−1027	QSO	3.319	43[a]	2.3	Arrigoni Battaia et al. (2019a)
Q2348−4025	QSO	3.334	103[a]	5.1	Arrigoni Battaia et al. (2019a)
SDSSJ0250−0757	QSO	3.336	86[a]	2.9	Arrigoni Battaia et al. (2019a)
SDSSJ0817+1053	QSO	3.336	102[a]	5.0	Arrigoni Battaia et al. (2019a)
SDSSJ0154−0730	QSO	3.337	83[a]	3.3	Arrigoni Battaia et al. (2019a)
SDSSJ1337+0218	QSO	3.344	51[a]	0.5	Arrigoni Battaia et al. (2019a)
SDSSJ0001−0956	QSO-RL	3.348	131[a]	10.8	Arrigoni Battaia et al. (2019a)
CTS R07.04	QSO	3.351	170	33.0	Borisova et al. (2016)
SDSSJ1427−0029	QSO	3.354	49[a]	4.1	Arrigoni Battaia et al. (2019a)
Q0042−269	QSO	3.357	61[a]	1.0	Arrigoni Battaia et al. (2019a)
FBQSJ2334−0908	QSO-RL	3.361	52[a]	0.7	Arrigoni Battaia et al. (2019a)
Q2355p0108	QSO	3.395	121[a]	5.4	Arrigoni Battaia et al. (2019a)
SDSSJ1019+0254	QSO	3.395	73[a]	3.1	Arrigoni Battaia et al. (2019a)
SDSSJ1429−0145	QSO	3.425	79[a]	3.6	Arrigoni Battaia et al. (2019a)
SDSSJ1057−0139	QSO-RL	3.452	65[a]	1.7	Arrigoni Battaia et al. (2019a)
0054−284	QSO	3.616	38	0.8	Bremer et al. (1992)
Q0055−269	QSO	3.634	180	37.0	Borisova et al. (2016)
0055−264	QSO	3.656	30	1.1	Bremer et al. (1992)
Q1621−0042	QSO	3.689	120	5.5	Borisova et al. (2016)
Q1317−0507	QSO	3.701	140	3.6	Borisova et al. (2016)
QB2000−330	QSO-RL	3.759	120	12.0	Borisova et al. (2016)
PKS1937−101	QSO-RL	3.769	110	29.0	Borisova et al. (2016)
J0124+0044	QSO	3.783	190	41.0	Borisova et al. (2016)
BRI1108−07	QSO	3.907	160	12.0	Borisova et al. (2016)
Q0953+4749	QSO	4.489	14	0.8	Christensen et al. (2006), Bunker et al. (2003)
BR1033−0327	QSO	4.510	70	2.4	North et al. (2012); Courbin et al. (2008)
SDSSJ14472+0401	QSO	4.510	42	0.2	North et al. (2012)
SDSSJ21474−0838	QSO	4.510	56	23.2	North et al. (2012)
1605−0112	QSO	4.920	60	4.4	Ginolfi et al. (2018)
J2228+0110	QSO-RL	5.903	30	7.8	Roche et al. (2014), Drake et al. (2019), This work
P009−10	QSO	6.004	15	0.9	This work
P340−18	QSO	6.010	18	7.5	This work
P359−06	QSO	6.172	17	3.3	This work
P065−26	QSO	6.188	25	6.6	This work
P308−21	QSO	6.234	43	8.8	This work

<div align="center">

Table 5
(Continued)

</div>

ID	Type	z	$d_{\mathrm{Ly}\alpha}$ (pkpc)	$L_{\mathrm{Ly}\alpha}$ (10^{43} erg s^{-1})	References
J1030+0524	QSO	6.300	34	2.5	Decarli et al. (2012), Drake et al. (2019), This work
J2329−0301	QSO	6.416	22	5.1	This work
J2329−0301	QSO	6.416	22	5.1	Goto et al. (2009, 2012), Willott et al. (2011), Momose et al. (2019), Drake et al. (2019), This work
P036+03	QSO	6.541	19	3.8	This work
P231−20	QSO	6.586	28	11.0	Drake et al. (2019), This work
P323+12	QSO	6.588	25	20.1	This work
J0305−3150	QSO	6.615	17	0.8	Farina et al. (2017), This work

Notes. The "Type" indicates whether the nebula is associated with a radio-loud quasar (QSO-RL), a radio-quiet quasar (QSO), or with a system of multiple quasars ($N \times$ QSO). The size is the maximum diameter distance of the Lyα emission.
[a] Value calculated assuming a circular source, i.e., $d_{\mathrm{Ly}\alpha}$ is the diameter of a circle with area equal to the area of the source.
[b] Published spectrum not flux-calibrated.

(This table is available in machine-readable form.)

ORCID iDs

Emanuele Paolo Farina https://orcid.org/0000-0002-6822-2254
Fabrizio Arrigoni-Battaia https://orcid.org/0000-0002-4770-6137
Fabian Walter https://orcid.org/0000-0003-4793-7880
Joseph F. Hennawi https://orcid.org/0000-0002-7054-4332
Alyssa B. Drake https://orcid.org/0000-0002-0174-3362
Roberto Decarli https://orcid.org/0000-0002-2662-8803
Thales A. Gutcke https://orcid.org/0000-0001-6179-7701
Chiara Mazzucchelli https://orcid.org/0000-0002-5941-5214
Marcel Neeleman https://orcid.org/0000-0002-9838-8191
Iskren Georgiev https://orcid.org/0000-0001-8471-6679
Anna-Christina Eilers https://orcid.org/0000-0003-2895-6218
Frederick B. Davies https://orcid.org/0000-0003-0821-3644
Eduardo Bañados https://orcid.org/0000-0002-2931-7824
Xiaohui Fan https://orcid.org/0000-0003-3310-0131
Jan-Torge Schindler https://orcid.org/0000-0002-4544-8242
Bram P. Venemans https://orcid.org/0000-0001-9024-8322
Feige Wang https://orcid.org/0000-0002-7633-431X
Jinyi Yang https://orcid.org/0000-0001-5287-4242

References

Ageorges, N., Seifert, W., Jütte, M., et al. 2010, Proc. SPIE, 7735, 77351L
Alam, S. M. K., & Miralda-Escudé, J. 2002, ApJ, 568, 576
Arrigoni Battaia, F., Chen, C.-C., Fumagalli, M., et al. 2018a, A&A, 620, A202
Arrigoni Battaia, F., Hennawi, J. F., Cantalupo, S., & Prochaska, J. X. 2016, ApJ, 829, 3
Arrigoni Battaia, F., Hennawi, J. F., Prochaska, J. X., et al. 2015a, ApJ, 809, 163
Arrigoni Battaia, F., Hennawi, J. F., Prochaska, J. X., et al. 2019a, MNRAS, 482, 3162
Arrigoni Battaia, F., Obreja, A., Prochaska, J. X., et al. 2019b, A&A, 631, A18
Arrigoni Battaia, F., Prochaska, J. X., Hennawi, J. F., et al. 2018b, MNRAS, 473, 3907
Arrigoni Battaia, F., Yang, Y., Hennawi, J. F., et al. 2015b, ApJ, 804, 26
Astropy Collaboration, Price-Whelan, A. M., Sipőcz, B. M., et al. 2018, AJ, 156, 123
Astropy Collaboration, Robitaille, T. P., Tollerud, E. J., et al. 2013, A&A, 558, A33
Atek, H., Kunth, D., Hayes, M., et al. 2008, A&A, 488, 491

Bacon, R., Accardo, M., Adjali, L., et al. 2010, Proc. SPIE, 7735, 773508
Bacon, R., Brinchmann, J., Richard, J., et al. 2015, A&A, 575, A75
Bădescu, T., Yang, Y., Bertoldi, F., et al. 2017, ApJ, 845, 172
Bahcall, J. N., & Spitzer, L. 1969, ApJL, 156, L63
Balmaverde, B., Gilli, R., Mignoli, M., et al. 2017, A&A, 606, A23
Bañados, E., Decarli, R., Walter, F., et al. 2015a, ApJL, 805, L8
Bañados, E., Rauch, M., Decarli, R., et al. 2019, ApJ, 885, 59
Bañados, E., Venemans, B. P., Decarli, R., et al. 2016, ApJS, 227, 11
Bañados, E., Venemans, B. P., Mazzucchelli, C., et al. 2018, Natur, 553, 473
Bañados, E., Venemans, B. P., Morganson, E., et al. 2015b, ApJ, 804, 118
Barnett, R., Warren, S. J., Banerji, M., et al. 2015, A&A, 575, A31
Barrio, F. E., Jarvis, M. J., Rawlings, S., et al. 2008, MNRAS, 389, 792
Beelen, A., Cox, P., Benford, D. J., et al. 2006, ApJ, 642, 694
Behroozi, P. S., Wechsler, R. H., & Conroy, C. 2013, ApJ, 770, 57
Bergeron, J., Petitjean, P., Cristiani, S., et al. 1999, A&A, 343, L40
Bieri, R., Dubois, Y., Rosdahl, J., et al. 2017, MNRAS, 464, 1854
Bolton, J. S., & Haehnelt, M. G. 2007, MNRAS, 374, 493
Borisova, E., Cantalupo, S., Lilly, S. J., et al. 2016, ApJ, 831, 39
Bouché, N., Murphy, M. T., Kacprzak, G. G., et al. 2013, Sci, 341, 50
Bowen, D. V., Hennawi, J. F., Ménard, B., et al. 2006, ApJL, 645, L105
Bremer, M. N., Fabian, A. C., Sargent, W. L. W., et al. 1992, MNRAS, 258, 23P
Brook, C. B., Governato, F., Roškar, R., et al. 2011, MNRAS, 415, 1051
Bunker, A., Smith, J., Spinrad, H., Stern, D., & Warren, S. 2003, Ap&SS, 284, 357
Cai, Z., Cantalupo, S., Prochaska, J. X., et al. 2019, ApJS, 245, 23
Cai, Z., Fan, X., Yang, Y., et al. 2017, ApJ, 837, 71
Cai, Z., Hamden, E., Matuszewski, M., et al. 2018, ApJL, 861, L3
Cantalupo, S. 2017, in Gas Accretion onto Galaxies, ed. A. Fox & R. Davé (Berlin: Springer), 195
Cantalupo, S., Arrigoni-Battaia, F., Prochaska, J. X., Hennawi, J. F., & Madau, P. 2014, Natur, 506, 63
Cantalupo, S., Pezzulli, G., Lilly, S. J., et al. 2019, MNRAS, 483, 5188
Cantalupo, S., Porciani, C., Lilly, S. J., et al. 2005, ApJ, 628, 61
Cardelli, J. A., Clayton, G. C., & Mathis, J. S. 1989, ApJ, 345, 245
Carilli, C. L., Wang, R., Fan, X., et al. 2010, ApJ, 714, 834
Casey, C. M., Scoville, N. Z., Sanders, D. B., et al. 2014, ApJ, 796, 95
Cen, R., & Haiman, Z. 2000, ApJL, 542, L75
Chambers, K. C., Magnier, E. A., Metcalfe, N., et al. 2016, arXiv:1612.05560
Chen, D. N., Jing, Y. P., & Yoshikaw, K. 2003, ApJ, 597, 35
Chen, H.-W., Helsby, J. E., Gauthier, J.-R., et al. 2010a, ApJ, 714, 1521
Chen, H.-W., & Tinker, J. L. 2008, ApJ, 687, 745
Chen, H.-W., Wild, V., Tinker, J. L., et al. 2010b, ApJL, 724, L176
Chieregato, M., Miranda, M., & Jetzer, P. 2007, A&A, 474, 777
Christensen, L., Jahnke, K., Wisotzki, L., & Sánchez, S. F. 2006, A&A, 459, 717
Churchill, C. W., Nielsen, N. M., Kacprzak, G. G., et al. 2013a, ApJL, 763, L42
Churchill, C. W., Trujillo-Gomez, S., Nielsen, N. M., et al. 2013b, ApJ, 779, 87
Connor, T., Bañados, E., Stern, D., et al. 2019, arXiv:1909.08619
Costa, T., Sijacki, D., & Haehnelt, M. G. 2015, MNRAS, 448, L30

Costa, T., Sijacki, D., Trenti, M., et al. 2014, MNRAS, 439, 2146
Courbin, F., North, P., Eigenbrod, A., & Chelouche, D. 2008, A&A, 488, 91
Cutri, R. M., Skrutskie, M. F., van Dyk, S., et al. 2003, 2MASS All Sky
    Catalog of Point Sources
D'Odorico, V., Feruglio, C., Ferrara, A., et al. 2018, ApJL, 863, L29
Davies, F. B., Hennawi, J. F., & Eilers, A.-C. 2019a, ApJL, 884, L19
Davies, F. B., Hennawi, J. F., & Eilers, A.-C. 2019b, MNRAS, in press
Davis, S. W., & Laor, A. 2011, ApJ, 728, 98
De Looze, I., Cormier, D., Lebouteiller, V., et al. 2014, A&A, 568, A62
De Rosa, G., Decarli, R., Walter, F., et al. 2011, ApJ, 739, 56
De Rosa, G., Venemans, B. P., Decarli, R., et al. 2014, ApJ, 790, 145
Decarli, R., Dotti, M., Bañados, E., et al. 2019a, ApJ, 880, 157
Decarli, R., Mignoli, M., Gilli, R., et al. 2019b, A&A, 631, L10
Decarli, R., Treves, A., & Falomo, R. 2009, MNRAS, 396, L31
Decarli, R., Walter, F., Venemans, B. P., et al. 2017, Natur, 545, 457
Decarli, R., Walter, F., Venemans, B. P., et al. 2018, ApJ, 854, 97
Decarli, R., Walter, F., Yang, Y., et al. 2012, ApJ, 756, 150
Dekel, A., & Birnboim, Y. 2006, MNRAS, 368, 2
Dekel, A., Birnboim, Y., Engel, G., et al. 2009, Natur, 457, 451
Dekel, A., Lapiner, S., & Dubois, Y. 2019, arXiv:1904.08431
Di Matteo, T., Croft, R. A. C., Feng, Y., Waters, D., & Wilkins, S. 2017,
    MNRAS, 467, 4243
Di Matteo, T., Khandai, N., DeGraf, C., et al. 2012, ApJL, 745, L29
Dijkstra, M. 2017, arXiv:1704.03416
Dijkstra, M., & Loeb, A. 2008, MNRAS, 386, 492
Dijkstra, M., & Loeb, A. 2009, MNRAS, 400, 1109
Draine, B. T. (ed.) 2011, Physics of the Interstellar and Intergalactic Medium
    (Princeton, NJ: Princeton Univ. Press)
Drake, A. B., Farina, E. P., Neeleman, M., et al. 2019, ApJ, 881, 131
Dubois, Y., Pichon, C., Haehnelt, M., et al. 2012, MNRAS, 423, 3616
Dutton, A. A., & Macciò, A. V. 2014, MNRAS, 441, 3359
Efstathiou, G., & Rees, M. J. 1988, MNRAS, 230, 5p
Eftekharzadeh, S., Myers, A. D., White, M., et al. 2015, MNRAS, 453, 2779
Eilers, A.-C., Davies, F. B., Hennawi, J. F., et al. 2017, ApJ, 840, 24
Eilers, A.-C., Hennawi, J. F., & Davies, F. B. 2018, ApJ, 867, 30
Erb, D. K., Steidel, C. C., & Chen, Y. 2018, ApJL, 862, L10
Faber, S. M., & Jackson, R. E. 1976, ApJ, 204, 668
Fall, S. M., & Efstathiou, G. 1980, MNRAS, 193, 189
Fan, X., Narayanan, V. K., Lupton, R. H., et al. 2001, AJ, 122, 2833
Fan, X., Strauss, M. A., Becker, R. H., et al. 2006, AJ, 132, 117
Fan, X., Strauss, M. A., Schneider, D. P., et al. 2003, AJ, 125, 1649
Fanidakis, N., Macciò, A. V., Baugh, C. M., et al. 2013, MNRAS, 436, 315
Fardal, M. A., Katz, N., Gardner, J. P., et al. 2001, ApJ, 562, 605
Farina, E. P., Falomo, R., Decarli, R., et al. 2013, MNRAS, 429, 1267
Farina, E. P., Falomo, R., Scarpa, R., et al. 2014, MNRAS, 441, 886
Farina, E. P., Georgiev, I. Y., Decarli, R., et al. 2018, MNRAS, 476, 1835
Farina, E. P., Venemans, B. P., Decarli, R., et al. 2017, ApJ, 848, 78
Fasano, G., & Franceschini, A. 1987, MNRAS, 225, 155
Fathivavsari, H., Petitjean, P., Noterdaeme, P., et al. 2016, MNRAS, 461, 1816
Feng, Y., Di Matteo, T., Croft, R., & Khandai, N. 2014, MNRAS, 440, 1865
Fitzpatrick, E. L. 1999, PASP, 111, 63
Flewelling, H. A., Magnier, E. A., Chambers, K. C., et al. 2016, arXiv:1612.
    05243
Fumagalli, M., Cantalupo, S., Dekel, A., et al. 2016, MNRAS, 462, 1978
Fumagalli, M., Prochaska, J. X., Kasen, D., et al. 2011, MNRAS, 418, 1796
Furlanetto, S. R., Schaye, J., Springel, V., et al. 2005, ApJ, 622, 7
Fynbo, J. U., Thomsen, B., & Møller, P. 2000, A&A, 353, 457
García-Vergara, C., Hennawi, J. F., Barrientos, L. F., & Rix, H.-W. 2017, ApJ,
    848, 7
Gauthier, J.-R., Chen, H.-W., & Tinker, J. L. 2010, ApJ, 716, 1263
Georgiev, I. Y., Neumayer, N., Gässler, W., et al. 2019, MNRAS, 484, 3356
Ginolfi, M., Maiolino, R., Carniani, S., et al. 2018, MNRAS, 476, 2421
Goto, T., Utsumi, Y., Furusawa, H., Miyazaki, S., & Komiyama, Y. 2009,
    MNRAS, 400, 843
Goto, T., Utsumi, Y., Kikuta, S., et al. 2017, MNRAS, 470, L117
Goto, T., Utsumi, Y., Walsh, J. R., et al. 2012, MNRAS, 421, L77
Gould, A., & Weinberg, D. H. 1996, ApJ, 468, 462
Greene, J. E., Zakamska, N. L., & Smith, P. S. 2012, ApJ, 746, 86
Gronwall, C., Ciardullo, R., Hickey, T., et al. 2007, ApJ, 667, 79
Gunn, J. E., & Peterson, B. A. 1965, ApJ, 142, 1633
Habouzit, M., Volonteri, M., Somerville, R. S., et al. 2019, MNRAS,
    489, 1206
Haiman, Z., & Cen, R. 2001, in ASP Conf. Proc. 222, The Physics of Galaxy
    Formation, ed. M. Umemura & H. Susa (San Francisco, CA: ASP), 101
Haiman, Z., & Rees, M. J. 2001, ApJ, 556, 87
Haiman, Z., Spaans, M., & Quataert, E. 2000, ApJL, 537, L5

Hayes, M., Schaerer, D., Östlin, G., et al. 2011, ApJ, 730, 8
He, W., Akiyama, M., Bosch, J., et al. 2018, PASJ, 70, S33
Heckman, T. M., Lehnert, M. D., Miley, G. K., & van Breugel, W. 1991a, ApJ,
    381, 373
Heckman, T. M., Miley, G. K., Lehnert, M. D., & van Breugel, W. 1991b, ApJ,
    370, 78
Hennawi, J. F., & Prochaska, J. X. 2007, ApJ, 655, 735
Hennawi, J. F., & Prochaska, J. X. 2013, ApJ, 766, 58
Hennawi, J. F., Prochaska, J. X., Burles, S., et al. 2006, ApJ, 651, 61
Hennawi, J. F., Prochaska, J. X., Cantalupo, S., & Arrigoni-Battaia, F. 2015,
    Sci, 348, 779
Hennawi, J. F., Prochaska, J. X., Kollmeier, J., et al. 2009, ApJL, 693, L49
Herenz, E. C., Wisotzki, L., Roth, M., et al. 2015, A&A, 576, A115
Hill, J. M., Green, R. F., Ashby, D. S., et al. 2012, Proc. SPIE, 8444, 84441A
Hill, J. M., & Salinari, P. 2004, Proc. SPIE, 5489, 603
Hoyle, F. 1951, Problems of Cosmical Aerodynamics, 195
Hu, E. M., & Cowie, L. L. 1987, ApJL, 317, L7
Humphrey, A., Binette, L., Villar-Martín, M., Aretxaga, I., & Papaderos, P.
    2013, MNRAS, 428, 563
Husband, K., Bremer, M. N., Stanway, E. R., et al. 2015, MNRAS, 452, 2388
Izumi, T., Onoue, M., Shirakata, H., et al. 2018, PASJ, 70, 36
Jiang, L., McGreer, I. D., Fan, X., et al. 2016, ApJ, 833, 222
Johnson, S. D., Chen, H.-W., & Mulchaey, J. S. 2015, MNRAS, 452, 2553
Kashikawa, N., Ishizaki, Y., Willott, C. J., et al. 2015, ApJ, 798, 28
Kellermann, K. I., Sramek, R., Schmidt, M., Shaffer, D. B., & Green, R. 1989,
    AJ, 98, 1195
Kennicutt, R. C., & Evans, N. J. 2012, ARA&A, 50, 531
Kereš, D., & Hernquist, L. 2009, ApJL, 700, L1
Kereš, D., Katz, N., Fardal, M., et al. 2009, MNRAS, 395, 160
Kereš, D., Katz, N., Weinberg, D. H., et al. 2005, MNRAS, 363, 2
Kim, Y., & Im, M. 2019, ApJ, 879, 117
Kunth, D., Mas-Hesse, J. M., Terlevich, E., et al. 1998, A&A, 334, 11
Lang, D., Hogg, D. W., Mierle, K., et al. 2010, AJ, 139, 1782
Lau, M. W., Prochaska, J. X., & Hennawi, J. F. 2016, ApJS, 226, 25
Lau, M. W., Prochaska, J. X., & Hennawi, J. F. 2018, ApJ, 857, 126
Leclercq, F., Bacon, R., Wisotzki, L., et al. 2017, A&A, 608, A8
Lehnert, M. D., & Becker, R. H. 1998, A&A, 332, 514
Leibler, C. N., Cantalupo, S., Holden, B. P., et al. 2018, MNRAS, 480, 2094
Leipski, C., Meisenheimer, K., Walter, F., et al. 2014, ApJ, 785, 154
Li, Y., Hernquist, L., Robertson, B., et al. 2007, ApJ, 665, 187
Lusso, E., Fumagalli, M., Fossati, M., et al. 2019, MNRAS: Lett., 485, L62
Lusso, E., Worseck, G., Hennawi, J. F., et al. 2015, MNRAS, 449, 4204
Lyman, T. 1906, ApJ, 23, 181
MacLeod, C. L., Ivezić, Ž, Sesar, B., et al. 2012, ApJ, 753, 106
Madau, P., & Rees, M. J. 2000, ApJL, 542, L69
Mannucci, F., Basile, F., Poggianti, B. M., et al. 2001, MNRAS, 326, 745
Marino, R. A., Cantalupo, S., Pezzulli, G., et al. 2019, ApJ, 880, 47
Martin, D. C., Chang, D., Matuszewski, M., et al. 2014, ApJ, 786, 106
Martin, D. C., Matuszewski, M., Morrissey, P., et al. 2015, Natur, 524, 192
Martin, D. C., O'Sullivan, D., Matuszewski, M., et al. 2019, NatAs, 3, 822
Matsuda, Y., Yamada, T., Hayashino, T., et al. 2011, MNRAS, 410, L13
Matsuoka, Y., Onoue, M., Kashikawa, N., et al. 2016, ApJ, 828, 26
Matsuoka, Y., Onoue, M., Kashikawa, N., et al. 2018, PASJ, 70, S35
Mayer, L., & Bonoli, S. 2019, RPPh, 82, 016901
Mazzucchelli, C., Bañados, E., Venemans, B. P., et al. 2017, ApJ, 849, 91
Mazzucchelli, C., Decarli, R., Farina, E. P., et al. 2019, ApJ, 881, 163
Mechtley, M., Windhorst, R. A., Ryan, R. E., et al. 2012, ApJL, 756, L38
Ménard, B., Scranton, R., Fukugita, M., & Richards, G. 2010, MNRAS,
    405, 1025
Millikan, R. A. 1920, ApJ, 52, 47
Mo, H. J., Mao, S., & White, S. D. M. 1998, MNRAS, 295, 319
Møller, P., Warren, S. J., Fall, S. M., et al. 2000, Msngr, 99, 33
Momose, R., Goto, T., Utsumi, Y., et al. 2019, MNRAS, 488, 120
Mori, M., Umemura, M., & Ferrara, A. 2004, ApJL, 613, L97
Morrissey, P., Matuszewski, M., Martin, C., et al. 2012, Proc. SPIE, 8446,
    844613
Morrissey, P., Matuszewski, M., Martin, D. C., et al. 2018, ApJ, 864, 93
Morselli, L., Mignoli, M., Gilli, R., et al. 2014, A&A, 568, A1
Mortlock, D. J., Warren, S. J., Venemans, B. P., et al. 2011, Natur, 474, 616
Narayan, R., & Schneider, P. 1990, MNRAS, 243, 192
Navarro, J. F., Frenk, C. S., & White, S. D. M. 1997, ApJ, 490, 493
Neeleman, M., Bañados, E., Walter, F., et al. 2019, ApJ, 882, 10
Neeleman, M., Kanekar, N., Prochaska, J. X., et al. 2017, Sci, 355, 1285
Neeleman, M., Kanekar, N., Prochaska, J. X., et al. 2018, ApJL, 856, L12
Neeleman, M., Prochaska, J. X., Zwaan, M. A., et al. 2016, ApJL, 820, L39
Nielsen, N. M., Churchill, C. W., Kacprzak, G. G., et al. 2013a, ApJ, 776, 114

Nielsen, N. M., Churchill, C. W., & Kacprzak, G. G. 2013b, ApJ, 776, 115
Nigoche-Netro, A., Aguerri, J. A. L., Lagos, P., et al. 2010, A&A, 516, A96
North, P. L., Courbin, F., Eigenbrod, A., & Chelouche, D. 2012, A&A, 542, A91
Ono, Y., Ouchi, M., Shimasaku, K., et al. 2010, ApJ, 724, 1524
Osterbrock, D. E., & Ferland, G. J. 2006, Astrophysics of Gaseous Nebulae and Active Galactic Nuclei (Sausalito, CA: Univ. Science Books)
Ota, K., Venemans, B. P., Taniguchi, Y., et al. 2018, ApJ, 856, 109
Oyarzún, G. A., Blanc, G. A., González, V., et al. 2017, ApJ, 843, 133
Peacock, J. A. 1999, Cosmological Physics (Cambridge: Cambridge Univ. Press)
Peng, C. Y., Ho, L. C., Impey, C. D., & Rix, H.-W. 2010, AJ, 139, 2097
Peng, C. Y., Ho, L. C., Impey, C. D., & Rix, H.-W. 2011, GALFIT v3.0.5, Astrophysics Source Code Library, ascl:1104.010
Planck Collaboration et al. 2014, A&A, 571, A16
Pons, E., McMahon, R. G., Simcoe, R. A., et al. 2019, MNRAS, 484, 5142
Prieto, J., Jimenez, R., Haiman, Z., et al. 2015, MNRAS, 452, 784
Prochaska, J. X., & Hennawi, J. F. 2009, ApJ, 690, 1558
Prochaska, J. X., Hennawi, J. F., Lee, K.-G., et al. 2013a, ApJ, 776, 136
Prochaska, J. X., Hennawi, J. F., & Simcoe, R. A. 2013b, ApJL, 762, L19
Prochaska, J. X., Lau, M. W., & Hennawi, J. F. 2014, ApJ, 796, 140
Rabien, S., Ageorges, N., Barl, L., et al. 2010, Proc. SPIE, 7736, 77360E
Rabien, S., Angel, R., Barl, L., et al. 2019, A&A, 621, A4
Reed, S. L., Banerji, M., Becker, G. D., et al. 2019, MNRAS, 487, 1874
Reed, S. L., McMahon, R. G., Martini, P., et al. 2017, MNRAS, 468, 4702
Rees, M. J. 1988, MNRAS, 231, 91p
Richards, G. T., Vanden Berk, D. E., Reichard, T. A., et al. 2002, AJ, 124, 1
Roche, N., Humphrey, A., & Binette, L. 2014, MNRAS, 443, 3795
Roettgering, H. J. A., van Ojik, R., Miley, G. K., et al. 1997, A&A, 326, 505
Roussel, H., Wilson, C. D., Vigroux, L., et al. 2010, A&A, 518, L66
Sales, L. V., Navarro, J. F., Theuns, T., et al. 2012, MNRAS, 423, 1544
Salpeter, E. E. 1964, ApJ, 140, 796
Schlafly, E. F., & Finkbeiner, D. P. 2011, ApJ, 737, 103
Seifert, W., Appenzeller, I., Baumeister, H., et al. 2003, Proc. SPIE, 4841, 962
Sérsic, J. L. 1963, BAAA, 6, 41
Shankar, F., Crocce, M., Miralda-Escudé, J., Fosalba, P., & Weinberg, D. H. 2010, ApJ, 718, 231
Shao, Y., Wang, R., Carilli, C. L., et al. 2019, ApJ, 876, 99
Shen, Y., Brandt, W. N., Richards, G. T., et al. 2016, ApJ, 831, 7
Shen, Y., Strauss, M. A., Oguri, M., et al. 2007, AJ, 133, 2222
Shen, Y., Wu, J., Jiang, L., et al. 2019, ApJ, 873, 35
Sijacki, D., Springel, V., & Haehnelt, M. G. 2009, MNRAS, 400, 100
Smith, D. J. B., Jarvis, M. J., Simpson, C., & Martínez-Sansigre, A. 2009, MNRAS, 393, 309
Sobral, D., & Matthee, J. 2019, A&A, 623, A157
Soltan, A. 1982, MNRAS, 200, 115
Soto, K. T., Lilly, S. J., Bacon, R., Richard, J., & Conseil, S. 2016, MNRAS, 458, 3210
Steidel, C. C., Dickinson, M., & Persson, S. E. 1994, ApJL, 437, L75
Stewart, K. R., Maller, A. H., Oñorbe, J., et al. 2017, ApJ, 843, 47
Straatman, C. M. S., Labbé, I., Spitler, L. R., et al. 2014, ApJL, 783, L14
Straatman, C. M. S., Spitler, L. R., Quadri, R. F., et al. 2016, ApJ, 830, 51
Stuik, R., Bacon, R., Conzelmann, R., et al. 2006, NewAR, 49, 618
Tanaka, T., & Haiman, Z. 2009, ApJ, 696, 1798
Taniguchi, Y., & Shioya, Y. 2000, ApJL, 532, L13
Timlin, J. D., Ross, N. P., Richards, G. T., et al. 2018, ApJ, 859, 20
Tody, D. 1986, Proc. SPIE, 627, 733
Tody, D. 1993, in ASP Conf. Ser. 52, Astronomical Data Analysis Software and Systems II, ed. R. J. Hanisch, R. J. V. Brissenden, & J. Barnes (San Francisco, CA: ASP), 173
Tormen, G., Bouchet, F. R., & White, S. D. M. 1997, MNRAS, 286, 865
Tremonti, C. A., Moustakas, J., & Diamond-Stanic, A. M. 2007, ApJL, 663, L77
Tumlinson, J., Peeples, M. S., & Werk, J. K. 2017, ARA&A, 55, 389
van de Voort, F., Schaye, J., Altay, G., et al. 2012, MNRAS, 421, 2809
van Ojik, R., Roettgering, H. J. A., Miley, G. K., & Hunstead, R. W. 1997, A&A, 317, 358
Venemans, B. P., Bañados, E., Decarli, R., et al. 2015, ApJL, 801, L11
Venemans, B. P., Decarli, R., Walter, F., et al. 2018, ApJ, 866, 159
Venemans, B. P., Findlay, J. R., Sutherland, W. J., et al. 2013, ApJ, 779, 24
Venemans, B. P., McMahon, R. G., Walter, F., et al. 2012, ApJL, 751, L25
Venemans, B. P., Neeleman, M., Walter, F., et al. 2019, ApJL, 874, L30
Venemans, B. P., Walter, F., Zschaechner, L., et al. 2016, ApJ, 816, 37
Verhamme, A., Schaerer, D., & Maselli, A. 2006, A&A, 460, 397
Villar-Martín, M. 2007, NewAR, 51, 194
Volonteri, M. 2010, A&ARv, 18, 279
Volonteri, M. 2012, Sci, 337, 544
Volonteri, M., Natarajan, P., & Gültekin, K. 2011, ApJ, 737, 50
Volonteri, M., & Rees, M. J. 2005, ApJ, 633, 624
Volonteri, M., & Rees, M. J. 2006, ApJ, 650, 669
Walter, F., Riechers, D., Cox, P., et al. 2009, Natur, 457, 699
Wang, F., Wang, R., Fan, X., et al. 2019a, ApJ, 880, 2
Wang, F., Yang, J., Fan, X., et al. 2019b, ApJ, 884, 30
Wang, R., Shao, Y., Carilli, C. L., et al. 2019c, arXiv:1904.07749
Wang, R., Wagg, J., Carilli, C. L., et al. 2013, ApJ, 773, 44
Wang, R., Wu, X.-B., Neri, R., et al. 2016, ApJ, 830, 53
Weidinger, M., Møller, P., & Fynbo, J. P. U. 2004, Natur, 430, 999
Weidinger, M., Møller, P., Fynbo, J. P. U., & Thomsen, B. 2005, A&A, 436, 825
Weilbacher, P. M., Streicher, O., Urrutia, T., et al. 2012, Proc. SPIE, 8451, 84510B
Weilbacher, P. M., Streicher, O., Urrutia, T., et al. 2014, in ASP Conf. Ser. 485, Astronomical Data Analysis Software and Systems XXIII, ed. N. Manset & P. Forshay (San Francisco, CA: ASP), 451
Werk, J. K., Prochaska, J. X., Cantalupo, S., et al. 2016, ApJ, 833, 54
White, M., Myers, A. D., Ross, N. P., et al. 2012, MNRAS, 424, 933
White, S. D. M., & Rees, M. J. 1978, MNRAS, 183, 341
Willott, C. J., Bergeron, J., & Omont, A. 2015, ApJ, 801, 123
Willott, C. J., Bergeron, J., & Omont, A. 2017, ApJ, 850, 108
Willott, C. J., Chet, S., Bergeron, J., & Hutchings, J. B. 2011, AJ, 142, 186
Willott, C. J., Delorme, P., Omont, A., et al. 2007, AJ, 134, 2435
Willott, C. J., Delorme, P., Reylé, C., et al. 2010, AJ, 139, 906
Willott, C. J., Omont, A., & Bergeron, J. 2013, ApJ, 770, 13
Wisotzki, L., Bacon, R., Blaizot, J., et al. 2016, A&A, 587, A98
Wu, X.-B., Wang, F., Fan, X., et al. 2015, Natur, 518, 512
Yang, J., Venemans, B., Wang, F., et al. 2019a, ApJ, 880, 153
Yang, J., Wang, F., Fan, X., et al. 2019b, AJ, 157, 236
Yang, Q., Shen, Y., Chen, Y.-C., et al. 2019c, arXiv:1904.10912
Yang, Y., Zabludoff, A., Tremonti, C., et al. 2009, ApJ, 693, 1579
Yoo, J., & Miralda-Escudé, J. 2004, ApJL, 614, L25
Zeimann, G. R., White, R. L., Becker, R. H., et al. 2011, ApJ, 736, 57